DISCONTINUOUS PRECIPITATION IN CU-IN ALLOYS

THE KINETICS OF DISCONTINUOUS PRECIPITATION IN COPPER INDIUM ALLOYS

By

JACK MURRAY SHAPIRO, B.A.Sc., M.A.

A Thesis

Submitted to the Faculty of Graduate Studies

in Partial Fulfilment of the Requirements

for the Degree

Doctor of Philosophy

McMaster University

May 1966

DOCTOR OF PHILOSOPHY (1966)
(Metallurgy)

McMASTER UNIVERSITY
Hamilton, Ontario.

TITLE: The Kinetics of Discontinuous Precipitation in Copper Indium Alloys

AUTHOR: Jack Murray Shapiro, B.A.Sc. (University of Toronto)

M.A. (University of Toronto)

SUPERVISOR: Professor J. S. Kirkaldy

NUMBER OF PAGES: ix, 136

SCOPE AND CONTENTS:

This thesis is concerned with the cooperative growth problem of the discontinuous precipitation reaction. Previous theories are examined, and the kinetic details of a model, which assumes the existence of a metastable monotectoid reaction and the adherence to local equilibrium, are derived. As with other attempts to describe the parameters of duplex growth situations, we cannot find a unique relation between the rate of growth and the lamellar spacing. The various optimal or variational procedures used to remove this degree of freedom are considered. The Cu-In system is subject to quantitative experimental study, and the extent of interference of the concurrent general precipitation reaction is determined. Finally the kinetic data and auxiliary information are used to test the various theories.

ACKNOWLEDGMENTS

I should like to thank Professor J. S. Kirkaldy for suggesting the topic of research, and for his encouragement and help throughout the study. Thanks are also due to many of the faculty, technical staff, and graduate students. In particular, discussions with Professors R. K. Ham and G. R. Purdy proved most helpful. The assistance of Mr. H. Walker in various aspects of the electron microscopy was appreciated. I also wish to thank Mr. R. Foster for preparing the line drawings, Mrs. N. Shennan for typing the thesis, and my wife for her help with the manuscript.

Finally, I should also like to express my gratitude for the following financial support: McMaster Graduate Research Scholarship, Ontario Graduate Fellowship, and the Steel Company of Canada Fellowship in Metallurgy.

TABLE OF CONTENTS

LIST OF SYMBOLS

Specific alloy phases are designated by the symbols used by Hansen and Anderko (189). The list below does not include these.

Symbol	Definition	Page of First Appearance
A	integration constant in Cahn's analysis	36
A	minimum value of the free energy of formation of the α and β phases, Figure 14	46
A'	minimum value of free energy of formation of the α' phase, Figure 14	46
A_n	set of Fourrier coefficients for the austenite composition distribution (Hillert's model)	30
a	equilibrium α phase composition, Figure 14	46
a	crystal lattice cube edge	96
a'	composition of α' phase at minimum value of free energy of formation	46
a_n	decay constants for the austenite composition distribution in Hillert's model	30
b	effective diffusion zone thickness of the advancing incoherent interface	14
b_n	set of period coefficients for the austenite composition distribution in Hillert's model	30
D or D_v	volume diffusion coefficient	15

Symbol	Definition	Page of First Appearance
D_B	diffusion coefficient in the advancing interface	14
D_{vc}	volume diffusion coefficient calculated from equation 4	17
D_{vm}	volume diffusion coefficient taken from the literature	17
f	free energy of formation of the α', α or β phases in Figure 14	46
ΔF	molar free energy of precipitation that is dissipated at the advancing interface in Cahn's model	36
ΔF_o	molar free energy change for complete precipitation	14
g	a parameter of equation 1	13
G	fraction of grain boundary occupied by cellular precipitate	80
H	a constant in the generalized growth rate expressions	56
ΔH	activation energy found for vS^3 in Figure 59	
ΔH	activation energy for a	112
ΔH_c	activation energy for diffusion found from equation 2 or 4	17
ΔH_D	activation energy for boundary diffusion	112
ΔH_q	activation energy for q	112
ΔH_{vm}	activation energy for volume diffusion taken from the literature	17
J	diffusive flux	28
J_i	generalized thermodynamic flux	55

Symbol	Definition	Page of First Appearance
$K^{\alpha\gamma}$, $K^{c\gamma}$	factors which determine the effect of interface curvature on the composition of austenite in local equilibrium with ferrite or cementite, respectively	31
K	ratio of total available free energy of transformation to the amount stored in the $\alpha\beta$ interface	50
k	ratio of the advancing interface composition to the product phase composition	35
$L_{\alpha,\beta}$	coefficient related to boundary diffusivity	42
L_{iK}	phenomenological coefficients relating fluxes J_i to forces X_i	55
l	length of traverse of a random line used in lineal analysis	80
M	interface mobility	36
m	a parameter in equation 1	13
m	constant in the analytic expression of a phase boundary	116
N_1	number of grain boundaries intersected by a random line	80
N_2	number of cells intersected by a random line	80
P	pressure; superscript denotes the phase on which P acts	27
P	fraction of the available free energy of transformation that is dissipated or stored in the $\alpha\beta$ surfaces in Cahn's analysis	36
p	constant in the analytic expression of a phase boundary	116

Symbol	Definition	Page of First Appearance
Q	fraction of the minor component precipitated	37
q	parameter in the free energy of formation expressions	46
R	gas constant	31
R	fraction of the available free energy of transformation that is stored in the $\alpha\beta$ interfaces, as used in Cahn's analysis	37
R^{α}, R^{β}	integration constant for the α or β phase composition distribution	47
r	radius of curvature, usually of the interface between phases	27
S	lamellar spacing of cellular aggregate	14
S^{α}, S^{β}	thickness of α or β phase in lamella	14
S_c	minimum lamellar spacing allowed by available free energy of transformation	27
s	distance measured along the (curved) cell-matrix interface	42
T	temperature	15
T_{cr}	temperature below the solvus temperature at which the tendencies for discontinuous dissolution after prior precipitation at a lower temperature, and for further discontinuous precipitation, are equal	20
T_o	solvus temperature	15
T_o	maximum solvus temperature of a miscibility gap	112
T_p	temperature at which precipitation is allowed to proceed	20

Symbol	Definition	Page of First Appearance
T_s	temperature at which dissolution of cellular precipitate is allowed to proceed	19
t	time	13
V	molar volume; with subscripts, partial molar volume	27
v	growth speed of a nodule	13
X	volume fraction of transformed material	13
X_1	average composition of α precipitated at T_{cr}	20
X_2	average composition of α formed by dissolution at T_{cr}	20
X^{α}, X^{c}	carbon content of ferrite or cementite	28
X_{α}^{γ}, X_{c}^{γ}	carbon content of austenite in local equilibrium with ferrite or cementite across an interface of arbitrary curvature	27
$X_{\alpha}^{\gamma o}$, $X_{c}^{\gamma o}$	carbon content of austenite in local equilibrium with ferrite or cementite across a flat interface	27
X_e^{α}	equilibrium composition of α phase (α or e is omitted occasionally)	14
$X_e^{\alpha'}$	initial composition of α' phase (α' or e is omitted occasionally)	14
X_p	composition of α phase on completion of cellular precipitation	19
X_s	average phase composition after discontinuous dissolution of the cellular precipitate below the solvus temperature	20
X_i	the set of independent thermodynamic forces	55

Symbol	Definition	Page of First Appearance
y	distance measured normal to the plane of the $\alpha\beta$ interface	28
z	distance measured normal to the cell-matrix interface	28
α	major product phase of cellular precipitation	1
α	Zener's distance parameter; superscript refers to product phase	28
α	dimensionless parameter in Cahn's analysis	37
α'	supersaturated α phase; undergoes cellular precipitation	1
β	minor product phase of cellular precipitation	1
β	dimensionless parameter in Cahn's analysis	37
γ	activity coefficient	41
ϵ	constant in a free energy expression	117
λ	vS^2/bD_B	47
μ	micron	3
μ_α^i	chemical potential of the i component of the α phase	41
σ	surface tension; superscripts denote the separated phase	14
σ	rate of internal entropy production	55

LIST OF TABLES

INTRODUCTION

Discontinuous or cellular precipitation is said to occur when a supersaturated phase (α') decomposes to the structurally identical, but solute depleted α phase and a new β phase, by the growth of cells or nodules of the parallel $\alpha + \beta$ mixture (usually lamellar) into the α' phase. This reaction appears metallographically (fig. 1) identical to cooperative eutectoid decomposition, e.g. pearlite growth in steels. Segregation takes place at the advancing interface between the cell and the α' matrix, showing the origin of the discontinuous label, i.e. the composition of α' and α remain constant. The cooperative side-by-side growth of the α and β phases accounts for the two striking features of the isothermal reaction, i.e. the uniform spacing of the lamellae, and constant growth rate. Such regularity suggests that one may be able to predict the kinetic parameters through a thermodynamic and diffusion model. Therefore this thesis is concerned with the growth problem of discontinuous precipitation.

We shall examine previous theories of growth, and derive the kinetic details for a model which assumes the existence of a metastable monotectoid and adherence to local equilibrium at the interface. The extent to which these theories can be tested and distinguished experimentally will also be discussed.

The experimental work consists of a description of the precipitation behaviour of copper rich copper-indium alloys. The observations of precipitation by mechanisms other than the discontinuous mode are included so that the latter can be properly placed in relation to the general theoretical considerations. The precipitation behaviour is compared with that of other alloy systems to see which features are specific to each system, and how ideal each one is when measured against the theoretical standard.

CHAPTER 1

DISCUSSION OF PREVIOUS WORK

1.1 Introduction

Discontinuous precipitation has been reviewed in the literature several times in the past. Much of the discussion has had the aim of relating this reaction to the more familiar general precipitation (33, 36). Smith (31) has discussed the morphology and kinetics of the reaction with special reference to general microstructural principles. Sulonen (144) has reviewed the micrographic features, kinetics and possible conditions for the occurrence of discontinuous precipitation. In this chapter we shall document these features, expanding on previous works. It is apparent that there exists a variety of duplex cooperative transformations other than the familiar eutectoid pearlite and controlled eutectic solidification reactions. Of these, discontinuous precipitation is but the simplest example. It is also apparent that there is now available a sufficient amount of kinetic data to make some comparisons with theoretical predictions.

1.2 Simple Reaction - Morphology

The most obvious feature of cellular precipitation is its initiation at a structural imperfection, usually a grain boundary. Nodules have also been observed in Pb-Sn single crystals at dendrite boundaries (34), and discontinuous precipitation has been implied from x-ray work at high supersaturation in single crystals of Cu + 4 - 5% Ag (1); however the perfection of the crystal was not noted. Gruhl and Kramer (6) observed that no cells

formed on sub-grain boundaries in Cu-Ag alloys. Underwood (79) showed cells within grains of a Au-Ni alloy, but the absence of inclusions was not established. Finally DeSorbo and Turnbull (5) demonstrated that the majority of small (~30 μ) Pb-Sn spheres (highly perfect crystals) remain supersaturated while bulk material underwent the usual discontinuous precipitation.

Since the cells do begin growth at a grain boundary, it is reasonable to ask whether a cell is the cooperative growth of the common grain boundary precipitate. There is evidence that the regular lamellar form is not always attained at the grain boundary. Gruhl and Kramer (6) and Sulonen (144, p. 28) show that lamellae are dissociated from the grain boundary precipitate.

Nonetheless, the original grain boundary does have an important role. Smith (31) showed that this boundary becomes the interface between the growing nodule and the grain being consumed, i.e. the α phase has the orientation of the adjacent but untransformed α' grain. This fact has been demonstrated by polarized light microscopy on Zn - 2% Cu. Additional evidence is seen in figure 2, which shows a nodule containing the continuation of twins of the parent α' grain. This phenomenon has been observed in Cu - Ag (31), Zn-Cu (6), and Cu-Cd (144). The same conclusion is reached from experiments using transmission electron microscopy for Cu - 3 wt % Co (96), and the continuation of slip lines and alignment of x-ray spots for Cu-Cd (144). Further demonstration is provided by observations of the early stage of discontinuous precipitation in Cu-Cd, in which the grain boundary bows out as the precipitate forms (144).

C. S. Smith (31) states that the advancing interface is incoherent and thus provides a good diffusion path for the segregating species. (In fact the term "discontinuous" was chosen to denote this mode of precipitation

because x-ray work (1) showed the appearance and intensification of separate diffraction lines corresponding to the depleted α phase, rather than a continuous change in the diffraction angles of the α' parent phase which may indicate a volume diffusion process.) Therefore the only orientation relation between the cell and the grain being consumed is the avoidance of particular orientations. This is completely analogous to the result noted by G. V. Smith and Mehl for Fe-C pearlite growth (31). In this regard Gruhl and Kramer (6) have noted that a growing cell is occasionally stopped on encountering a twin in the grain being consumed.

The effect of a variation of the mutual orientation of the initial α' grains is of interest, but it has thus far been inadequately investigated. Gruhl and Amman (4) used polycrystalline Cu - 30% Ni - 30% Mn and Cu - 1.8% Be specimens with a [100] fibre axis. The width of the cellular precipitate band increased with increasing orientation difference, up to a flat maximum at 45°. The authors interpreted this result as reflecting a variation in nucleation rate with orientation, although Cahn (41) has shown a better correlation with the expected variation of boundary diffusion coefficient, and hence growth rate. Because observations were taken at only one time these two causes cannot be differentiated. In addition one has no information about the mobility of tilt boundaries or the direction of growth of the cells from the boundary, which may vary with orientation and thus systematically change the apparent cell size. Similar but less extensive observations have been made in the Cu-Be (2, 33) and Au-Pt (109) systems. Finally we must recall that cellular precipitation has been observed in single crystals (36, 1) and within grains (79), so that it may be possible for entirely new orientations to nucleate from relatively weak imperfections and provide the incoherent interface necessary for solute diffusion.

The orientation relation between the α and β phases within a cell is of some interest. Quite early C. S. Smith (136) suggested that a fixed habit does not exist because branching (frequently observed) enables growth in all directions with a fairly uniform spacing. Continual branching contradicts an hypothesis of a rigid habit. Direct observation in Cu - 3.1 wt % Co by Phillips has revealed both {100} and {111} habits, which must be approximate because of curving and branching (96). On the other hand C. S. Smith, in contradiction to his early premise, (31) shows that in Zn + 2% Cu the habit of the Widmanstatten pattern in the neighbouring grain is continued in a growing cell. A very rigid habit has been found in the first cellular precipitate from Fe - 30 Ni - 6 Ti by Speich (15) - (001) Ni_3Ti || $(111)_\gamma$; [010] Ni_3Ti || $[\bar{1}10]_\gamma$, which results in an almost perfectly coherent interface. No branching of lamellae was ever observed in this system. The nodules in the Cu-Cd system are composed of β rods in the α matrix (144). These rods lie in the α (111) plane and x-ray spots from some planes are found to be aligned. Thus we may conclude that a rigid habit obtains only in a few alloy systems.

1.3 Related Cooperative Duplex Reactions

The previous section has shown that many morphological features are common to all systems exhibiting discontinuous precipitation. We now show that a great variety of thermodynamic situations result in this general morphology. The sequence and morphology of the various reactions in the remainder can often be rationalized by the independent evaluation of the relative stability of the reaction products.

a. β' → martensite (α') → cellular precipitate (α + γ)

Cu - 11.8 wt % Al exists as the β phase above 565°C, undergoing

eutectoid reaction to $\alpha + \gamma$ below this temperature. If the β phase is quenched below 385°C, a martensite forms which is structurally related to the α (f.c.c.) phase. This martensite subsequently undergoes a discontinuous reaction to $\alpha + \gamma$ from 525°C to 325°C (136, 138). If we consider the martensite as supersaturated α, the correspondence with the usual cellular precipitation reaction is exact. Smith (136) has shown that the lamellar spacing in the latter case is greater than that in the pearlite formed directly from β at the same temperature. Assuming that the spacing is inversely proportional to the free energy change of the transformation, this observation is consistent with the fact that the martensite has a lower free energy than the β phase.

b. $\beta \rightarrow$ massive (ζ_s) $\rightarrow \zeta + \gamma$

At ~23.5 wt% Ga and 616°C the Cu-Ga phase diagram shows a eutectoid reaction $\beta \rightarrow \zeta + \gamma$. However on holding below 616°C, a metastable hcp ζ_s phase forms by the massive reaction (154, 156). ζ_s is an extension of the ζ phase as shown by extrapolating the lattice parameters of ζ to the ζ_s composition. Spencer and Mack observe that ζ_s subsequently transforms to $\zeta + \gamma$ by the cellular mode (154). (These authors have also observed the general precipitation of γ from ζ_s, which Massalski has claimed to be the only mechanism (156).) Thus (a), (b) are examples of the simple cellular precipitation reaction in which the initial phase is metastable at all temperatures

c. Pearlitic $[\alpha + \beta]_1 \rightarrow$ pearlitic $[\alpha + \beta]_2$

There are several examples where the lamellar products of a primary reaction undergo a second cellular precipitation. In all cases the lamellar spacing of the second reaction is greater than that of the first. The title above indicates that phases of the initial and final states have identical structures. This is indeed the case for the first five systems shown in Table I

In the sixth system, however, the first reaction may be considered as occurring in the extrapolated $\gamma + Ni_3 Ti$ phase field, while the second occurs in the stable $\gamma + (Fe, Ni)_2 Ti$ field. In addition the stable products can grow directly into the supersaturated γ above 900°C.

Table I - Alloy Systems Showing Consecutive Cellular Segregation Reactions

Alloy wt %	Temperature Range °C	First Reaction	Reference
Cu - 6 Be	< 600	Eutectoid $\beta \rightarrow \alpha + \beta'$	153
Cu - 31 In	< ?	Eutectoid $\beta \rightarrow \alpha + \delta$	151
Zn - 22 Aℓ	< 275	Eutectoid $\alpha_1 \rightarrow \alpha + \beta$	155
Cu - 23.5 Ga	< 616	$\zeta_s \rightarrow \zeta + \gamma$	154
Pb - Sn		$\alpha' \rightarrow \alpha + \beta$	28
Fe - 30 Ni - 6Ti	400-975	$\gamma_A \rightarrow \gamma_B + Ni_3 Ti$	15
Ag - 50 Cd	< 440	$\beta \rightarrow \alpha + \zeta$	152

Two further examples, which differ slightly from those above, deserve consideration. Co-Ta (10-15 wt. %) at 900°C (7) and Co-Ni-Nb (2-6 wt. % Nb) at 750-900°C (14) undergo a cellular precipitation reaction which is later replaced by a Widmanstatten morphology whose phases have the same structure as the previous cellular products.

For all of the systems discussed, where no change of structure accompanies the second reaction, the compositions of the primary and secondary phases are of great interest. Unfortunately, only in the case of Cu-6Be have measurements been made to indicate that the supersaturation of the α phase is greater for the first reaction. Nonetheless we must assume that the products of the first cellular segregation reaction are sufficiently unstable

in terms of structure, surface energy or composition to sustain a further precipitation reaction.

We make another important inference from the existence of this type of reaction. The advancing interface between the new nodule and the old must average or smear out the thermodynamic state of the duplex matrix over distances less than the spacing of the new lamellae.

1.4 Concurrent General Precipitation

Most of the alloys that exhibit discontinuous precipitation also decompose by a continuous mode. The sequence and conditions for occurrence of these mechanisms have been the subject of many discussions, as noted in the introduction. Since our main purpose in this thesis is to gain an understanding of the growth process of discontinuous precipitation, a discussion of the continuous mode is relevant only if it yields information on the thermodynamic state of the matrix awaiting cellular precipitation. For the sake of discussion we will divide the various precipitating systems into three groups:

a. The effective supersaturation of the matrix changes with time. In such a situation the discontinuous reaction is competing with the continuous reaction and the kinetics should be extremely difficult to predict.

b. The continuous precipitate is effectively frozen in a metastable state after some time so that the nodules advance into a duplex structure. This situation resembles 1.3 (c) above.

c. The general precipitate has the properties of the equilibrium phase but its formation involves only very local volume diffusion. The matrix may then be considered to have retained its original supersaturation except for small pockets of depletion. This situation should approximate

the ideal case of no general precipitate if the fraction of the total volume involved therein is small and the average distance between particles of the new phase is much larger than the lamellar spacing of the discontinuous precipitate. In particular the kinetic parameters should be the same as if no general precipitate forms.

Unfortunately, few of the studies in this field have been designed to provide the information needed for the above categorization. In fact a single system may fall into more than one category with varying composition and temperature. Nevertheless the discussion which follows is organized as suggested above.

a. Competition for solute between the general and cellular precipitate was suggested by C. S. Smith (31), but no direct evidence was given as proof. However it has often been noted that at low supersaturation (high temperature) continuous precipitation predominates, because of the relative kinetics of the two reactions as discussed by H. Böhm (38). The C-curve for the volume diffusion controlled general precipitation reaction sits at higher temperatures than the C-curve for the boundary diffusion controlled discontinuous precipitation. Hence, at high temperature the matrix can be continuously depleted by the general precipitate while the cells advance at an ever decreasing velocity. Therefore continuous precipitation predominates at high temperatures.

Böhm found the maximum temperature for the cellular precipitation mode to be from 0.8 to 0.9 of the absolute solvus temperature for a number of copper based alloys (39). Although he did not notice a systematic deviation from the steady state growth in this temperature region we shall include these alloys in the table below.

The Au-Ni system may also fall into this category. Because cells grow inward from the grain boundaries, it is possible to maintain the grain centers of large grained material supersaturated for longer times at the aging temperature. Gerlach found evidence of a continuous change in the matrix of such large grained specimens (64). The Curie temperature of a 50-50 alloy aged at 410°C rose from 95°C to 120°C during aging, compared to 340°C for the Ni - rich phase of the discontinuous precipitate. (The Curie temperature decreases with increasing Au content.) For the moderate aging times required in materials of average grain size this continuous change can probably be neglected.

Table II - Alloys in which Discontinuous and Continuous Precipitation Compete in Growth

	Alloy	Conditions and Remarks	Reference
1.	Ag-Cu	Low Supersaturation	1
2.	Au-Pt	Indefinite classification, but 2 processes are simultaneous	109
3.	Co-9Ti	Low Supersaturation, ~900°C	8
4.	Cu-1.8 Be	" "	6, 39
5.	Cu-3 Co	650-750°C (minimum range)	96
6.	Cu-In	Low Supersaturation	27, 38, 39
7.	Cu-Mg	" "	39
8.	Cu-20Ni-30Co	Similar to #2 above	32
9.	Cu-Sb	Low Supersaturation	39
10.	Zn-2 Cu	≥ 150°C; retardation noted	6

b. Cellular segregation occurring in the metastable mixture of general precipitate and matrix has definitely been observed in some alloys. For others

however the distinction between (b) and (c) may depend on the quality of the metallography. Often an author merely reports that nodules form during or after general precipitation. Usually the scale of the first reaction is much finer than that of the second. In the table below those alloys whose status is doubtful are marked by an asterisk.

Table III - Alloys in which Discontinuous Precipitate Develops from a Metastable General Precipitate

	Alloy	Conditions and Remarks	Reference
1.	Al-Ag	$\gamma' \rightarrow \gamma$ is cellular	33, 38
2.	Co + Ni+6 Nb	Widmanstatten structure well developed before cellular reaction	14
3.	Co + 10-15 Ta	<900°C; similar to Co-Ni-Nb above	7
4.	Cu + 3-5.3 Ag*	At lower supersaturation cellular follows general precipitation especially in single crystals. A transition phase of 10 At % Ag also reported.	1 3
5.	Cu + 2-4 Cd*	Metastable general precipitate forms only in strained specimens	144
6.	Nb+12.6 Cr	1260°C - similar to #2 above	43

c. Discontinuous precipitation has been observed to proceed unaffected by the general precipitate in the systems tabulated below. The criteria are constant growth rate and uniform spacing. In no case, however, have specific efforts been made to establish the absence of situations (a) and (b) above.

Table IV - Alloys in which the Discontinuous Precipitate is not Affected by the Continuous Precipitate

	Alloy	Conditions and Remarks	Reference
1.	Cr + 20-50 Ni	800 - 1000°C	12
2.	Cu + 1.8 Be	Higher Supersaturation	6
3.	Cu + 6-15 In	T < 0.8 T solvus, Böhm finds no general precipitate (27)	

Table IV (con't)

3. (con't)	but Corderoy and Honeycombe do (124).	27, 124, 39
4. Nb - 9 Cr	1205°C	43

Cu-Sb, Cu-Mg, Cu-Sn may also fall into this category at high supersaturation, although continuous precipitation is presumed absent by Böhm (39).

1.5 Breakdown of Cooperative Growth at High Temperatures

Hirschhorn and Gregg have observed the enlargement of the lamellar precipitate at the cell-matrix interface for Nb-Cr alloys at high temperatures, as shown in figure 3 (16, 43). On surveying the behaviour of 14 alloy systems they have concluded that this morphology occurs at temperatures above 0.6 of the absolute liquidus temperature. This behaviour is associated with the increasing importance of volume diffusion at these high temperatures and shows that the solute is diffusing to the interface from the matrix. The cell advances as the precipitate is redistributed in a lamellar form.

1.6 Dissolution of Discontinuous Precipitates

Sulonen has studied extensively the dissolution of cellular precipitate in the Cu-Cd (11) and Pb-Sn (145) systems. It is found that dissolution takes place by the retreat of the incoherent cell boundary, both above and below the solvus temperature. For dissolution above the solvus there is evidence of inhomogeneity remaining in the single phase alloy, while below the solvus, particles of the second phase remain behind the dissolution front (fig. 4). These are globular rather than lamellar. There appears to be competition between cellular dissolution and direct dissolution of the second phase into the matrix by volume diffusion at the highest temperatures, and some

spheroidization may precede either or both dissolution processes. The interpretation of kinetic data is complicated by the presence of an additional experimental variable - both the temperature of dissolution and prior precipitation must be considered. An acceptable theory of cellular growth must be consistent with the associated dissolution process.

1.7 Previous Quantitative Work: The Mechanism of Discontinuous Precipitation

Intensive study of the kinetics has been made for a number of alloy systems. We shall anticipate some of the theoretical derivations of the next chapter in presenting and discussing the results of these various measurements. The theoretical quantities of particular interest are the rate of advance of the cell-matrix interface and the $\alpha + \beta$ lamellar spacing within the nodules, both measured as functions of composition and temperature. We shall not discuss in detail the rate of cell formation at grain boundaries, for this quantity is not particularly relevant to the steady state growth problem. (However, it is important in the design of experiments and for making measurements.)

a. Growth Rate and Spacing

There are two classes of methodology used in the measurement of cell growth rates. One class involves the direct observation of the rate of increase of nodule size with time. The other is indirect, relying on the derivation or calculation of the growth rate from a measurement of the fraction of the sample that has transformed. Such methods include lineal analysis (19), used for Cu-Cd (144) and Co-Ni-Nb (14), resistance measurements for Pb-Sn (29) and Au-Ni (79) and magnetic measurements for Au-Ni (63, 64). The experimental results can be fitted to an equation of the form (40, 42).

$$X = 1 - \exp[-g\,(vt)^m] \qquad (1)$$

for a high nucleation rate, where X is the volume fraction transformed, g depends on the type of nucleation catalyst and the grain size,

v is the cell growth rate,

t is the time,

m takes the values 1 for nucleation on grain surfaces,

2 for nucleation on grain edges,

3 for nucleation on grain corners.

If, however, the nucleation rate is initially low and increases with time, then eq. (1) does not hold. Once the sites available for nucleation become exhausted the form of the rate equation changes so that the extraction of the quantity of interest, v, becomes difficult. For a fuller discussion of this problem the reader is referred to Cahn's analysis (40, 42). In this section we shall consider only the results of direct measurement of growth rates.

In section 2.3a we outline Turnbull's derivation (25) of an expression for the growth rate:

$$v = \frac{X_o^{\alpha'} - X_e^{\alpha}}{X_e^{\alpha}} \frac{bD_B}{S^2} \qquad (2)$$

This expression does not fix the spacing, and so Turnbull used the value predicted by Zener (26) for the pearlite growth problem:

$$S = \frac{4\sigma V}{\Delta F_o} \qquad (3)$$

where $X_o^{\alpha'}$ is the initial mole fraction of the minor component in the alloy,

X_e^{α} is the equilibrium composition at the reaction temperature,

b is the effective thickness of advancing interface,

D_B is the diffusion coefficient in the advancing interface,

S is the lamellar spacing,

σ is the α - β surface tension,

V is the molar volume of the alloy,

ΔF_o is the molar free energy change for complete precipitation.

Although Cahn (22) has criticized the derivation of these expressions, as discussed in the next chapter, they contain most of the same important functional dependencies as more sophisticated derivations, so we retain them for the general discussion. They say, in effect that

a. the spacing should decrease with increasing supersaturation.

b. that the growth speed depends most strongly on temperature through the exponential variation of D_B with temperature.

c. the growth speed also depends on the supersaturation, directly through $(X_o^{\alpha'} - X_e^{\alpha})$ and indirectly through the variation of S.

d. the behaviour of all systems should be roughly similar.

The corresponding expression for v assuming volume diffusion in the α' matrix is

$$v = \frac{X_o^{\alpha'} - X_e^{\alpha}}{X_o} \quad \frac{D_v}{S} \qquad (4)$$

Thus from the experimental values of S, v and their dependence on X_o and T, one can test the above expressions.

Let us first discuss the observed spacing. Fig. 5 shows a plot of 1/S as a function of T/T_s for constant initial composition of various systems. T is the absolute reaction temperature and T_s is the absolute solvus temperature for the particular alloy. T/T_s serves as a rough measure of the supersaturation for all systems.

In order to put all results on a comparable basis of equal α - β surface tension, the following adjustments are made:

(1) The value of $1/\delta$ for Cu-Cd (curves 2-1, 2-2) have been multiplied by 1.7 to account for the greater surface area associated with the rod morphology as opposed to the lamellar form of most systems.

(2) $1/\delta$ for 3-1 has been arbitrarily divided by 5. From Section 1.2 it will be recalled that the lamellae in this Fe-Ni-Ti alloy attained a high degree of coherency, so that a low surface tension should result. Speich (15) estimates that σ = 20 - 100 erg/cm^2, values which are a factor of 5 to 25 less than that of an incoherent grain boundary free energy. Since one may presume σ for other systems will have values less than the maximum a factor of 5 was chosen in figure 5.

The results fall within ~50% of the average, except for Cu-In alloys (27) for which $1/\delta$ is about 1/3 the average. Therefore we may conclude that the spacing shows a fairly consistent behaviour for all systems. To test equation 3 quantitatively Cahn (22) calculates σ using estimates of ΔF_o based on Henry's and Raoult's Laws (see section 2.3a). E.g., for Pb - 14.7 Sn at 90°C $\Delta F = 8.35 \times 10^8$ erg/gm mole which gives σ = 650 erg/cm^2. The maximum value one expects for σ is about 190 erg/cm^2 (162); therefore the value from the analysis of the experiments is at least 3.4 times too large. Speich found an error factor of 3 for Fe-Ni-Ti (15) and for comparison Zener found a factor of 5 for the Fe-C eutectoid (26).

Turnbull and Treaftis (29) found that the spacing observed at a particular temperature was independent of the thermal history of the specimen. Up or down quenching from temperature to temperature resulted in a unique spacing at each temperature. Thus we must conclude that the failure to agree with equation 3 is due to a fault in its derivation and not due to the difficulty of nucleating a nodule with a sufficiently fine spacing.

Sulonen also cold rolled Cu-Cd specimens 10% before aging (144). The spacings observed were the same as those for undeformed material although the growth rates were greatly increased. We may be led to the conclusion that the spacing depends more strongly on the conditions of supersaturation than any other parameter.

In the Cu - 6 Be eutectoid alloy which shows consecutive cellular reactions, an interesting phenomenon occurs which may contradict the conclusion given above (153). As the second cellular reaction proceeds the minimum observable spacing of the first reaction increases. This change in apparent spacing is detected quite early so that we must conclude that there exists a range of spacings, the finest of which are first consumed by the second reaction.

The experimental results for the growth rate cannot be presented as concisely as those for the spacing. Equations 2 and 4 based on cell boundary and volume diffusion, respectively, are useful for discussion of the results. One can use the measured values of v and S to calculate bD_B and D_{vc}, from which one may determine the activation energy for the diffusion process. Table 5 summarizes the findings of several authors.

Table V - Kinetic Data for Various Alloys

Alloy	Quantities Measured	$\frac{D_{vc}}{D_{vm}}$	ΔH_c Kcal/gm mole	ΔH_{vm} Kcal/gm mole	Data fits Eq. 2 or 4	Reference
Pb-Sn	S, v	6.10^4*	8-10	26	2	28, 22
Cu-Cd	S, v	10^2-10^5	43	10-46	2 or 4	144, 168
Cu-In	S, v	3.10^3*	22	35-58**	2	27
Fe-30 Ni-6Ti	S, v	4.10^3	40	67.5	4	15
Au-Ni	v		25-38	42	-	79
Co-Ni-6Nb	v		76*	65	-	14

Notes: D_{vc} = volume diffusion coefficient calculated from equation 4.

D_{vm} = independent volume diffusion data (168).

ΔH_c = activation energy calculated from equation 2 or 4

ΔH_{vm} = activation energy for volume diffusion from independent diffusion data. (168)

* = calculated by this reviewer.

** = data for Cu-Sn (Cu-In not available)

For Au-Ni Underwood calculated a diffusion activation energy directly from the variation of the growth rate with temperature, realizing that these values may be only approximate. Actually at high supersaturation both S and $X_o^{\alpha'} - X_e^{\alpha}$ vary slowly with temperature in comparison to bD_B so that ΔH_c calculated in this region may be quite good. Therefore we let ΔH_c for Au-Ni be 38 Kcal/gm mole. ΔH_c(Co-Ni-6Nb) was calculated in the same way. We believe the high value obtained (76 Kcal/gm mole) results from the presence of and the variation with temperature of the amount of previous Widmanstatten precipitate, (see Table 3).

From Table 5 it appears that Pb-Sn and Cu-In behave as suggested by equation 2. The results for all the alloys show that precipitation takes place too rapidly for it to be explained by a volume diffusion mechanism and therefore suggest the involvement of cell boundary diffusion. However, the activation energy for Cu-Cd is too high for boundary diffusion, which prompted Sulonen to suggest that perhaps the process may be controlled by the "recrystallization act" of the matrix. The data for Cu-Cd can fit either equation 2 or 4 equally well. Although the data for the Fe-Ni-Ti system qualitatively fits the volume diffusion equation, D_{vc}/D_{vm} is unreasonably large and an activation energy more appropriate to interface diffusion is found. These results will be discussed further in the next chapter.

(b) Extent of Solute Depletion

There is convincing evidence that the α and/or β phases of a cellular precipitate are supersaturated on formation. Early work on Au-Ni showed that the Curie temperature of the Ni-rich phase rises slowly after the initial discontinuous reaction which demonstrates that freshly formed phases do not have their equilibrium composition (195). Micrographs of Au-Ni alloys show a variation of etching behaviour from the centre to the periphery of a cell (79). Turnbull and Treaftis found by means of resistometry and x-rays that only 50-60% of the excess tin was drained from solid solution when the cells had completely impinged (28, 29). That is $X_o - X_f = 0.55\ (X_o - X_e)$ where X_o, X_f, X_e are the initial, final, and equilibrium compositions respectively at any particular temperature. No information was obtained on the tin-rich phase. The results for Cu-Cd differ slightly (144). Using an x-ray method which allows a resolution of 0.1 wt. % it was found that about 0.3 to 0.4 wt. % excess Cd remained in the α lamellae for all initial compositions and reaction temperatures. Sulonen concluded that this resulted from the small radius of curvature of the β rod ends at the advancing interface. On the other hand, Böhm concluded for Cu-In that the α phase was of equilibrium composition, and that the observed x-ray line breadth was due to elastic strain near the cell front, for the lines were observed to sharpen with time (44). It is recalled (see section 1.3c) that the first pearlitic reaction in eutectoid Cu-6 Be resulted in a supersaturated α phase.

(c) Discontinuous Dissolution. $\alpha + \beta \rightarrow \alpha' (+\beta)$

In Section 1.6 the qualitative features of discontinuous dissolution were discussed. We now turn to a quantitative discussion. As mentioned in 1.6 this reaction, when compared with precipitation, has an additional controllable variable. One can now choose the dissolution temperature T_s as well

as the initial composition X_o and the temperature of precipitation T_{pr}. The lamellar spacing, average α composition and amount of precipitate to be dissolved are fixed by the precipitation temperature. The maximum α' composition is set by the dissolution temperature above the solvus temperature, T_o in fig. 6a. The variables one would like to measure are the growth rate, v, of the dissolved regions and some quantity related to the composition gradients left behind the interface, fig. 6b. Of these quantities only the velocity of dissolution has been carefully studied - in Cu-Cd (11) and Pb-Sn (145) by Sulonen.

The behaviour of v is quite different above and below the solvus temperature T_o. For a given X_o, v increases rapidly with increasing dissolution temperature T_s, when $T_s < T_o$, and for a given $T_s < T_o$, v increases slowly with decreasing initial composition X_o. In both these cases the increase in v is due mainly to the smaller number of precipitate particles remaining behind the dissolution front (fig. 4). In Cu-Cd alloys of $X_o < 3$ wt. % Cu and $T_s < T_o$ the average α composition after dissolution has the value X_s given by the $\alpha/(\alpha+\beta)$phase boundary, but in the 4.2 wt. % Cd alloy this composition exceeds X_s by an amount which increases with the dissolution temperature T_s. This behaviour constitutes a kind of reversion.

Below the solvus one can also define a temperature T_{cr}, which is that temperature at which upon up-quenching from T_{pr} the tendency to dissolve is equal to the tendency to precipitate further with a different spacing S. It is found that $(X_o - X_1) = (X_2 - X_p)$ where

X_1 is the composition of α precipitated at T_{cr}

X_2 is the composition of α formed by dissolution at T_{cr}

X_p is the composition of α precipitated at T_p.

At T_{cr} the rate of interface advance (precipitation) is equal to the rate of retreat (dissolution), although the diffusion distance for the dissolution reaction depends on the lamellar spacing established by prior precipitation at T_p and is, of course, much smaller than the lamellar spacing for precipitation at T_{cr}. Sulonen concluded that at least one of the reactions cannot be diffusion controlled. The precipitate remaining after dissolution may account for the retardation of this process.

In Pb-Sn alloys, for which considerable supersaturation remains after cellular precipitation ($[X_p - X_e^\alpha] = 0.45\ [X_o - X_e^\alpha]$), the solvus temperature for the average α composition X_p is comparatively high. Dissolution takes place at and above this temperature, while the second stage of precipitation, also discontinuous, occurs below.

At temperatures above the solvus, dissolution behaviour is more regular. Sulonen showed that the growth rate could be fitted to a modified form of equation 2:

$$v \alpha \frac{bD_B}{S^2} \frac{X_s - X_p}{X_o - X_p} \qquad (5)$$

(see fig. 6)

The factor $\frac{X_s - X_p}{S}$ gives the diffusion gradient and $(X_o - X_p)\ S$ is proportional to the amount of precipitate dissolved. No quantitative allowance is made for the free energy gained from the destruction of the α - β interfaces. Activation energies for diffusion are calculated to be 17.5 - 13.5 Kcal/gm mole for Pb + 7-19 at. % Sn and 21 Kcal/gm mole for Cu-Cd, suggesting boundary diffusion control. Comparing equations 2 and 5 one finds an explanation why, at constant T_p and T_s, v increases with X_o more slowly for dissolution than for precipitation.

The dissolution behaviour after cold rolling 10% has been noted. Above

the solvus temperature little or no effect is observed in both Pb-Sn and Cu-Cd alloys. Sulonen interprets this as evidence for boundary diffusion, but it may also be that the effects of cold work are annealed out quickly at the higher temperatures.

1.8 The Cause of Cellular Precipitation

There has been much speculation about the cause of cellular precipitation. How can a non-eutectoid system decompose with a morphology suggestive of a eutectoid reaction? Early workers, whose main concern was the study of precipitation hardening, suggested that the cellular mode is the recrystallization act in a matrix strained by the general precipitate, even when such general precipitate was not detected by early experimental techniques (1, 33, 36). There is sufficient evidence to refute this suggestion. E.g. electron microscopy has failed to detect a general precipitate in Cu-Cd alloys (44).

Other investigators, acknowledging the existence of cellular precipitation as an independent, boundary diffusion controlled reaction, still seek a fundamental reason for its occurrence. This reaction is observed in some precipitating alloys and not in others. The work of Böhm (38) on Cu alloys and that of Hirschhorn and Gregg (16) have shown the obvious limitation of the discontinuous reaction to the temperature range where boundary diffusion predominates.

Hagel and Beattie have related a greater matrix - precipitate lattice mismatch to the occurrence of cellular precipitation in multicomponent Ni-Co-Ti based alloys (9). In addition one notes that the lattice mismatch between the end phases of Cu-Ni-Co is greater than that of Cu-Ni-Fe, and only the former shows the discontinuous reaction (81). From these observations one may argue that a greater mismatch inhibits the nucleation of general precipitate

or the rate of spinodal decomposition thus allowing the discontinuous reaction to proceed. However we are already familiar with the Fe-Ni-Ti system in which the Ni_3Ti precipitates by the cellular mode and is almost coherent with the matrix. Therefore the lack of matrix-precipitate coherency cannot be a criterion for the occurrence of discontinuous precipitation.

Böhm has suggested that the atom size difference between solute and solvent, in copper based alloys at least, is the controlling factor, noting that if this difference exceeds 11% cellular precipitation occurs. However this reaction occurs in Cu-Co (96), Cu-Ni-Co (32) and Cu-Ni-Mn (4), in which the atomic radii differ at most by 3%. Therefore it is probable that a large size effect accounts for nothing more than the limited solubility at low temperatures, the essential condition for any precipitation.

Sulonen proposes an interesting model for the driving force of discontinuous precipitation (17, 72). A zone, impoverished in solute, is supposed to form ahead of the advancing interface by fluctuations of the boundary position and volume diffusion. This zone, coherent with the remainder of the untransformed α', is subject to a tensile or compressive stress depending on the sign of the change of lattice parameter with composition. There are no stresses behind the interface in the newly formed cell, so that a net force for interface migration exists. That is, as the interface advances the matrix strain can be relieved. Under an external stress applied to the specimen, the transfer of atoms across the α' - cell interface results in the relaxation of stress so that a cell acts somewhat as a cavity. Stress concentrations exist at cavity surfaces, doubling the tensile stress at points tangential to the applied stress, while points on the surface whose tangent is normal to the applied stress experience a compressive stress almost equal to the average stress. These stresses add to the solute depletion stress in the matrix,

increasing or decreasing the rate of interface migration in the appropriate direction. On dissolution these effects should be reversed.

Experiments were performed on Cu-Ag, Cu-Cd, Cu-Mg, Ag-Cu, Pb-Sn, and Zn-Cu alloys which seem to confirm the predictions. The growth rate was increased in the direction parallel to the applied tensile stress in Ag-Cu, Pb-Sn and Zn-Cu. Cu-Ag and Cu-Mg showed a larger growth velocity perpendicular to the stress.

No measurements of other discontinuous precipitation parameters were made, such as the effect of stress on spacing and α composition. No comparisons of growth rate were made between systems of varying misfit. Since this model depends on the existence of a strong variation of lattice parameter with composition, then the occurrence of cellular precipitation in alloys whose components differ but little in atomic size suggests that the proposed model may not be correct.

Kirkaldy has suggested a possible condition for the occurrence of this reaction (21). The morphological similarity to eutectoid decomposition suggests that the reaction occurs in a metastable monotectoid, as indicated in fig. 7. Such a model does not exclude simultaneous general precipitation. This suggestion will be examined in detail in a later section.

We may conclude from the work done to date that the cause of discontinuous precipitation has not been established beyond reasonable doubt.

CHAPTER 2

THEORY OF COOPERATIVE GROWTH

2.1 Introduction

Phase transformations involving steady state cooperative growth have been subject to many theoretical studies. The object of these studies has been to predict the kinetic parameters and hence identify the dominant factors in the growth process. Historically, the austenite-pearlite reaction was first studied (26, 172, 173, 23) followed by work on cellular precipitation (25, 22) and controlled eutectic solidification (174, 175).

It is instructive to compare the basic characteristics of the three reactions. Each of the two new phases of the eutectic and eutectoid reactions differ from the parent, while the structure of one new phase is identical to the parent in cellular precipitation. The most common path for material transport appears to be the parent phase for eutectics and the Fe-C eutectoid (interstitial solute), but the advancing interface is the likely transport path for discontinuous precipitation and eutectoids of substitutional solid solutions. For practical purposes the experimentally controllable variable is the growth rate in the solidification process, while it is the temperature in the case of the solid state reactions. This follows from the greater latent heat production of the first reaction. Also the slowest growth speeds commonly used in eutectic solidification are of the order of the fastest rates for the solid state reactions.

In this chapter we review the various models proposed for the growth process. The work on the pearlite problem serves as an excellent introduction to the consideration of the cellular precipitation process, while

reference is made to eutectic studies for comparison only. Finally, the details of the model proposed by Kirkaldy (21) are derived.

2.2 The Pearlite Growth Problem

a. Thermodynamic Situation

Let us consider the region about the advancing pearlite-austenite interface, as indicated in fig. 12, section 2.4b. The assumption is made that the transport of carbon from α to Fe_3C occurs in the parent austenite, and that the carbon content of the product phases remains substantially constant. The required rejection of carbon by α and its acceptance by Fe_3C provide a constant buildup and deficiency, respectively, in γ ahead of the new phases. This constant lateral concentration gradient results in the steady diffusive flux of carbon and hence in a steady growth rate. This is not possible in the case of spherical or planar diffusional growth of a single phase from a supersaturated matrix.

The free energy of formation vs. composition curves at a temperature below the eutectoid temperature are shown in Fig. 8 a. The common tangents determine the compositions for metastable equilibrium between γ - α and γ - Fe_3C. These are just the extrapolations of the stable phase boundaries, fig. 8 b. Since $X^{\gamma}_{\alpha 0} > X^{\gamma}_{C0}$ then the assumption of local equilibrium at the centres of the γ - α and γ - Fe_3C interfaces is sufficient to provide the gradient required for nodule growth. Brandt uses this assumption as a boundary condition in his treatment of this problem (172, 173). He points out, however, that local equilibrium cannot obtain everywhere along a planar growth front for this would result in an infinite gradient at the three phase juncture.

Zener demonstrates the importance of considering the energy of the created α - Fe_3C interfaces (26), and the resulting curvature of the γ - α

and γ - Fe_3C interfaces. Associated with a curved interface is a pressure difference between the two phases equal to

$$\Delta P = \left(\frac{1}{r_1} + \frac{1}{r_2}\right) \sigma$$

where r_1, r_2 are the principal radii of curvature, and σ is the interfacial tension. Since the interfaces of concern here are cylindrical, $r_2 = \infty$ and

$$\Delta P = \frac{\sigma}{r} \qquad (6)$$

One usually assumes that the parent phase, γ, remains at the relatively low value of atmospheric pressure.

Assuming local equilibrium, the effect of this pressure difference can be considered in two equivalent ways. One can evaluate analytically the change in chemical potential of each component of the phases affected and derive the resulting composition relations at the interface; this is done later. Alternatively, one may consider that the increase in free energy of the phase under pressure is $V\Delta P$ where V is the molar volume of the α or Fe_3C phase. The free energy composition curves are shifted upwards (shown in fig. 8) resulting in new values of $X_\alpha^\gamma(P^\alpha)$, $X_C^\gamma(P^C)$, and a smaller difference $X_\alpha^\gamma - X_C^\gamma$. As an inference from the Gibbs-Thomson equation, Zener writes

$$X_\alpha^\gamma - X_C^\gamma = (X_\alpha^{\gamma o} - X_C^{\gamma o})(1 - S_C/S) \ , \qquad (7)$$

where

$$\frac{2\sigma^{\alpha\beta} V}{S_C} = \Delta F_o \ , \qquad (8)$$

and ΔF_o is the bulk free energy change for the eutectoid reaction at T_1. It is seen that when $S = S_C$, then $X_\alpha^\gamma = X_C^\gamma$. Thus when all of the free energy available from the transformation is stored in the α- Fe_3C surfaces, then the lateral carbon gradient in the austenite falls to zero. For this case,

growth cannot proceed.

Local equilibrium and the continuity of X^{γ} can be maintained at the advancing interface if the curvature of the α, β phases increases continuously from the centre of each phase to the three phase juncture. Along this line X_{α}^{γ} must be equal to X_{C}^{γ}. This is the situation which Hillert describes in his treatment of the pearlite problem (23).

Brandt and Zener note that the assumption of local equilibrium cannot be exactly valid in a kinetic situation. Some free energy difference must exist to provide the driving force for the reconstruction of γ into α and Fe_3C, but this is assumed to be a very small fraction of the total free energy available in the reaction, and is therefore ignored.

Cahn has coupled diffusion and interfacial reaction equations in his formulation of the growth problem for both discontinuous precipitation and eutectoid decomposition (22). This treatment is discussed later.

b. Evaluation of the Rate of Growth by Dimensional Arguments

Zener uses a dimensional argument to evaluate the growth rate of pearlite (26). Let X^{α}, X^{C}, X_{o}^{γ} be the carbon concentrations in ferrite, cementite and initial austenite respectively. The flux of carbon atoms away from (or towards) the appropriate new phase is

$$v(X_{o}^{\gamma} - X^{\alpha}) = J \qquad (9)$$

or

$$v(X_{o}^{\gamma} - X^{C}) = J \qquad (10)$$

This flux must be supported by a concentration gradient in the austenite given by the diffusion equation

$$J = -D \frac{\Delta x}{\Delta y} \qquad (11)$$

where y refers to the lateral distance, (fig. 12).

$$\Delta y = \alpha S \ , \qquad (12)$$

where α is a numerical factor which depends on the choice of eq. 9 or 10 above. Also,

$$\Delta X = X_{\alpha}^{\gamma} - X_{C}^{\gamma} \, . \tag{13}$$

Combining eqs. 9, 10, 11, 12, 13 one obtains

$$v = D \frac{X_{\alpha}^{\gamma} - X_{C}^{\gamma}}{X_{o}^{\gamma} - X^{C}} \frac{1}{\alpha^{C}} \frac{1}{S} \left(1 - \frac{S_{C}}{S}\right) \, . \tag{14}$$

Thus one can evaluate the growth rate in terms of the spacing. The effect of the spacing is twofold:

(1) it determines the approximate diffusion distance,

(2) it determines the magnitude of the concentration difference in the austenite for a particular temperature.

A most important fact learned from this analysis is that an absolute evaluation of v or S cannot be made from considerations of diffusion alone. There remains the problem of choosing a method by which such an evaluation can be made. Zener postulates that the reaction proceeds at the maximum possible rate. Setting $\frac{dv}{ds} = 0$ (max.) in equation 14 yields the result, $S = 2S_{C}$. This fact implies that $\frac{1}{2}$ of the available free energy of the transformation is stored in the α - Fe_3C interfaces. In section 1.7a we note that this statement is not true experimentally. This problem is discussed again later (section 2.5).

c. Accurate Analysis of the Growth Rate and Interface Shape

A proper evaluation of the growth rate can be made by solving the diffusion equation subject to the assumptions of a moving interface and other boundary conditions. This has been done by Brandt (172) and Hillert (23).

The two-dimensional diffusion equation referred to axes (oz', oy) fixed in the material is

$$\frac{\partial^2 X}{\partial z^2} + \frac{\partial^2 X}{\partial y^2} = \frac{1}{D}\frac{\partial X}{\partial t} \quad , \tag{15}$$

where X is the carbon concentration and D its (constant) diffusion coefficient in γ. The form of this differential equation is inconvenient for a description of steady state growth. Because a steady state exists, compositions measured at a fixed distance from the moving interface are time invariant. That is to say,

$X(y, z) = \text{constant}$,

where $z = z' - vt$,

which results in a new differential equation in which the time does not explicitly appear (172, 23), viz.,

$$\frac{\partial^2 X}{\partial z^2} + \frac{\partial^2 X}{\partial y^2} + \frac{v}{D}\frac{\partial X}{\partial z} = 0 \ . \tag{16}$$

This differential equation is of order two in z and y. Therefore four independent pieces of information are needed to effect a complete solution.

Choosing the origin at the centre of an α lamella introduces a simplifying symmetry, and the general solution to equation 16 becomes

$$X - X_o^{\gamma} = \sum_{n=0}^{\infty} A_n e^{a_n z} \cos b_n y \tag{17}$$

where X_o^{γ} is the original austenite composition,

$$a_n = -\frac{v}{2D}\left[1 \pm \left(1 + \frac{4b_n^2 D^2}{v^2}\right)^{1/2}\right] \tag{18}$$

and

$$b_n = \frac{2\pi n}{S} \quad , \tag{19}$$

In general, A_o is finite and so an average carbon buildup exists ahead of the interface for a distance of the order of D/v.

The use of cosine terms and $n \geq 0$ in eq. 17 follows from the choice of origin. The positive sign within the parentheses of eq. 18 must be chosen to yield the result $X^{\gamma} \to X_o^{\gamma}$ as $z \to \infty$. The lamellar spacing S results in the basic periodicity in X given by eq. 19. Thus two boundary conditions have been applied. There remains the problem of finding the set $\{A_n\}$.

From this point the treatment of Brandt differs from that of Hillert. Brandt assumes that two terms A_o, A_1 of eq. 17 are sufficient. To evaluate these, use is made of the mass balance relations at the interface. It is also assumed that $X_\alpha^{\gamma o}$, $X_C^{\gamma o}$ are the austenite compositions at the centers of the α and Fe_3C lamellae, as mentioned in section 2.2a, and that the center of one phase may lead the other. On the other hand, Hillert obtains equations for the complete set of A_n, first making the simplification that the interface is substantially flat, i.e. $e^{A_n z_o} \sim 1$, where $z_o = z_o(y)$ is the equation for the shape of the interface. The remainder of this subsection outlines Hillert's derivation.

The mass balance for a slab of thickness dy and extending to $z = \pm \infty$ is considered and it is assumed that the lever rule determines the relative thickness S^{α}, S^{C} of the two new phases to good accuracy. This yields an expression for A_n:

$$\frac{A_n b_n^2}{-a_n} = \frac{4v}{DSb_n} (X^C - X^{\alpha}) \sin \frac{n\pi S^{\alpha}}{S} \qquad n > 0 \qquad (20)$$

Local equilibrium across the advancing interface is assumed which results in an expression for the austenite composition in equilibrium with α or Fe_3C, showing the deviation with pressure or curvature:

$$X_\alpha^{\gamma o} - X_\alpha^{\gamma} = \frac{\sigma^{\alpha\gamma}}{RT\, K^{\alpha\gamma} r} \qquad (21\ a)$$

$$X_C^{\gamma o} - X_C^{\gamma} = \frac{\sigma^{C\gamma}}{RT\, K^{C\gamma}{}_r} \qquad (21\ b)$$

(The K's are only approximately independent of composition). Approximating $a_n = b_n$, these last expressions are related to the equilibrium three phase juncture angles to yield two equations in A_o. Eliminating A_o results in a relation for v:

$$\frac{v}{D} = \pi^3 \frac{S^{\alpha} S^{C}}{S^2 \sum_1^{\infty} \frac{\sin^2 \pi n S^{\alpha}/S}{n^3}} \frac{X^{\gamma}_{\alpha o} - X^{\gamma}_{Co}}{X^{C} - X^{\alpha}} \cdot \frac{1}{S}\left(1 - \frac{S_C}{S}\right) \qquad (22)$$

where

$$S_C = \frac{V\sigma^{\alpha C}}{RT(X^{\gamma}_{\alpha o} - X^{\gamma}_{Co})}\left(\frac{S}{S^{\alpha} K^{\alpha\gamma}} - \frac{S}{S^{C} K^{\gamma C}}\right)\left[1 + \frac{\sigma^{\alpha\gamma 2} - \sigma^{C\gamma 2}}{\sigma^{\alpha C 2}} \cdot \frac{S^{C} K^{\gamma C} + S^{\alpha} K^{\gamma\alpha}}{S^{C} K^{\gamma C} - S^{\alpha} K^{\gamma C}}\right] \qquad (23)$$

Hillert notes that

$$S^{C} K^{\gamma C} \underset{\sim}{} - S^{\alpha} K^{\gamma\alpha}$$

and

$$\sigma^{\alpha\gamma} \underset{\sim}{} \sigma^{C\gamma}$$

so that eq. (23) may be simplified and rearranged, and is seen to resemble equation 8. Equations 14 and 22 are also similar. In fact a reasonable choice of α^C in eq. 14 makes the two equations quantitatively similar. There still remains the problem of choosing v or S.

This detailed analysis also allows Hillert to calculate the shape of the advancing interface. One uses the composition determined at the interface $X^{\gamma}(z_o, y)$ in equations 21 a, b. The results confirm the approximation made in the growth calculation that the interface is fairly flat. These shapes are shown in figure 55.

Jackson et al have solved the same problem approximately by use of an electric analogue (176). This approximation results in the simpler

diffusion equation

$$\frac{\partial^2 X}{\partial z^2} + \frac{\partial^2 X}{\partial y^2} = 0 \text{ .} \qquad (24)$$

This is Laplace's equation, which also governs the distribution of electric potential on a plane conductor. Thus an analogy exists between carbon flux and current density, or carbon content and local voltage as measured by a probe. The configuration used is shown in fig. 9. The geometrically simple boundary conditions result from the choice of a symmetric eutectic reaction, so that $S^{\alpha} = S^{\beta}$. Assuming initially an arbitrary interface shape (flat), the composition distribution is measured. From this the shape may be calculated with sufficient accuracy that further iterations of the surface shape are unnecessary.

2.3 Growth Models for Discontinuous Precipitation

a. Evaluation of the Growth Rate by Dimensional Analysis

Turnbull (25) has transformed Zener's pearlite growth relation, equation 14, into a form suitable for the description of a boundary diffusion controlled process. Let $X^{\alpha'}$, X^{α} be the initial and final mole fractions of the minor component in the parent α' and new phase respectively, and let b be the effective thickness of the incoherent advancing interface. Then

$$v = \frac{X^{\alpha'} - X^{\alpha}}{X^{\alpha'}} \frac{b}{\tau} \text{ ,} \qquad (25)$$

where τ is the time necessary to drain the boundary region of solute. Now

$$\tau \approx \frac{S^2}{D_B} \text{ ,} \qquad (26)$$

so

$$v = \frac{X^{\alpha'} - X^{\alpha}}{X^{\alpha'}} \frac{bD_B}{S^2} \text{ .} \qquad (27)$$

The spacing S is chosen as that given by Zener for the pearlite problem, viz., $S = 2S_c$. This is the spacing for which v is a maximum in equation 14; however no optimization can be made from eq. 27 since the capillarity terms are not specificially taken into account. Turnbull then writes

$$S = \frac{4\sigma V}{RT \ln \frac{X^{\alpha'}}{X^{\alpha}}}, \tag{28}$$

but Cahn points out that $RT \ln \frac{X^{\alpha'}}{X^{\alpha}}$ is an incorrect expression for ΔF_o (22). Figure 10 illustrates a possible free energy-composition diagram for discontinuous precipitation. If the μ's are the chemical potentials we may write

$$\Delta F_o = \mu_A^{\alpha} + X^{\alpha'}(\mu_B^{\alpha} - \mu_A^{\alpha}) - \mu_A^{\alpha'} - X^{\alpha'}(\mu_B^{\alpha'} - \mu_A^{\alpha'}) \tag{29}$$

$$= X^{\alpha'}(\mu_B^{\alpha} - \mu_B^{\alpha'}) + (1 - X^{\alpha'})(\mu_A^{\alpha} - \mu_A^{\alpha'}) \tag{30}$$

Further, assuming Henry's Law for B and Raoult's Law for A, we have

$$\mu_B^{\alpha} - \mu_B^{\alpha'} = RT \ln \frac{X^{\alpha}}{X^{\alpha'}}, \tag{31}$$

and

$$\mu_A^{\alpha} - \mu_A^{\alpha'} = RT \ln \frac{1 - X^{\alpha}}{1 - X^{\alpha'}} \tag{32}$$

so that

$$\Delta F_o = RT \left[X^{\alpha'} \ln \frac{X^{\alpha}}{X^{\alpha'}} + (1 - X^{\alpha'}) \ln \frac{1 - X^{\alpha}}{1 - X^{\alpha'}}\right] \tag{33}$$

From equation 28 it is indeed seen that Turnbull has incorrectly used $-\Delta\mu_B$ instead of $-\Delta F_o$ in this expression.

The main merit of Turnbull's equation 27 is that it is semi-quantitative and easy to apply.

b. Growth Relations for Boundary Diffusion and Reaction Control

Cahn considers the growth problem of cellular precipitation and eutectoid decomposition assuming both interface diffusion and reaction control (22). It can be seen from fig. 10 that with the assumed constitution local equilibrium cannot obtain between α' and α. Therefore relations which determine the composition at the interface on the assumption of local equilibrium cannot be stated and Cahn enunciates some plausible alternatives.

The restriction of all solute transport to the cell boundary has the important consequence that segregation to the equilibrium composition cannot be achieved for any finite growth rate. For a given spacing the faster the interface advances, the less time there is allowed for solute diffusion. (We may note that in general a non-equilibrium solute distribution also derives from a volume diffusion controlled model of the eutectoid reaction with the assumption of local equilibrium, but the extreme sharpness of the α and Fe_3C free energy curves limits this inhomogeneity to insignificant levels in the pearlite reaction.) The existence of incomplete solute segregation with some corresponding stored free energy is quite compatible with the observation of successive cellular reaction discussed in section 1.3c.

The dependence of the lamellar solute content on growth rate is expressed indirectly through the postulated relation

$$X^{\alpha} = kX^{B} , \qquad (34)$$

where X^{B} is the interface composition and k is a constant. Given the spacing S, a greater v requires a steeper concentration gradient and therefore a

larger average concentration in the boundary. Eq. 34 shows that X^{α} is then larger as well.

The interdependence of v and the amount of solute segregation means another degree of freedom has now been introduced into the problem. To remove this degree of freedom a new kinetic condition must be imposed. In this model it is assumed that the growth rate v is proportional to the net free energy decrease. That is, the boundary mobility becomes important, in contrast to the assumption made by Brandt and Zener (section 2.2a). In analytic form, we have

$$v = -M\Delta F \tag{35}$$

with

$$\Delta F = P\Delta F_o + \frac{2\sigma V}{S} , \tag{36}$$

where M is the boundary mobility, and P is the fraction of ΔF_o available for dissipation or conversion to α-β surface energy. P is less than unity due to the imcomplete solute segregation.

The diffusion equation appropriate to the steady state motion of the flat α' - α interface is

$$bD_B \frac{d^2X^B}{dy^2} + v(X^{\alpha'} - X^{\alpha}) = 0 . \tag{37}$$

In writing just one equation for the boundary in front of the α phase, it has been assumed that the amount of the β phase is very small so that the simultaneous process in front of the β phase can be ignored. Using eq. 34, $X^{\alpha} = kX^B$, and placing the origin at the center of the α' -α interface results in the general solution to eq. 37

$$X^{\alpha} = X^{\alpha'} + A \cosh \left(\frac{kvS^2}{bD_B}\right)^{1/2} \frac{y}{S} . \tag{38}$$

The constant A is determined by assuming that X^{α} has its equilibrium com-

position at the α-β phase boundary, $y = \frac{S}{2}$. From this solution the following quantities can be calculated:

(1) the fraction of β precipitated,

$$Q = \frac{2}{X^{\alpha'} - X_e^{\alpha}} \int_0^{1/2} (X^{\alpha'} - X^{\alpha}) \, d\frac{y}{S}$$

$$= \frac{2}{\sqrt{\alpha}} \tanh \frac{\sqrt{\alpha}}{2} \qquad (39)$$

where

$$\alpha = \frac{KvS^2}{bD_B}$$

(2) the fraction of the total possible free energy change that is released on precipitation, P. One must assume some shape for the α-phase free energy curve of fig. 10 for this calculation.

(3) the fraction of ΔF_o expended on α-β surface energy, R.

Noting that

$$P = P(\alpha) \, , \qquad (40)$$

we substitute eq. 36 into eq. 35 to obtain

$$v = -M(P(\alpha)\Delta F_o + \frac{2\sigma V}{S}) \, . \qquad (41)$$

Thus eq. 40 and 41 are two equations in the three unknowns v, S, P, and so again, as in the pearlite problem, no unique determination of the kinetic parameters can be made, and some additional criterion must be used. Cahn assumes that the spacing which the system chooses is that which maximizes $|\Delta F|$ with respect to spacing. Because of eq. 35 v also attains its maximum value at this spacing. (When local equilibrium instead of reaction control is assumed as in the Zener-Hillert model, the maximum of $|\Delta F|$ corresponds to infinite spacing, or to zero growth rate, for then no energy can be stored in the α-β interfaces.)

Under the assumption of a maximum of $|\Delta F|$, the quantities P, Q, R, P-R and log α have been calculated and plotted in Fig. 11. The abscissa is the parameter

$$\beta = - \frac{kM\sigma^2 v^2}{bD_B \Delta F_o} \quad , \tag{42}$$

all the factors of which can in principle be determined independently. In this expression the ratio $\frac{M}{bD_B}$ is most important. From fig. 11 it is seen that at the extreme of high mobility and low diffusivity much supersaturation remains and most of the available chemical free energy is changed to surface energy. That is, the cell interface requires little net driving force for its advance. The limit of this situation is pure boundary diffusion control, as suggested by Turnbull. At the other extreme much segregation is achieved and relatively little energy is stored in the fewer α-β surfaces. That is, a low mobility allows more time for diffusion over the distance of a larger spacing. The spacing measurements of the last chapter seem to indicate such a situation. For both Pb-Sn and Cu-Cd, $\beta \approx 10^{-2}$ although the solute depletion of the Cu-Cd system alone is great enough to be consistent with the high Q shown in fig. 11.

Cahn explains the low β in this way. He assumes that the individual atomic mobilities in an incoherent boundary are anisotropic. Atoms should move more easily along an interface than into or out of one of the adjoining lattices. The boundary diffusivity is expected to reflect the larger values of atomic mobility while the boundary mobility reflects the lower values. The result is a low β. Perhaps those activation energies for diffusion shown in Table 5, which seemed high for boundary diffusion, actually reflect the influence of the interface mobility on the growth process.

Sulonen has considered the effect of the boundary mobility in his

model of the driving force for the growth process (72). It is recalled from section 1.8 that in this theory the interface advances to relax the coherency stress of the assumed solute depleted zone just ahead of the interface, and that an external stress can enhance or retard growth parallel or normal to the direction of the applied stress. Alloys whose precipitation behaviour indicates a low β (low mobility and high diffusivity) should be more sensitive to an external stress than a high β alloy whose precipitation growth rate is controlled mainly by the boundary diffusion. It was found that the enhancement of the growth rate due to an applied stress was greater for Cu-Cd alloys than Pb-Sn alloys. Since the supersaturation remaining after precipitation is much less in Cu-Cd, then it is indicated that this alloy might indeed be characterized by a lower β than Pb-Sn.

In summary, we have seen that Turnbull's approximate equation fits the growth data for a few systems fairly well. However the Zener spacing criterion leads to values about 1/4 of those reported. Cahn's theory of reaction and diffusion control can account for these larger spacings although some disagreement exists in the associated degree of segregation, and the theory assumes an arbitrary and unchecked boundary mobility value. Therefore we conclude that further study of the theoretical problem may be fruitful.

2.4 Metastable Monotectoid - Local Equilibrium Growth Model for Discontinuous Precipitation

a. Thermodynamics

In section 1.8 it was suggested that the discontinuous precipitation reaction may occur in a metastable monotectoid system (21, p.78). Not only is the growth morphology consistent with this model, but local equilibrium

can be assumed as well. This model also predicts the occurrence of the residual supersaturation and can be modified to allow the repetition of a cellular reaction. It will, of course, be very difficult to independently confirm the postulated metastable phase boundaries as indicated in fig. 7, in order to predict the observed supersaturations. In this respect the model has a similar weakness as Cahn's, in which the parameters k and M_s which determine the lamellar composition, are difficult to obtain independently. The results of the present derivation should also apply directly to eutectoid reactions involving substitutional solid solutions which segregate by phase boundary diffusion.

Following the suggestion of an underlying metastable monotectoid reaction, the details of a steady-state growth model based on local equilibrium and interface diffusion will now be derived.

Local equilibrium allows us to overcome some of the difficulties inherent in a boundary diffusion problem. Since the chemical potentials of a component in the parent phase, the boundary and the growing phase are all equal we need not discuss explicitly the composition in the interface. The chemical potentials can be written in terms of composition and pressure as

$$\mu_i^{\alpha'}(X^{\alpha'},o) = \mu_i^{B}(X^{B}) = \mu_i^{\alpha}(X^{\alpha},P^{\alpha}) \qquad (43\ a,b)$$

where i refers to the species,

B to the boundary phase, and

$$P^{\alpha} = \frac{\sigma^{\alpha'-\alpha}}{r^{\alpha}}$$

The a and b are used here and elsewhere in numbering the equations to show that we are discussing both the $\alpha' - \alpha$ and $\alpha' - \beta$ interfaces.

An important implication of equation 43 is the variation of $X^{\alpha'}$, which must be continuous along the whole interface. This requires volume diffusion ahead of the interface for at least a few atomic diameters. In the following it is therefore assumed that such diffusion can take place in the time allowed before the passage of the interface, but that this volume diffusion cannot contribute to the lateral solute transport. That this may be the case is seen from a consideration of the 0th term in eq. 17, $A_o \exp(\frac{v}{D_v} z)$. D_v/v is a characteristic forward diffusion distance which may be estimated for a typical system as from 5 to 20 A. Since characteristic spacings are much greater than this, no account of lateral volume diffusion need be taken.

Continuing the argument from eq. 43, we have

$$\mu_i^{\alpha'}(0,0) + RT \ln \gamma_i^{\alpha'} X_i^{\alpha'} = \mu_i^{\alpha}(0,0) + RT \ln \gamma_i^{\alpha} X_i^{\alpha} + P^{\alpha} \bar{V}_i^{\alpha} \qquad (44\ a, b)$$

Since the α' and α phases have the same crystal structure, i.e.

$$\mu_i^{\alpha'}(0,0) = \mu_i^{\alpha}(0,0) \quad ,$$

$$RT \ln \frac{\gamma_i^{\alpha'} X_i^{\alpha'}}{\gamma_i^{\alpha} X_i^{\alpha}} = \bar{V}_i^{\alpha} P^{\alpha} \quad . \qquad (45\ a, b)$$

Using $\sum X_i = 1$ for each phase allows one to calculate the lamellar composition at local equilibrium for a given curvature, viz.,

$$X_i^{\alpha} = X_i^{\alpha}(T, P^{\alpha}) \qquad (46\ a, b)$$

b. The Diffusion Equation

We consider a small box of unit depth which moves with the cell boundary as shown in fig. 12. Here s is the distance measured along the

boundary. In the steady state location d is sufficiently far from the interface that $X^{\alpha'} = X^{\alpha' o}$, the bulk composition. The boundary flux of component two averaged over the effective thickness b is taken to be

$$J_s = -L_\alpha \frac{\partial(\mu_2 - \mu_1)}{\partial s} \quad , \qquad (47\ a, b)$$

where L is a phenomenological coefficient related to the boundary diffusivity.

For a mass balance within the box

$$b_\alpha(J_S^+ - J_S^-) + \Delta S \cos\theta\ (J_z^+ - J_z^-) = 0 \quad , \qquad (48\ a, b)$$

where

$$J_z^+ = - v \frac{X^{\alpha' o}}{V^{\alpha'}}$$

and

$$J_z^- = - v \frac{X^\alpha}{V^\alpha} \quad \text{or} \quad - v \frac{X^\beta}{V^\beta} \ .$$

The above expressions result from the forward motion of the interface. Therefore,

$$b_\alpha \Delta S \frac{\partial J_S}{\partial s} - \Delta S \cos\theta \quad v\left(\frac{X^{\alpha' o}}{V^{\alpha'}} - \frac{X^\alpha}{V^\alpha}\right) = 0$$

and hence

$$b_\alpha L_\alpha \frac{\partial^2(\mu_2 - \mu_1)}{\partial s^2} + v \cos\theta \left(\frac{X^{\alpha' o}}{V^{\alpha'}} - \frac{X^\alpha}{V^\alpha}\right) = 0 \ , \qquad (49\ a, b)$$

where L_α is an appropriate average for the interface. It is seen that eq. 49 a is similar to Cahn's eq. 37.

The differential equation for the shape of the interface is

$$\frac{d^2 z_o}{ds^2} \Big/ \frac{dy_o}{ds} = - \frac{P^\alpha}{\sigma^{\alpha'\alpha}} \qquad (50\ a, b)$$

where $z = z_o(s)$, $y = y_o(s)$ are the parametric shape equations. They are related by the expression $y_o'^2 + z_o'^2 = 1$. Eqs. 49 and 50 are a simultaneous

pair, but approximating by the assumption $\cos\theta \doteq 1$ decouples them, so that the diffusion equation 49, may be solved alone.

c. Boundary Conditions

Two pairs of differential equations of order two require a total of eight boundary conditions. In addition the positions of the boundaries S^{α}, S^{β}, are themselves unknown making ten conditions required.

Setting the origin at the center of the $\alpha' - \alpha$ interface results in the following:

$$z_o(v) = 0 \tag{51.1}$$

$$z_o'(o) = 0 \tag{51.2}$$

$$\frac{d(\mu_2 - \mu_1)}{ds} = 0 \text{ at } s = 0 \tag{51.3}$$

At the $\alpha' - \alpha - \beta$ juncture ($y = \frac{S^{\alpha}}{2}$) we may write the interface continuity relation,

$$z_o^{\alpha}\left(\frac{S^{\alpha}}{2}\right) = z_o^{\beta}\left(\frac{S^{\alpha}}{2}\right) , \tag{51.4}$$

the flux continuity relation,

$$b_{\alpha}L_{\alpha}\frac{\partial(\mu_2 - \mu_1)^{-}}{\partial s} = b_{\beta}L_{\beta}\frac{\partial(\mu_2 - \mu_1)^{+}}{\partial s} , \tag{51.5}$$

(the $-$, $+$ signs indicate the discontinuity of $\frac{\partial \mu}{\partial s}$ at $y = \frac{S^{\alpha}}{2}$) and the local equilibrium relations,

$$\mu_i^{\alpha'} = \mu_i^{\alpha} = \mu_i^{\beta} . \tag{52}$$

Equations 52 represent four equations in five unknowns: $X_2^{\alpha'}$, X_2^{α}, X_2^{β}, P^{α}, P^{β}, and so may be reduced to a single relation between any two of them, say

$$X^{\alpha} = X^{\alpha}(X^{\beta}) \tag{51.6}$$

The interfacial tension balance determines the interface slopes at $\frac{S^\alpha}{2}$, viz,

$$\frac{\sigma^{\alpha'\alpha}}{\sin \phi^\beta} = \frac{\sigma^{\alpha\beta}}{\sin \phi^{\alpha'}} = \frac{\sigma^{\beta\alpha'}}{\sin \phi^\alpha} \tag{53}$$

where

$$\phi^\alpha + \phi^\beta + \phi^{\alpha'} = 2\pi \,. \tag{54}$$

In order to use these relations in the solutions of eq. 49 a, b without solving eq. 50 a, b we note using fig. 13 that,

$$\int_o^{\frac{S^\alpha}{2}} \frac{1}{r^\alpha}\, dy = \int_o^{\frac{S^\alpha}{2}} \left(\frac{d^2 z_o}{ds^2} \Big/ \frac{dy_o}{ds}\right) \frac{dy_o}{ds} \cdot ds = \int_o^{\frac{S^\alpha}{2}} \frac{d^2 z}{ds^2}\, ds$$

$$= \left.\frac{dz}{ds}\right|_o^{\frac{S^\alpha}{2}} = -\sin \theta^\alpha = \cos \phi^\alpha,$$

and therefore that

$$-\int_o^{\frac{S^\alpha}{2}} \frac{P^\alpha}{\sigma^{\alpha'\alpha}}\, dy = \cos \phi^\alpha \tag{51.7}$$

and

$$-\int_{\frac{S^\alpha}{2}}^{\frac{S}{2}} \frac{P^\beta}{\sigma^{\alpha'\beta}}\, dy = \cos\phi^\beta, \tag{51.8}$$

into which one must substitute the expression for P^α, P^β found from eq. 46 a, b. At the center of the $\alpha' - \beta$ interface, $y = \frac{S}{2}$, the following relations apply:

$$\frac{d(\mu_2 - \mu_1)}{ds} = 0 \tag{51.9}$$

and

$$\frac{dz}{ds} = 0 \tag{51.10}$$

Thus we have the ten conditions that enable us to find $v = v(S)$, the lamellar composition distribution and the interface shape.

There remains the problem of finding or estimating the appropriate thermodynamic data to enable detailed calculations following the above outline.

d. Approximate Analytic Solution for the Diffusion Problem

Figure 7 shows the free energy curves for a metastable monotectoid reaction. The analytic expression of these curves, including the correct dependence on temperature necessary to generate the phase diagram shown, is difficult to formulate. In general the local α and α' minima must shift to lower X values with decreasing temperature, and the curvature about these minima must increase.

Therefore our complete calculation will be concerned with an analytically simpler case, the symmetric eutectoid of figure 14. While such a specialization of the model has obvious deficiencies when applied to the discontinuous precipitation reaction it would appear to be quite realistic as applied to many eutectoid reactions involving substitutional solid solutions. Most serious of these shortcomings for discontinuous precipitation is the inability to describe with accuracy the effect of increasing supersaturation starting from the stable α phase (rather than α'). In particular, figure 7b predicts that there should be no cellular reaction in the region between the stable α-$(\alpha + \beta)$ and metastable $\alpha' - (\alpha' + \beta)$ phase boundaries.

For symmetry we assume that the following simplifications hold:

$$b_\alpha L_\alpha = b_\beta L_\beta$$
$$\sigma^{\alpha'\alpha} = \sigma^{\alpha'\beta} \neq \sigma^{\alpha\beta}$$

and

$$V^{\alpha} = V^{\beta} = V^{\alpha'} = V \quad . \tag{55}$$

The position and shape of the free energy curves of figure 14 are given by:

$$f^{\alpha}(X^{\alpha}, 0) = A + q(X^{\alpha} - a)^2 \tag{56 a}$$

$$f^{\beta}(X^{\beta}, 0) = A + q\,(X^{\beta} - 1+a)^2 \tag{56 b}$$

$$f^{\alpha'}(X^{\alpha'}, 0) = A' + q\,(X^{\alpha'} - a')^2 \tag{56 c}$$

and

$$f^{\alpha}(X^{\alpha}, P) = f^{\alpha}(X^{\alpha}, 0) + VP^{\alpha} \quad , \tag{57}$$

where the A's, a's and q are empirical constants. Up to this point we still allow a unsymmetric phase diagram by not restricting the value of a'.

The boundary diffusion equations 49 may be transformed into differential equations that contain the lamellar composition explicitly, rather than the chemical potentials, by using the local equilibrium relations

$$\mu_i^{\alpha} = \mu_i^{\alpha'} \quad .$$

These expressions are equivalent to the relations

$$\mu_2 - \mu_1 = \frac{\partial f^{\alpha}}{\partial X^{\alpha}} = \frac{\partial f^{\alpha'}}{\partial X^{\alpha'}} = \frac{f^{\alpha'} - f^{\alpha}}{X^{\alpha'} - X^{\alpha}} \quad . \tag{58}$$

Therefore,

$$\mu_2 - \mu_1 = 2q(X^{\alpha} - a) = 2q(X^{\alpha'} - a'), \tag{59 a, b}$$

and

$$\mu_2 - \mu_1 = \frac{A' + q(X^{\alpha'} - a')^2 - A - q(X^{\alpha} - a)^2 - VP^{\alpha}}{X^{\alpha'} - X^{\alpha}}$$

$$= \frac{A' - A}{a' - a} - \frac{VP^{\alpha}}{a' - a} \quad . \tag{60 a, b}$$

Substituting eq. 59 a, b into 49 a, b with the approximation $\cos \theta = 1$, we obtain

$$2qbLV \frac{\partial^2 (X^\alpha - a)}{\partial s^2} + v (X^{\alpha' o} - X^\alpha) = 0 \ . \qquad (61\ a, b)$$

2 q VL may be identified as the boundary diffusion coefficient, viz.,

$$2\ q\ VL = D_B \ . \qquad (62)$$

Eq. 61 operates directly on X^α, since the thermodynamic treatment has allowed us to bypass the surface phase composition, X^B, which was a necessary parameter in Cahn's diffusion eq. 37.

The solution of eq. 61 which is symmetrical about the origin, satisfying eqs. 51.3 and 51.9, is

$$X^\alpha - X^{\alpha' o} = R^\alpha \cosh \lambda \frac{s}{S} \quad (0 \leq s \leq \frac{S^\alpha}{2}) \qquad (63\ a)$$

$$X^\beta - X^{\alpha' o} = R^\beta \cosh \lambda \frac{s - \frac{S}{2}}{S} \quad (\frac{S^\alpha}{2} \leq s \leq \frac{S}{2}) \qquad (63\ b)$$

where λ is defined by

$$\lambda^2 = \frac{vS^2}{bD_B} \ . \qquad (64)$$

In the case of the symmetric eutectoid, the number of boundary conditions to be applied is reduced from those specified in the foregoing treatment. That is to say, we may use the symmetry conditions that $a' = \frac{1}{2}$, and $S^\alpha = S^\beta = \frac{S}{2}$. For generality, the value X=1 may occur in an intermediate phase rather than at the pure component. The application of eq. 51.5 yields

$$R^\alpha \lambda \sinh \frac{\lambda}{4} = -\lambda R^\beta \sinh \frac{\lambda}{4}$$

so that

$$R^\alpha = - R^\beta \ . \qquad (65)$$

Local equilibrium at the $\alpha - \alpha' - \beta$ juncture may be expressed through eq. 51.6 as

$$\frac{\partial f^{\alpha}}{\partial X^{\alpha}} = \frac{\partial f^{\beta}}{\partial X^{\beta}} .$$

Therefore, at $s = \frac{S}{4}$

$$X^{\alpha} - a = X^{\beta} - 1 + a ,$$

and hence

$$R^{\alpha} \cosh \frac{\lambda}{4} - a = R^{\beta} \cosh \frac{\lambda}{4} - 1 + a . \qquad (66)$$

Combining eqs. 65 and 66 we obtain

$$R^{\alpha} = - \frac{\frac{1}{2} - a}{\cosh \frac{\lambda}{4}} . \qquad (67)$$

To establish a relation between v and S eqs. 59 and 60 are used with eq. 51-7,

$$\int_0^{S/4} \left(\frac{2q(x^{\alpha} - a)(\frac{1}{2} - a)}{V} - \frac{A' - A}{V} \right) ds = \cos\phi^{\alpha} \, \sigma^{\alpha'\alpha} \qquad (68)$$

From eqs. 53 and 54 for the angle ϕ^{α}, we deduce

$$\cos\phi^{\alpha} = \frac{\sigma^{\alpha'\alpha^2} + \sigma^{\alpha\beta^2} - \sigma^{\beta\alpha'^2}}{2\sigma^{\alpha'\alpha}\sigma^{\alpha\beta}}$$

so that

$$\cos \phi^{\alpha} = - \frac{\sigma^{\alpha\beta}}{2\sigma^{\alpha\alpha'}} . \qquad (69)$$

Therefore,

$$2q(\tfrac{1}{2} - a) \int_0^{S/4} (\tfrac{1}{2} - a + R^{\alpha} \cosh \tfrac{\lambda s}{S}) ds - \frac{A' - A}{4} S = - \frac{\sigma^{\alpha\beta} V}{2}$$

and

$$2q(\tfrac{1}{2} - a)^2 (\frac{S}{4} - \frac{S}{\lambda} \frac{\sinh \frac{\lambda}{4}}{\cosh \frac{\lambda}{4}}) - (A' - A) \frac{S}{4} = - \frac{\sigma^{\alpha\beta} V}{2} \qquad (70)$$

Eq. 70 may be simplified further if the values of λ are small enough that $\tanh \frac{\lambda}{4}$ may be replaced by the first few terms of its power series expansion:

$$\tanh \frac{\lambda}{4} = \frac{\lambda}{4} - \frac{1}{3}\left(\frac{\lambda}{4}\right)^3 + \frac{2}{15}\left(\frac{\lambda}{4}\right)^5 \quad \ldots\ldots \qquad (71)$$

To verify this we note from Turnbull's eq. 27 that

$$\lambda^2 = \frac{vS^2}{bD_b} = \frac{X_o - X_e}{X_o} < 1$$

Therefore

$$\frac{\lambda}{4} < 0.25 \ ,$$

$$\frac{1}{3}\left(\frac{\lambda}{4}\right)^3 < 0.005 \ ,$$

and

$$\frac{2}{15}\left(\frac{\lambda}{4}\right)^5 < 0.000125 \ .$$

Thus the powers series for $\tanh \frac{1}{4}$ converges rapidly. Applying the first two terms of eq. 71 to 70, we obtain

$$\frac{S}{4}\left[1 - \frac{4}{\lambda}\left(\frac{\lambda}{4} - \frac{\lambda^3}{3.4^3}\right) - \frac{A' - A}{2q\left(\frac{1}{2} - a\right)^2}\right] = \frac{\sigma^{\alpha\beta}V}{4q\left(\frac{1}{2} - a\right)^2} \ .$$

Therefore

$$\frac{\lambda^2}{48} - \frac{A' - A}{2q\left(\frac{1}{2} - a\right)^2} + \frac{2\sigma^{\alpha\beta}V}{S\ 2q\left(\frac{1}{2} - a\right)^2} = 0 \ ,$$

and since

$$\lambda^2 = \frac{vS^2}{bD_B} \ ,$$

then

$$v = \frac{48bD_B}{S^2} \cdot \frac{A' - A}{2q\left(\frac{1}{2} - a\right)^2}\left(1 - \frac{2\sigma^{\alpha\beta}V}{(A' - A)S}\right) \ . \qquad (72)$$

The form of eq. 72 is shown in fig. 15.

Thus a relationship is derived which is quite similar to Hillert's volume diffusion eqs. 22 and 23 if we delete the quantity b/S (the ratio of boundary width to spacing), and note that

$$\frac{A' - A}{2q(\frac{1}{2}-a)} = \frac{1}{2}\,(X^{\alpha'}_{\alpha o} - X^{\alpha'}_{\beta o})\ ,$$

as seen from eqs. 59 and 60 for zero curvature (P = 0). Zener and Hillert assumed

$$S = 2\,\frac{2\sigma^{\alpha\beta}V}{A' - A} = 2\,S_C$$

as the result of the maximum growth rate postulate. We shall leave the optimal problem of determining the unique spacing to the following section and assume for present purposes that the optimum is designated by

$$S = K\,\frac{2\sigma^{\alpha\beta}V}{A' - A}\ , \tag{73}$$

where K is the order of but greater than unity.

Therefore

$$v = \frac{48bD_B}{S^3}\,\frac{2\sigma^{\alpha\beta}V}{2q(\frac{1}{2}-a)^2}\,(K - 1) \tag{74}$$

or

$$\frac{bD_B}{q(\frac{1}{2}-a)^2} = v\,S^3 \tag{75}$$

Eq. 72 or 74 is similar to Turnbull's eq. 27 only if

$$\frac{X^{\alpha' o} - X^{\alpha}_{e}}{X^{\alpha' o}} = \frac{24(A'-A)}{q(\frac{1}{2}-a)^2}\,(1 - \frac{1}{K})\ .$$

Although these coefficients will be of the same magnitude, a detailed connection cannot be established.

The variation of the quantity q with temperature will prove to be of interest later. The elementary theory of the free energy of solid solutions, as given by Cottrell (178), in which the enthalpy of mixing is merely the sum of nearest neighbour bond energies allows us to estimate this quantity, viz.,

$$q \triangleq \frac{1}{2} RT \left(e^{\frac{zU}{RT}} - 2zU\right) .$$

(In Cottrell's notation, z is the coordination number and $U = U_{AB} - \frac{U_{AA}+U_{BB}}{2}$ is the interaction energy.) It can be seen that q increases rapidly with decreasing temperature due to the exponential factor.

Finally at constant temperature eq. 75 predicts that vS^3 remains constant when the initial composition is varied, provided D_B is independent of composition. This prediction is capable of experimental test.

2.5 The Problem of the Choice of Spacing: Variational Principles

Equation 72 shows that for any spacing $S > S_c$, the steady state diffusion equations can be solved to yield a particular growth speed. However, it was shown experimentally in section 1.7a, for a given composition and precipitation temperature, that a almost unique spacing exists. We say "almost" since we recall that the Fe-Ni-Ti alloy showed a range of spacings that probably resulted from the inability of the quasi-coherent structure to branch, and that the Cu-Be eutectoid exhibited a variation of spacing accompanied by a variation in the composition of the new phases. We do not know whether this range of spacings resulted from a variation in $\sigma^{\alpha\beta}$, keeping $S = K S_c$, or from a variation of K. Nonetheless we must not be tempted to infer from figure 15 that although nodules of all spacings are growing, the fastest soon swamp the rest to yield the experimentally observed v and S. It is recalled from section 1.7a that the up and down quenching experiments of Turnbull and Treaftis (29) disproved this possibility.

The problem of selecting the stable kinetic parameters from the continuum of possible values, all of which satisfy the diffusion equations, is not limited to discontinuous precipitation, eutectoid, or eutectic reactions.

Kirkaldy has noted that a similar degree of freedom exists in the morphological development of a variety of two-phase reactions (21, p.96). Applying the principle of local equilibrium to an $\alpha \rightarrow \beta$ unidirectional growth system one finds that the development of a non-planar interface is accompanied by a cooperative variation between at least two intensive variables along the growth direction. In these cases a planar interface is still consistent with the diffusion equations. These reactions are tabulated below.

TABLE VI - Reactions in which a Non-planar Interface Develops.

Reaction	Intensive variables exhibiting Cooperative Variation
1. Dendritic pure element solidification from supercooled melt.	$\nabla T, \Delta\mu^{*}$; ∇P (provided by surface tension).
2. Cellular or dendritic binary alloy solidification from (constitutionally) supercooled melt.	∇T, $\nabla\mu$; ∇P
3. Plate or needle precipitation of β phase from α matrix.	$\nabla\mu$, ∇P, $\Delta\mu$
4. Ternary diffusion couple wherein the mean lateral composition passes through a two phase region of the phase diagram at an angle to the tie-lines.	$\nabla\mu_1, \nabla\mu_2$, ∇P

*$\Delta\mu$ represents a chemical potential step at the interface. If this quantity is small then local equilibrium is essentially obtained.

The departure from local equilibrium does not remove this degree of freedom, as Cahn's analysis has shown in section 2.3b. Nor will more

sophisticated treatments such as the introduction of a volume diffusion contribution to the solute transfer in discontinuous precipitation or a boundary diffusion contribution in the eutectoid reaction.

The approach to a solution of this problem is actually less advanced for the $\alpha \rightarrow \beta$ reaction than for the (α' or γ) $\rightarrow \alpha + \beta$ reactions which are of interest here. Among the first class of reactions the isothermal ternary diffusion reaction and most isothermal precipitation processes cannot easily be constrained to a specified steady state. This situation complicates the mathematical analysis. Indeed the most advanced treatments of the steady and unsteady problems merely specify the values of the various gradients in Table 6 that are necessary for the development of a non-planar interface but they do not specify the interface shape (yielding the equivalent of the spacing S) nor the composition distribution in the transition products. For example, in the binary alloy solidification problem, Mullins and Sekerka have derived the conditions for instability of a planar interface with respect to infinitesmal sinusoidal fluctuations (179) but have not described the stable transition product. For a given speed of solidification and temperature gradient in the liquid such instability only occurs for wavelengths between certain limits. The lower limit is set by consideration of the surface tension, while the upper limit is determined by the time available for lateral solute diffusion. This result is similar to that indicated in fig. 15, in which a trial lamellar spacing is analogous to a trial wavelength and the nodule growth rate is analogous to a positive rate of perturbation growth. In both problems the small wavelengths limit or small spacing limit exists due to capillarity. However in the solidification problem there is also a long wavelength limit because the growth of a fluctuation of the interface shape is superposed on the average rate

of advance of the solid-liquid interface. The solidification rate sets a limit on the time available for the lateral solute diffusion necessary for fluctuation growth. Hence a limit is set on the distance or wavelength of a fluctuation. Because only minute fluctuations are considered, no conclusion can be made concerning the transition to the ultimate steady state configuration. Shewmon has modified the analysis above by introducing the effect of reaction control at the interface (167). No fundamental advance is made in the quest for a unique interface configuration except that the onset of instability is more restricted.

We now return to a review of the attempts made to remove this degree of freedom.

The analysis of Mullins and Sekerka yields the rate of growth of a perturbation of a particular wavelength. The authors realize that the fastest growing wavelength cannot be chosen as the fundamental of the finite steady state because their calculations are strictly valid only for infinitesmal variations of the interface shape. Perhaps the required method of calculation is to assume a spectrum of possible morphologies with a finite departure from flatness and then to test each shape against further small changes.

In the example above it has been suggested that the steady state morphology can be found by testing a particular configuration for stability against fluctuation. Another method of approach is to construct some function which defines the stable state at an extremum with respect to one of the kinetic variables (eg. spacing). Glansdorff and Prigogine have shown that for certain hydrodynamic and thermodynamic systems, the two approaches to the stability problem are equivalent (197).

Kirkaldy has discussed the problem of the selection of an optimization principle (21, 180). As a first step we note that the achievement of a stable steady state by finding an extremum of some quantity characteristic of the continuum of possible kinetic states is analogous to the second law of thermodynamics in determining the stable state of a static system. We next note that the thermodynamics of irreversible processes has been applied successfully to a number of steady state processes which are simpler than the problem at hand. These are discrete systems such as the thermoelectric cell or continuous systems such as a single phase ternary diffusion couple. It is found, for example, that for a discrete system if the rate of internal entropy production, written as a thermodynamic potential,

$$\sigma = \sum_{i=1}^{n} J_i X_i = \sum_{i,k} L_{ik} X_i X_k$$

is minimized with respect to a variation of some of the independent thermodynamic forces, X_i, the others being kept constant, then the Le Chatelier stability criterion is generated in the form of an Euler-Lagrange equation like

$$J_1 \delta X_1 + J_2 \delta X_2 + \cdots = 0 . \qquad (76)$$

For a two-force system in which X_2 is fixed, say, this also generated the steady state condition in the form

$$J_1 = 0 .$$

This theorem, of course, makes the rather restrictive assumption that the symmetric matrix L_{ik} is constant.

Onsager has rephrased the stability problem in terms of microscopic fluctuations and, depending on the boundary conditions, obtains both a

principle of minimum entropy production and maximum entropy production.

Kirkaldy has postulated that the theories of Onsager and Prigogine (references given in (21) and (180)) can be extended to yield statements concerning heterogeneous dissipative processes. These deliberations have not as yet led to a quantitative or unequivocal result. Nonetheless, if such potentials exist, it is clear that they must be closely related to the dissipation function and will lead to a maximization or minimization, depending on the boundary conditions.

In the following we test the principle that the stable state for an isothermal cellular reaction is given by a maximum in the rate of entropy production. For the volume and boundary diffusion controlled eutectoid reactions, we let

$$\frac{dS}{dt} = - v \Delta F \tag{77}$$

where

$$\Delta F \triangleq \Delta F' + \frac{2\sigma V}{S} \quad . \tag{78}$$

Eq. 78 is approximate since $\Delta F'$ is a function of spacing through the influence of local equilibrium on the α and β compositions. For boundary diffusion control,

$$v = \frac{H}{S^2}\left(1 - \frac{S_c}{S}\right) \tag{79}$$

$$S_c = - \frac{2\sigma V}{\Delta F'} \quad .$$

$$- v \Delta F = - \frac{H}{S^2}\left(1 - \frac{S_c}{S}\right)\left(\Delta F' + \frac{2\sigma V}{S}\right)$$

$$= - H\, 2\sigma\, V \frac{1}{S^2}\left(1 - \frac{S_c}{S}\right)\left(- \frac{1}{S_c} + \frac{1}{S}\right)$$

$$= 2\sigma VH \frac{1}{S^4 S_c} (S - S_c)^2 \quad .$$

$$- \frac{d\ v\ \Delta F}{dS} = \frac{2\sigma VH}{S_c} \left[- \frac{4(S-S_c)^2}{S^5} + \frac{2(S-S_c)}{S^4} \right]$$

$$= \frac{2\sigma VH}{S_c} \left[\frac{2\ S(S-S_c) - 4(S-S_c)^2}{S^5} \right] .$$

$$\frac{dv\Delta F}{dS} = 0 \quad \text{when} \quad S = S_c \quad \text{or} \quad S - 2(S - S_c) = 0.$$

Therefore

$$S = 2\ S_c \ , \tag{80}$$

is the required result.

For volume diffusion control

$$v = \frac{H}{S} \left(1 - \frac{S_c}{S}\right) . \tag{81}$$

Therefore

$$v\Delta F = \frac{2\sigma VH}{S_c} \frac{(S - S_c)^2}{S^3} .$$

$$\frac{dv\Delta F}{dS} = 0 \quad \text{when}$$

$$- \frac{3}{S^4} (S - S_c)^2 + \frac{2}{S^3} (S - S_c) = 0$$

or

$$S = 3\ S_c . \tag{82}$$

Zener (26) proposed that the correct spacing is that which maximizes the growth rate. The values so obtained are $2\ S_c$ and $\frac{3}{2}\ S_c$ for volume and boundary diffusion control, respectively. We see that these values do not differ greatly from those which yield a maximum in the internal entropy production.

In the case of controlled eutectic solidification the indeterminancy appears in the form of a relation between S and the interfacial undercooling ΔT (174). An "ad hoc" principle to the effect that the undercooling is to be minimized has led to fair agreement with experiment. For low undercooling, this is equivalent to an optimization of the rate of entropy production.

The above result can be compared with that obtained by Cahn (22). He proposed that the steady state velocity is that for which the free energy decrease is greatest, (section 2.3b), which for his model is the state of maximum entropy production. Because of this basic assumption of interfacial reaction control the fraction of available free energy stored in the α - β interfaces, R, (equivalent to 1/K in eq. 73 for the local equilibrium model) varies with the boundary mobility. Figure 11 shows that R takes values from 0.05 to 0.5. The fraction of the free energy that is actually released by precipitation and stored in the boundaries is R/P, however, which varies from about 0.05 to 0.99 at $\beta \triangleq 100$. That is, relatively little free energy is dissipated to move the interface as the parameters of the system approach the local equilibrium case.

Another approach to the problem of stability of the advancing interface in the solidification problem is that of Bell (181). Here the Le Chatelier principle of moderation for a kinetic system (e.g. eq. 76) is applied to the fluxes and forces acting across the interface. That is, he assumes that the interfacial reaction is most important in determining interface morphology even if the dissipation in the diffusion field is greater. Bell did not extend the theory to a consideration of the spacing problem with which we are concerned.

Jackson and Chalmers have proposed another method whereby the lamellar spacing of a eutectic may be uniquely calculated (182). It is recalled from section 2.2a that the growth speed is a controllable variable in the solidification process and hence the undetermined quantity that varies with the spacing is the undercooling at the interface, ΔT. Assuming local equilibrium, ΔT may be calculated as that due to the solute buildup in the liquid which provides the concentration gradient for diffusion, ΔT_1, plus that due to the curvature of the α - L and β - L interfaces, ΔT_2. Tiller states that the stable configuration is obtained when ΔT is a minimum with respect to spacing, an intuitive assumption (174). Jackson and Chalmers note that if a termination, as shown in fig. 16, exists at the advancing interface then the stable spacing will be that for which the terminated lamella neither advances to the right with the growth process (decreasing the spacing) nor retreats to the left (increasing the spacing). Because of geometry each of the calculated undercoolings ΔT_1, and ΔT_2 near the termination differ numerically (not functionally) from the values calculated far from the termination. The authors state that at the stable spacing the total undercooling, $\Delta T_1 + \Delta T_2$, at the termination equals that remote from it, so that equating these two functions of the spacing yields a unique spacing. It is our opinion that equating the two total undercoolings is an arbitrary step, which assumes that the region of the termination neither projects from nor recedes into the average interface position, which ultimately must be regarded as having the same characteristics as an "ad hoc" principle. If the two undercoolings are not equal, which is a theoretical possibility, then a unique specification of the spacing has not been achieved.

In summary we may say that the problem of the internal degree of freedom associated with many irreversible processes is an intriguing one. The solution seems to lie in the perturbation methods of Mullins and Sekerka, or in the choice of an equivalent variational principle. For the $\alpha' \rightarrow \alpha + \beta$ type reaction such a variational principle has not as yet been definitely established.

CHAPTER 3

EXPERIMENTAL OBJECTIVES

3.1 General Experimental Objectives

The discussion of the theory of discontinuous precipitation and the review of previous work on this reaction suggest the direction of the experimental program. One should obtain as much knowledge of the relevant properties and the kinetic parameters of a particular alloy system as possible in order to evaluate the theory. The quantities required are listed below.

a. Properties of the Alloy

1. The thermodynamic properties of the unstable α' phase.

Such knowledge would verify the existence of an underlying metastable monotectoid reaction. This is a most difficult task. To measure the chemical potential of a component in solid solution requires the equilibration of that component with another phase, e.g. vapour or electrolyte. This must be accomplished in less time than that required for discontinuous precipitation at the interface between the alloy and the extra phase. The probability of success is greatest at high temperatures (low supersaturation), where the nucleation and growth processes are slow, but the diffusivity high.

2. bD_B, the boundary diffusion coefficient.

This data can be obtained independently only for grain boundaries in stable material. However, the theory actually requires data for the phase boundaries ($\alpha' - \alpha$ and $\alpha' - \beta$) in the unstable region of the phase diagram.

3. M, the mobility of the advancing interface.

The problem here is similar to that of determining bD_B. One may have

to be satisfied with simple grain boundary mobility data obtained in the stable region of the phase diagram.

4. $\sigma^{\alpha\beta}$, the interfacial tension of the $\alpha - \beta$ interface.

This quantity might be obtained from the three phase juncture angle at the advancing interface provided the surfaces are in mechanical equilibrium for the kinetic situation. The relative orientation of the two phases with respect to the interface, as determined by Speich for an Fe-Ni-Ti alloy (15), should corroborate the above information.

b. Parameters of the Growth Process

5. v, the speed of cell growth.

6. S, the lamellar spacing.

7. $X^{\alpha}(y)$, $X^{\beta}(y)$, the composition distribution within the lamellae.

It is necessary that this quantity be measured near the advancing interface, i.e. in material that has recently transformed and not had time for the relaxation of any concentration gradients. The spacings within which one seeks the concentration variations are of the order of 1μ, so that current electron-probe microanalysis techniques lack sufficient resolution. At very low supersaturations S increases, but the maximum possible concentration differences decrease, so that there is a further limitation here.

The resolution of an electron-probe microanalyser can be improved greatly as shown by a short review of some operating principles. Two main factors determine the size of the volume element from which characteristic x-rays are emitted. The first is the diameter of the electron beam at the specimen surface, which depends on the aperture size limiting the beam and the electron focussing geometry. The second is the accelerating voltage of the electron gun. The more energetic the electrons, the greater is the distance over which they can "diffuse" in the specimen and excite x-rays.

Decreasing the accelerating voltage greatly reduces the intensity of emitted x-rays, so that the practical limitation of effective spot size is about 1μ. However some of the incident electrons are scattered out of the specimen and may be counted. The fraction of the beam that is backscattered is roughly proportional to the average atomic weight of the specimen material and is independent of the accelerating potential. Therefore the voltage can be reduced, and the spot size diminished to a probe about 0.1μ, and still yield a measurable current of backscattered electrons (188). Of course this method is useful only for binary or pseudobinary alloys whose components differ greatly in atomic number so that the backscattered fraction varies considerably with composition in the alloy. For example Zn-Cu and Cr-Ni alloys cannot be studied by this technique. As we shall discuss later this experiment had to be abandoned.

8. $z^{\alpha}(y)$, $z^{\beta}(y)$, the shape of the advancing interface.

The assumptions of local equilibrium and the continuous decrease of chemical potential from the center of an α lamella to the center of a β lamella require that the curvature increase from the centre of a lamella to the edge. However, this condition is not sufficient to infer the existence of local equilibrium.

3.2 Choice of Alloy System

We should like to choose the alloy which will yield the maximum amount of information. Choosing an alloy for which some kinetic data is available (Table 5) allows us to seek the more difficult growth parameters b.7 and b.8.

We discuss the suitability of each of the alloys listed in Table 5.

a. Pb - Sn

The main drawback of Pb-Sn is the continuation of the precipitation and homogenization reactions at and below room temperature. Therefore the

determination of the lamellar composition and especially the interface shape would be extremely difficult.

b. Cu-Cd

Sulonen reports that the average α composition in the cell exceeds the equilibrium composition by about 0.3 wt. % Cd for all initial compositions and precipitation temperatures (144). Assuming a current resolution of about 1 part in 1000 for backscattered electrons means that the composition resolution is about 0.18 wt. % for Cu-Cd (or Cu-Ag and Cu-In) alloys. Therefore the determination of the composition profile would be difficult.

Cu-Cd decomposes by a different discontinuous mechanism at low supersaturations, which Sulonen believes to be metastable melting as suggested by the retrograde α - solidus (143). Therefore no measurements of any kind can be made in this region of the phase diagram. Finally the rod morphology of the cellular precipitate requires a more complicated theoretical analysis of the growth process (since the amount of α - β surface depends not only on the rod spacing but also on the relative amount of β precipitated).

c. Fe-Ni-Ti

Because of the low α - β surface tension the spacing S is very small and quite variable. The components do not differ greatly in atomic weight. A transmission electron micrograph of an $\alpha' - (\alpha + \beta)$ interface (15) shows a ragged shape, suggesting reaction control. (It is not known, however, whether the main growth direction of the cell is in the plane of the foil.) For all these reasons, this system was not chosen.

d. Au-Ni

Growth rates have been measured for this alloy (79). The morphology of the precipitate for the equiatomic alloy has recently been investigated but spacing measurements have not been published (184). At low super-

saturations, cells consist of needles of Ni-rich phase in a Au-rich matrix. At high supersaturation the Ni-rich phase assumes a spherical form. Thus there may be difficulty in deriving the v-S relation for this morphology. Sellars and Maak have measured the free energy of formation of homogeneous Au-Ni alloys down to 775°C (95). The maximum temperature of the miscibility gap is 808°C so that the free energy change on precipitation is known for 33°C of undercooling at 73 at. % Ni. Because of the difficulties suggested by the precipitate morphology, this system was not chosen.

e. Co-Ni-6Nb

Because the discontinuous precipitation occurs after Widmanstätten precipitate is well developed, and because no measurements of spacing have been made, this system is a poor choice for further study.

f. Cu-In

Figure 5 shows that the lamellar spacings measured by Böhm are larger for Cu-In than for any other system (27). This would facilitate the work on both interface shape and lamellar composition. As mentioned in section 1.7b, Böhm interpreted the x-ray line breadth of α reflections in terms of elastic strain, saying that the composition of the new phase was the equilibrium value (44). It was felt that the electron probe experiments could verify this point, since the atomic weights of Cu (63.6) and In (114.8) differ substantially.

Another feature that makes Cu-In attractive for further study is the value of the apparent diffusion activation energy shown in Table 5, 22 k cal/gm mole, suggesting boundary diffusion control. Therefore it was decided to undertake experimental work with this alloy.

3.3 A Review of the Precipitation Behaviour from α-Cu-In Alloys

a. Phase Diagram

The α-phase boundary for the Cu-In system shown in Hansen and Anderko (189), is drawn mainly from the work of Jones and Owen (163) although the diagrams are not identical, especially near the inflection point at 470°C, as shown in figure 17 a,b. The work of Jones and Owens is discussed here briefly. The x-ray method was used. A calibration was made of the lattice parameter of the f.c.c. cell versus composition using material from three regions of each of several ingots to ensure homogeneity and the reliability of the as-weighed compositions. Samples of an 11.4 at % In alloy (and others for temperatures below 400°C) were held for various times at each temperature, so that when subsequent measurements of lattice parameter showed no change with time, equilibrium was assumed. The accuracy of the boundary determination appears to be ± 0.2 at % at 260°C decreasing to ± 0.04 % at 400°C and above.

The structure of the δ phase, Cu_9In_4, appears to be a tetragonal distortion of the cubic γ brass structure, as suggested by Reynolds, Wisman and Hume-Rothery on the basis of x-ray diffraction (140), and confirmed by Corderoy and Honeycombe by electron diffraction (124). The γ brass structure can be visualized as a superlattice of 3 x 3 x 3 b.c.c. cells (54 atoms) from which the corner and center atoms have been removed, so that some of the remaining 52 atoms occupy positions slightly relaxed from the original cube corners and centers (149).

The composition limits of the δ phase do not vary with temperature as shown in fig. 17.

b. Precipitation Behaviour

The region of the phase diagram in which discontinuous precipitation occurs has been noted in Table 4. Böhm found no general precipitate for T < 0.8 T(solvus) using light optical and x-ray metallography (27, 39), but Corderoy and Honeycombe have observed by means of transmission electron

microscopy a general precipitate in 8.5 and 10 at. % In samples aged at temperatures above 250°C. Nodule growth was eventually halted by the continuous precipitate. Part of this discrepancy is due to the different resolutions of the two techniques, and part may be due to a difference in grain size, since the larger the grain, the more time available for the development of general precipitate to a resolvable size. Because Böhm detected no continuous depletion of the matrix by x-ray diffraction in the course of the cellular reaction we were not deterred from studying this alloy. (Corderoy's paper appeared after the preliminary experimental work of this investigation was begun.)

At each temperature the general precipitate particles seem to grow quickly to their maximum dimensions (about 1 x .3 x .3 μ), the density of particles increasing with time (124). The particles are not coherent with the matrix but have a habit-plane relationship {111}β || {100}α. Each particle is surrounded by a high concentration of dislocations.

The kinetics of the cellular reaction were studied by Böhm (27). His experimental methods and results are described here briefly. The growth rate was determined as the nodule radius divided by the time of anneal. The nodule radius was taken as $\frac{4}{\pi}$ times the average radius of a large number of cells (28). As will be seen this procedure involves a small error because of the finite time that is required for cells to first appear. The results of these measurements are shown in figure 46.

The lamellar spacing was determined by the method of Turnbull and Treaftis (28). The average apparent spacing S_a was first measured as the ratio of the width of a cell to the number of lamellae in the cell, althugh it was realized that this apparent spacing was not uniform across a cell. Then a plot was drawn of the number of cells, $n(S_a)$, whose apparent spacing

was less than S_a. The true spacing was taken as that value of S_a for which $n(S_a)$ extrapolates to zero. 30-50 cells were used for these measurements. In this way one overcomes the difficulty that arises because most of the lamellae are not normal to the polished surface. As mentioned, Böhm's results are plotted in figure 5. It was found that Turnbull's eq. 28

$$S = 4\sigma^{\alpha\beta}V/RT\ell n \frac{X_o^{\alpha'}}{X^{\alpha}} \quad ,$$

was not obeyed.

3.4 Results of Preliminary Experiments

In order to become familiar with the precipitation behaviour of the Cu-In system some growth rate and spacing determinations were made using light microscopy. The techniques and final results will be described later. It is sufficient to note at this point that the growth rates, v, agreed very well with those of Böhm, fig. 46. However the spacings, S, were found to be about 1/8 of those shown in curve set 4 of figure 5. Confirmation of these results appeared in the micrographs shown in reference 124.

The method of measurement used in our work differed slightly from that of Böhm. Only those areas within a cell which showed a uniform fine spacing were selected for measurement, and the minimum of the values obtained was used to ensure that the lamellae were normal to the polished section.

In addition it was found that the general precipitate was quite evident for the higher In content alloys in the range of temperatures where Böhm observed only cellular precipitate, as shown in fig. 38. Electron microscopy was not necessary to confirm this fact.

Simple preliminary experiments were performed to determine the effect of tension on the growth rate of the cellular precipitate, as has been done

with other alloys by Sulonen (17, 72). No anisotropy in growth rate was found. In fact the growth of cells was retarded slightly in all directions, indicating, perhaps, the presence of precipitate on slip planes. Therefore the growth model of Sulonen could not be checked using the Cu-In system.

3.5 Specific Experimental Objectives

Because our results disagreed with those of Böhm in two important areas, it was decided to alter our plans for the experimental program. The electron-probe microanalysis project was suspended in favour of reliable lamellar spacing determination experiments. The finer spacings would also make the probe experiments more difficult. The experimental program adopted is given below.

1. A study is made of the morphology and sequence of the discontinuous and continuous precipitation behaviour by light optical and thin foil electron microscopy. The extent to which the cellular reaction may be considered independent of the other is determined.
2. A redetermination of the kinetic parameters v and S.
3. An investigation of the shape of the $\alpha' - \alpha$ and $\alpha' - \beta$ interfaces by transmission electron microscopy.
4. A determination of the $\alpha \div$ phase composition and an estimate of its uniformity across the lamella by means of standard x-ray diffraction techniques.
5. A general search for evidence of metastability of the α' phase as depicted in fig. 7.

CHAPTER 4

EXPERIMENTAL APPARATUS AND PROCEDURES

4.1 Preparation of Specimens for Precipitation Heat Treatment

a. Materials

Table VII

Material	Source	Total Impurities as Received	Main Impuritie
Copper	Johnson, Matthey and Co., Ltd.	10 ppm	Fe, Pb, Ag
Indium	Consolidated Mining and Smelting Co., Ltd.	10 ppm	-

b. Alloy Preparation

The copper and indium were cut from stock by means of a jeweller's saw an knife, respectively, after which they were etched in nitric acid, rinsed and dried. Weighings were made accurate to 0.1 mg.

The apparatus used to prepare the alloys is shown schematically in Figure 18. The description and principles of operation follow.

The helium gas was used as a coolant to quickly solidify the alloy within the crucible 7. The purpose of component 2 was the deoxidation of the gas at a rapid rate. To do this the gas was first heated by the massive bundle of tubing, 2a, then passed over the large area of copper turnings 2b and finally over a water cooled coil 2c.

The crucible 7, machined from National Carbon Co. (Union Carbide) grade AUC graphite, had a capacity of about 16 gm. of alloy. Before materials were added, the crucible was cleaned by induction heating to about 1500°C under vacuum until a low pressure could be maintained (about 10 minutes).

To prepare an alloy, material was placed in the crucible, and the system was evacuated, then flushed with helium. The gas cleaning furnace was heated up and the gas flow rate set at a low level. The materials were induction melted slowly, so that the vapour pressure of the unalloyed indium was not raised quickly. When molten the material was stirred by the induced currents for about one minute. The power was switched off and the gas flow rate increased for quick solidification of the alloy. The ingots always emerged bright. The following nominal compositions in % indium by weight were prepared:

5.13

8.97

12.70

16.58

Less than 1 mg. of material was lost on melting each alloy.

c. Specimen Preparation

The quickest way of reducing an ingot to a useful form was found to be hot rolling.

A set of grooved rolls was used which was kindly loaned to us by the Canadian Westinghouse Co. in Hamilton. The grooves ranged from about 0.30" to 0.04" diameter.

A small Vycor tube furnace was built as shown in figure 19. The ingot was placed in the cool portion of the tube which was then flushed

with argon. A push rod was used to position the ingot at the thermocouple. When the ingot reached 600°C, the furnace was tilted about the pivot so that the ingot could be quickly removed and passed through the rolls. After one or two passes the alloy was returned to the furnace and the cycle repeated. This procedure resulted in an almost scale-free rod reduced in area by a factor of 8.

The material could then be cold rolled. One half of the rod was reduced to rod of the minimum diameter of 0.04". This material was cut up and used for optical microscopy studies. The other half was flat rolled to 150μ strip after an anneal at 650°C. This material was used for transmission electron microscopy studies. The smoothest rolls were used for this purpose and their parallelism was carefully checked.

One of the alloys was partially melted by overheating during the homogenizing treatment (described below). This alloy was salvaged by the following method. The alloy was levitation melted in 2 gm. lots in a helium atmosphere and then solidified by dropping onto a cold brass plate as shown in figure 20. The help of S. Shiraishi is acknowledged here. The solidification was quick enough to restrict long range segregation so that the material could be cold rolled to sheet material.

d. Homogenization and Grain Size Control

The study of discontinuous precipitation requires reasonable control of the grain size of the homogenized material. For growth rate measurements, especially at lower temperatures, where the rate of formation of nodules is relatively high, a large grain size is preferred so that nodules can grow without impingement. For electron microscopy (and at higher temperatures) a smaller grain size is essential if there is to be a high probability that

a cell will be in a section thin enough to be transparent to electrons. Therefore the sheet material was homogenized for shorter times and at lower temperatures than the rod material. This practice was compatible with the smaller diffusion time required for the sheet. In annealing the rods, care had to be taken to hold the sample below 670°C for some time to ensure that any high indium regions did not melt. The ideal grain distribution in the rods was for the boundaries to traverse the complete diameter. This situation was seldom obtained, however, because thermal grooving anchored a layer of smaller grains near the surface.

Preliminary experience showed that the discontinuous reaction was substantially suppressed in samples deformed even slightly after homogenization. Bands of precipitate were observed to outline the slip traces. Therefore care was taken in the homogenization treatment. Sheet material was cut into rectangles 2 x 0.5 cm and placed in "accordions" of .005" molybdenum strip shown in figure 21a. This material served as mechanical protection, and prevented welding during annealing. Graphite separators served the same purpose for rod specimens. These components were protected further by a cylinder formed from .010" molybdenum sheet, figure 21c. The enveloped specimens were then sealed under a vacuum of 10^{-5} torr. in Vycor tubing to ensure a bright anneal.

The specimens were homogenized in a standard horizontal tube furnace, whose temperature could be monitored independently of the control thermocouple, and which could be muffled at each end to prevent convection. The annealing treatments are tabulated below.

Table VIII - Homogenizing Treatments

Composition wt % In	5.13	8.97	12.70	16.58
Sheet and Rods				
Temp.	630°C	640°C	650°C	650°C
Time	20 hr.	28 hr.	10 hr.	8 hr.
Rods only				
Temp.	890°C	no rods	760°C	650°C
Time	5 day		5 day	5 day

After homogenizing, the specimens were quenched in the device shown in figure 21d. The Vycor capsule was placed in the "U" of the jig, and the hinged top was lowered quickly to break the glass as the water sprayed from the jets. The distance of interference between the lid and the capsule was about 1/16" so that the molybdenum cylinder could protect the samples. As a result the samples emerged bright and undamaged.

The grain size of sheet material was about 0.15 mm. and that of rod material was about 0.5 mm. The average grain diameter is taken as 5/3 times the length of a random line divided by the number of grain boundaries intersected by that line in a polished and etched surface (42, 59).

4.2 Composition Determination

a. Homogeneous Alloys (α' phase)

The composition of each alloy was checked by the standard Debye-Scherrer x-ray diffraction technique, using the lattice parameter versus composition data of Jones and Owen (163) which is shown in Table 9.

Table IX - Lattice Parameter for α Cu-In Alloys

Indium, at. %	Lattice Parameter	
	KX at 18°C	A° at 18°C
0.00	3.6074_s	3.6147_4
2.0_0	3.6269_8	3.6343_6
4.0_1	3.6455_7	3.6529_3
5.8_7	3.6623_8	3.6697_8
7.6_1	3.6786_1	3.6860_4
8.4_9	3.6974_4	3.6948_9
9.0_0	3.6913_8	3.6988_4
9.8_2	3.6991_8	3.7066_5
10.5_0	3.7046_0	3.7120_8

It is seen that 10 at. % In. increases the lattice parameter by about 0.1A so that an uncertainty of $\pm$ 0.0005A means that the composition is determined to within 0.05 at. %.

The reliability of the lattice parameter determination was increased by using a copper target with a copper filter of thickness .015 mm. rather than a nickel filter. This procedure actually permitted the use of four wavelengths: Cu-$K_{\alpha 1}$, Cu-$K_{\alpha 2}$, Cu-K_β, W-L_α. The last wavelength resulted from evaporation of the tungsten filament material onto the target in an older x-ray tube. As a result there were 12 high angle lines instead of 6 (including one at $\theta \sim 80^\circ$) from which one could extrapolate to obtain precise lattice parameters (i.e. to within .0005A).

The specimens for this study were snipped from sheet material, with 2 or 3 slivers glued together to obtain the optimum thickness of about 0.3 mm. A 155 mm. diameter camera was used with exposures ranging from 10 to 40

hours, depending on the generator and beam port available. Some of the specimens were homogenized material, and some had various partial precipitation treatments. The results of these measurements are given in Table 10.

Table X - Alloy Compositions

As Weighed		Determined by X-ray Diffraction
Wt. % In	At. % In	At. % In
5.13	2.99	not determined
8.97	5.17	$5.13 \pm .04$
12.70	7.45	$7.51 \pm .10$
16.58	9.96	$10.07 \pm .10$

It is seen that the deviations for the average of several samples in the higher indium alloys are somewhat greater than that due to the technique of measurement. It may be that the practice of solidifying the ingot in the crucible, rather than chill casting, resulted in a macroscopically segregated structure which could not be removed by rolling and homogenizing. From section 3.3a we recall that the uncertainties in the phase diagram are of the same order as those above. Therefore, calculations involving both the initial and equilibrium compositions will have uncertainties somewhat greater than those given in Table 10.

b. Partially Precipitated Alloys (α phase)

The use of samples which have undergone partial precipitation treatments results in the extra diffraction lines from the α and δ phases, from which one may calculate the compositions of the α phase. There is a difficulty here, however. For intense lines from the α phase one needs

fine-grained samples precipitated for longer times, during which the α formed initially may relax to the stable equilibrium composition. Therefore samples were chosen for which α lines were just resolvable in the hope that these preserved the original composition distribution.

At lower supersaturations another problem arose from the lower rate of nucleation of cells in comparison to the rate of growth. The diffraction lines were spotty from the few orientations of α available at the Bragg angle.

4.3 Precipitation Heat Treatment

Apparatus for the precipitation treatments must do the following:

a) bring the sample to temperature relatively quickly,

b) hold the sample at temperature, allowing little oxidation, especially in thin sheet specimens,

c) quench the sample to preserve the cell-matrix interface.

Two types of furnace were used to meet these requirements. When a high growth rate v was expected, so that only short precipitation times were needed, a stirred $NaNO_3$ and $NaNO_2$ salt bath was used. The temperature was uniform to within about 1/2 inch of top and bottom of the bath, and remained constant for several hours when the furnace was protected from strong drafts. The voltage from a double thermocouple was continuously recorded so that any variations could be detected. Periodically a chromel-alumel thermocouple was also used with a manually operated potentiometer to accurately measure the temperature. This thermocouple was calibrated at the melting points of tin, lead and zinc. The salt pot was used for precipitation times up to 11 hours. The samples were quenched into water. They emerged with an oxide scale that could usually be removed by etching or electropolishing.

For long heating periods the specimens were sealed in Pyrex tubing using an inert gas atomosphere or a vacuum. A forced convection furnace, Blue M type CW1412, was used to provide a uniform constant temperature. Again the temperature was continuously monitored and accurately measured. In this case the time required to reach the required temperature ranged up to 10 minutes, but this was not considered a serious error when the total precipitation time ranged from 10 hours to 35 days. Over the longest periods some temperature drift was inevitable. The samples were quenched using the device shown in figure 21d.

The details of the heat treatments for each alloy, including time, temperature and its variation, will be given in section 5.2 with the results of the quantitative metallography.

4.4 Metallographic Techniques - Light Microscopy

a. Surface Preparation

The rod samples were prepared for examination by standard techniques: mounting in thermoplastic or thermosetting materials, wet grinding on 4 grades of silicon carbide papers, and diamond polishing with kerosene lubricant. Final polishing consisted of either alternated etching and 1μ diamond polishing, or electropolishing. The following were found to be suitable etches:

(1) CrO_3 - 25 g
HNO_3 - 40 g
H_2O - 100 ml (185)

(2) $K_2Cl_2O_7$ - 2 g
NaCl - 1.5 g
H_2SO_4 - 8 ml
H_2O - 100 ml (186)

The electropolishing solution was

HNO_3 - 1 part

Methanol - 2 parts

Temperature $\leq -20^{\circ}C$

Polishing Voltage 5 - 8 v

Etching Voltage 2 v

Electropolishing was found to yield better results although contrast between grains of the same phase was sometimes poor.

Sheet specimens were used for light microscopy when the smaller grain size was an advantage. These specimens were not mounted and sometimes were not flat. They were prepared by electropolishing.

b. Techniques of Measurement

A Reichert Universal Camera Microscope Me F was used for measurements and photography.

Measurements of length were made in three ways:

1) using a Vickers 6X eyepiece containing a grid which yielded a resolution of 1 part in 60, or 0.3 μ with the highest power objective lens.

2) using the projected image on the ground glass screen, on which a 10 cm rule may be used.

3) using micrographs, on either 4 x 5 inch film or 35 mm roll film.

All these measurements were calibrated using the stage micrometer. The eyepiece was used mainly for nodule size measurements, i.e. for lengths greater than 5 μ, since this was the quickest way of taking a large number of readings as discussed in section 5.2 below. The projection methods were more suitable for spacing measurements where one scans a great number of cells, but makes measurements on relatively few. The 35 mm film offered the advantage of speed, but had the disadvantage of difficult focussing and poorer resolution.

If the spacing was measured as the average of, say, 10 lamellae, then values greater than 0.3 μ could be obtained to ± 0.03 μ. Regularity seldom extended over a larger number of lamellae.

The fraction of grain boundary occupied by cellular precipitate, G, was also measured. G = 1 when cells have grown in both directions from all grain boundaries. The sample is traversed across a fixed point in the image plane (an intersection on the eyepiece grid) with the micrometer drive, and the number of grain boundaries intersected N_1 are counted. On the return drive, the number of cell intersections N_2 are counted. From the definition of G and the theory of lineal analysis

$$G = \frac{N_2}{2N_1} \quad .$$

From N_1 and the length of traverse ℓ the grain diameter may be calculated as

$$d = \frac{5}{3} \frac{\ell}{N_1} \quad .$$

The initial grain boundary precipitate is ignored in the determination of N_2.

4.5 Metallographic Techniques - Electron Microscopy

a. Thin Foil Preparation

Duplex copper indium alloys may be thinned using techniques found suitable for several copper based alloys (102, 103, 104). Some of the conditions described are more strict than those given in the references, and were necessary for successful thinning. Some of the more elaborate techniques described in the literature were omitted since no improvement accompanied their use.

The so-called "window technique" was used, for which the oblong sheet specimen was most suitable. The polishing cell was set up as shown in figure 22a. The electrolyte was the same nitric acid and methanol solution

described in the last section. The cell potential was 5 - 6 volts, and the temperature was kept below - 30°C, which is lower than for other copper alloys. The specimen was not agitated, except to remove an initial black anodic film, but was supported loosely so that it could be quickly removed at the right moment.

The specimen was held by a flat jawed clip and given a first outline coating of Microstop lacquer (Michigan Chrome and Chemical Co., Detroit). Polishing was continued until metal was completely dissolved away in a band adjacent to the upper Microstop coating figure 22b. The sample was rinsed, dried, inverted and given a second coating as shown. Ideally, subsequent polishing resulted in one or two very thin tongues of metal foil, but often other regions (near holes or edges) were also suitable for microscopy. With the voltage still on, the sample was then quickly transferred to a beaker of clean methanol cooled with dry ice and agitated. A second and third cold rinsing bath ensured removal of the electrolyte. The specimen was gently removed from the clip and left in the last cold beaker of methanol until ready to cut. This procedure prevented the formation of a thin oxide layer which imparted a speckled appearance in the electron microscope to an otherwise featureless specimen, and which also resulted in additional diffraction spots.

N.B. - Thomas (102) suggests covering the surface of the electrolyte with liquid air before removing the specimen from the polishing cell. This dangerous practice did not result in an improved thin foil.

The sample and cold methanol were transferred to a shallow dish placed on a light box. Watchmaker tissue was loosely folded about the specimen. A foil was cut from the sample with a scalpel using a rolling rather than a drawing action. The cut foil and tissue were transferred to a dry dish and

and rinsed with a jet of acetone. After drying, the specimen was dropped into the electron microscope specimen holder in which was placed the coarsest grid consistent with adequate specimen support.

The rest of the specimen was dealt with in one of several ways. If further electropolishing was planned it could be left in the last methanol dish. If further cutting was planned within a short time it was suspended in a capsule in a dewar of liquid nitrogen. The sample was prepared for longer storage by a 10 second ultrasonic cleaning in ethanol, after which it was stored in a vacuum desiccator. This cleaning removed the last traces of acid from under the Microstop lacquer.

The above procedure was suitable for all compositions and treatments of copper-indium alloys. Some preferential polishing of the α phase was inevitable, however. In a recent publication a method for the even polishing of multiphase alloys is described by Ginn and Brown (190). Most of our work was completed before this method became known.

b. Microscope Operation

A Siemens Elmiskop I was used in this study, operated at 100 Kv. The magnification was calibrated from a series of photographs of a carbon replica of a diffraction grating for the projector pole-piece III. The rotation was determined as a function of magnification setting using these photographs and pairs of microscopy and diffraction photographs of the (111) twin plane between crystals in the (110) orientation.

c. Spacing Determination

Using light optics one defines the true lamellar spacing as the minimum observable spacing within a nodule. Using transmission electron microscopy one can readily determine whether the lamellae are normal to the

foil surface. Figure 23 shows that the α-δ interfaces yield contrast effects. Even when these effects are not distinguishable from the dark δ phase, obliqueness is revealed by an apparent fraction of δ greater than expected from the application of the lever rule.

CHAPTER 5

EXPERIMENTAL RESULTS

5.1 Morphology and Sequence of the Discontinuous and Continuous Precipitate in Copper Indium Alloys

a. Morphology of the Discontinuous Precipitate

Cellular precipitate does not initially exhibit regular cooperative growth. It is usually preceded by a more disorganized grain boundary precipitate whose average "spacing" exceeds that within the cell. Figure 24 (7.5 at % In, 404°C) shows such a grain boundary precipitate evolving into cells at a few points after 86 minutes. At 290 minutes figure 25 shows the achievement of cooperation, the coalescing of adjacent small cells, and the growth of cells from both sides of the original grain boundary. Figure 1 (the same alloy at a later time and a higher temperature) shows the development of cooperation and that several growth directions can exist in a single cell. It is probable that only the central portion of this cell is growing in the plane of the micrograph. Figure 26 shows the beginning of a cell in transmission electron microscopy. We see that the α phase of the cell has the same orientation as the α' parent grain (light contrast), and the region between the two phases is populated by a relatively high dislocation density, rather than a boundary. The advancing interface and precipitate distribution is still irregular for this cell. No coherent general precipitate with the associated elastic strain field is visible. Therefore we may reject the proposal (1, 36, 37, 132) that discontinuous precipitation is a recrystallization reaction in the literal sense.

That the boundary precipitate, as well as the cells, develop by means of boundary diffusion is shown by figure 27. A 7.5 at % In alloy was held at 447°C for 23.5 hrs., quenched and then held at 330°C for 10 hrs. In the first heating the dark irregular boundary precipitate developed, in the second the nodules grew. It is seen that the beginning of the nodules outlines the position of the $\alpha - \alpha'$ boundary as it was at the end of the first treatment. This boundary bowed out between precipitate particles to supply them with solute. Hence the cells grew only on one side of the boundary, avoiding the depleted region. This occured although the boundary precipitate spacing ($\doteq$ 11μ) is about three times the cellular precipitate lamellar spacing (3.8 μ) at the same temperature (447°C). Under these circumstances volume diffusion in the vicinity of the first precipitate might have been expected to contribute to the solute flux. However, at 330°C the cells grew at the same rate as in samples with no prior treatment at 447°C, showing that no appreciable depletion occurred in this region.

One feature of nodule growth is the frequent observation of fine twins within the cells, as shown in figure 28. These are also visible in light microscopy if the cells are dissolved back by reheating as shown in figure 29. [Dissolution behaviour is discussed in Appendix A.] Figure 30 shows the early formation of twins between the boundary precipitates. We believe the twins form either as accidents of growth or to enable the nodule to change growth direction, i.e. so that the α phase may simultaneously have an incoherent interface with the α' matrix and a good fitting interface with the δ phase.

In figure 1, the spacing appears quite uniform in the central portion of the cell. Electron microscopy seldom reveals a uniform spacing as indicated in figure 54 h. Here individual lamellae may vary by more than a

factor of two, but groups of just three lamellae differ by less than 20%, so that we may safely take the average value in reporting the spacing measurement in section 5.2.

b. The General δ and δ' Precipitates

Figure 31 illustrates several features of the general precipitate. Each particle appears platelike (lying in the {100} planes), is surrounded by dislocations and has the same size as its neighbour, as observed by Corderoy and Honeycombe. When edge-on these plates show typical strain field contrast, which suggests that there exists at least partial coherency across the habit plane at this stage of the aging process.

The density appears uniform except at the upper left corner of the micrograph where the foil is thinner, and near the grain boundary where a zone 1.3μ wide is free of precipitate. This precipitate-free zone has been the object of study by Embury and Nicholson for the system Al-5.9 % Zn-2.9 % Mg by weight (125). The authors suggest that the nucleation of the precipitate requires the presence in the lattice of a certain vacancy concentration in excess of the equilibrium value at the aging temperature. At the homogenization temperature the vacancy concentration is increased, but on quenching the solubility of vacancies is decreased so that they tend to diffuse to the high angle grain boundaries which are good vacancy sinks. Therefore at the precipitation temperature a zone adjacent to a grain boundary lacks sufficient vacancies for precipitate nucleation to occur, and the remainder of the grain has a vacancy excess which permits such nucleation. Without becoming too involved in this interesting aspect of precipitation in Cu-In alloys, we were able to find some evidence to confirm this model. Figure 32 shows a twin boundary consisting of coherent and incoherent segments. Assuming that only the latter can act as vacancy

sinks explains the observation that precipitate free zones surround only the incoherent segments.

Figure 31 also shows an array of boundary precipitates which are parallel to one of the orientations of the general precipitate in the same grain. This is an infrequent occurence, but does not exclude cell formation at the same grain boundary.

Hitherto there have been no observations of an early stage of the general precipitate. Figures 33, 35, 36 and 37 show a contrast effect which we believe to be such an early stage and shall arbitrarily call δ'. This feature was observed only in the thinnest sections, as shown by a comparison of the density of general precipitate in figures 31 and 33, which depict different grains of the same specimen, and by the fact that these fine features fade out in the thicker regions of the foil of figure 33. The foil orientation at which δ' was visible was near the {110} orientation, with a slight tilt about the [111] direction lying in the plane of the foil. Figure 34a is a diffraction pattern of the area of figure 33, and figure 34b is that of an area not showing the fine precipitate. These particles are seen by dark field microscopy figure 35 using one of the strong (111) diffracted beams. The thickness dependence of the contrast is quite noticeable in this micrograph. In figure 36 the precipitate appears to have both a "positive" and "negative" sense. This type of feature has been explained by the dynamical theory of electron diffraction as arising from the proximity of the particle to the upper or lower foil surface (193). The particles do not appear like the classical discs of condensed vacancies or small dislocation loops. In figure 37 the interaction of dislocations from the large general precipitate particle with the δ' precipitate is evident.

We have not been able to determine the temporal development of δ',

nor its copious existence in aged alloys of composition other than 10 at % In. Obviously the large δ particles must have an early stage of development and it is not unreasonable to assume that δ' is that predecessor.

c. The Effect of the General δ and δ' Precipitate on the Cellular Precipitate

We shall consider in this section the extent to which the δ significantly affects the growth of the cellular precipitate. It should be appreciated that the longest aging times used for growth rate measurements are from 1/5 to 1/10 of the time characteristic of the peak mechanical properties as measured by Corderoy and Honeycombe (124). In these short times the mean distance between δ particles is usually much greater than the spacing shown in figures 41, and it will be seen later that the distance of nodule advance remains a linear function of time for all but one composition and temperature treatment. Figure 38 illustrates the dispersion of δ in this exceptional case. Figures 39, 40 and 41 show δ particles in the vicinity of, encountered by and wholly within advancing cells. It is seen that the general precipitate disturbs cooperative lamellar growth only locally. In particular no large spacing variations are noted in the vicinity of a δ particle, showing that the supersaturation is not relieved over large distances. This may also be inferred from the way that the general precipitate develops, mainly by increasing in density rather than in size.

The effect of the fine δ' precipitate can not be the same however. Here the spacing between particles is about the same as the lamellar spacing. The advancing cell can see the average of a composition fluctuation over these small distances because of the boundary diffusion mechanism. The matrix should appear to have slightly less supersaturation since some free energy has been released in the δ' precipitation process. From the following

kinetic results we cannot estimate the magnitude of this effect. We will be able to say that it is not significantly time dependent. Indium increases the lattice parameter in a copper alloy, and has a larger atomic scattering cross section for electrons. Therefore one would intuitively expect even small clustering tendencies to be easily detected in the electron microscopy. Because the detection of δ' is difficult we may tentatively conclude that the δ' precipitation process involves but a small amount of solute segregation, and hence a small change in the free energy of the α' matrix.

We summarize this section by saying that the interaction of the δ and the discontinuous precipitation process conforms to group 3 (Table 4) as discussed in section 1.4, and that the δ' interaction conforms to group 2 (Table 3).

5.2 Grain Boundary Occupation and the Determination of Growth Speed

Values of G, the fraction of grain boundaries occupied by nodules, are given in Table 11. In general, G increases with time and decreases with temperature. As an illustration, figure 42 shows a striking difference in G for equal values of growth rate v. It is emphasized that these values are not used in any comparison with the theory, but are useful for the choice of grain size and precipitation time in preparing alloys for electron microscopy. They also aid in the determination of v.

Both Cahn (42) and Sulonen (144) have considered the problem of estimating the nodule growth distance from measurements of cell size in a two dimensional section. What follows is a specific application to the present work.

When G is low, cells are individual and the representative distance of advance can be taken as that of the largest nodule visible. Those that

appear smaller have either been sectioned at a level other than that corresponding to the largest diameter, or are late starters, or have a growth speed smaller than the largest nodules. Should the grain boundary from which the cell is growing not be normal to the polished section, no great error is introduced into the estimate of growth distance. When G is high, the cells coalesce and grow as slabs from the boundary. The representative distance of advance is now more difficult to determine, since the largest apparent slab width may be due to oblique grain boundaries. Therefore we must take a distance smaller than the largest, still keeping in mind the late starters and slow growers. Accordingly measurements are made of several slab widths and a histogram is plotted of the length of grain boundary occupied by each slab width, as in figure 43. The tail of the distribution is made up of two parts, that due to obliqueness of thinner slabs and that due to the fewer thick slabs. Beyond a certain distance we expect only the first contribution, and the estimation of this distance is aided by noting the appearance of the larger slabs. If the advancing front is ragged, they are probably not normal to the polished section.

There is an added difficulty in estimating the true growth distance. Measurement should be made in the direction of cell growth, which in general, is neither normal to the original grain boundary, nor in the plane of section. If a slab is normal to the section plane then the growth distance is larger than the slab width. Therefore this error tends to cancel the previous one. One may conclude that the inferred growth distance may be considered accurate to within about 20%. The values obtained for growth distance as a function of composition, temperature and time are listed in table 11. These values are plotted as a function of time to yield the growth velocity as the slope, and an initial delay time. Two examples

are given in figure 44, showing one essentially linear graph as well as one corresponding to figure 38, in which the general precipitate affects the discontinuous reaction at long times. The initial delay times are associated with the development of cooperative growth from the more widely spaced grain boundary precipitate. The values of growth speed are tabulated in table 12 and plotted as a function of temperature in figure 45, and of composition in figure 46. Some of the values for figure 46 are obtained by interpolation in figure 45. The comparison with the results of Böhm (27) is made in figure 46. It is seen that the present work suggests a more regular behaviour of v. For the 7.5 at % In alloy it is seen that the growth speed rapidly tends to zero as the temperature increases towards the solvus temperature.

Table XI - Kinetic Data for Discontinuous Precipitation in Cu-In Alloys

Composition at. % In	Temperature °C	Time	Grain Size mm.	% of Boundary Transformed	Distance of Nodule Advance μ
5.13	249.0±0.5	3.0 day			1
	"	9.7 "			3.6
	"	20.8 "		24	14.3
	247.±2	36.0 "	.12	39	56
	341.2±1.0	4 hr	.08		3.1
	"	9 "			7.3
	"	18 "	.04		14.6
	392.0±1.0	48.3 hr	.13	17	41
	"	91 "	.125	25	80
	448	76 hr	No precipitate at 600X		
7.51	249.0±.05	17 hr			<1.5
	"	41.5 hr			4.0
	"	146.0 "			10.7

Table XI (cont'd)

Composition at. % In	Temperature °C	Time	Grain Size mm.	% of Boundary Transformed	Distance of Nodule Advance μ
	329.3±1.0	1.0 hr			<1.5
	"	3.1 "			5.4
	"	5.8 "	.22		14.3
	"	11.0 "	.11		42
	403.9±1.0	1.5 hr			5
	"	4.25 hr	.25	14	43
	"	4.8 "			34
	"	10.3 "			120
	421 ± 1	1.25 hr			3.9
	"	4.3		<2	19.5
	"	11.3		14	80
7.51	432.2±1.0	5.2 hr			27
	"	11.4 "	.18	3.3	47
	"	15.9 "	.14	8.7	66
	447.0±1.2	10.5 "			0
	"	23.5 "			0
	"	47.4 "			3.2
	"	129 "			16
	461.4±.06	72 "			10
		232 "			0
	472.5±1	120 "	No nodules.		
10.07	246.0±1.0	21.5 "			0
	"	69 "	.63	<1	6
	"	207 "		36	15
	329.3±0.9	24 min			0
	"	48 "	.67	17	4
	"	310 "	.58	54	48
	403.9±0.3	15 min	.4	19	8.4
	"	60 "	.57	34	52
	"	230 "	.51	94	150

Table XII - Kinetic Variables of Discontinuous Precipitation in Copper Indium Alloys

Variable	Temp. °C	5.1 %	7.5 %	10.1 %
Growth Speed	246 ±1.0	-	-	2.0×10^{-9}
cm/second	249.0± .5	1.8×10^{-9}	2.1×10^{-9}	-
	329.3±1.0	-	1.2×10^{-7}	2.7×10^{-7}
	341.2±1.0	2.3×10^{-8}	-	-
	392.0±1.0	2.8×10^{-8}	-	-
	403.9±1.0	-	3.8×10^{-7}	1.7×10^{-6}
	421 ±1	-	2.2×10^{-7}	-
	432.2±1.0	-	1.25×10^{-7}	-
	447 ±1.2	-	5×10^{-9}	-
Spacing-μ	246 ±1.0	-	-	0.0745
	249.0± .5	.13	.091	-
	329.3±1.0	-	.13	0.099
	341.2±1.0	.30	-	-
	392.0±1.0	.55	-	-
	403.9±1.0	-	.32	0.175
	421 ±1.0	-	.42	-
	432.2±1.0	-	.59	-
	447 ±1.2	-	3.8	-
	461.4±0.6	-	5	-
	472.7± .5	-	-	.52
Temp. at which 1/S → 0 (°C)		432±10	450±5	505±10
Solvus Temp (°C)		454± 2	488±3	554± 3

5.3 The Lamellar Spacing and the Precipitation Behaviour at Low Supersaturation

The results of the lamellar spacing measurements are listed in the table 12 and plotted to figure 5 to compare with the values for other alloys, and those of Böhm for Cu-In. The factor of eight discrepancy as mentioned in section 3.4 is clearly seen.

The results are also plotted separately in figure 47, with the values of the solvus temperature marked for each composition. It is seen that the spacing extrapolates to an infinite value (1/S = 0) at a temperature below the solvus. These values of temperature are also listed in table 12 and plotted on the phase diagram, figure 17b. Because this feature is most interesting, attention is concentrated on the observations at low supersaturation. For the 5.13 at. % In no precipitate was seen at 448°C after 76 hours. The 7.5 at % alloy yielded recognizable cells at 447°C, a single rudimentary nodule in one of the samples at 461°C, figure 48, and only grain boundary and grain corner precipitates at 472.5°C, figure 49. A 3.0 at % In alloy was prepared and samples held at 357.5°C for 76, 148 and 213 hours. No cells were observed, only grain boundary precipitates. The precipitates, as well as those of the 7.5 at %, 461° treatment were noted to cause a shifting of the original grain boundary as shown before in figure 27, demonstrating the continued importance of grain boundary diffusion. Figure 49 shows that the 7.5 % - 472.5°C sample has relatively smooth grain boundaries which suggests a volume diffusion mode of material transport.

Thus we may conclude that cellular precipitation does not persist to the limits of the two-phase region. Only for the smallest supersaturations, however, is boundary diffusion unimportant.

Electron microscopy allows us to try to determine whether or not a unique spacing exists for a given precipitation treatment. Figures 50 and

51 show two cells in the same sample, the first of which has a spacing of 0.091μ, the second, 0.16μ. The micrographs show that in neither case are the α - β interfaces normal to the foil, and that possibly the finer spaced lamellae are more oblique than the coarse. We may tentatively conclude that a unique spacing does not exist, and therefore our tabulated measurements refer to the finest of a range of values. It is not known whether these values correspond to the growth rates measured. If a spectrum of v exists as well, we can only measure a value near the maximum. The clarification of this aspect of the kinetics will have to await improved experimental methods. In the discussion of the results it will be assumed, however, that the values of v and S do indeed correspond to the same growing cell.

5.4 The Composition of the α - Phase

The results of the X-ray determination of the α- phase composition are shown in table 13 and plotted on the phase diagram, figure 17b. The finest grained material and the maximum times for each composition and temperature as shown in table 11 were used. Even so, the intensities of lines from the α- phase were often low. These might have been improved if a two-step homogenization treatment had been undertaken. An intermediate cold rolling and a second short anneal might have yielded a finer grain size for all but the higher In alloys where the solvus temperature is fairly high.

Table XIII - The Composition of the α- Phase of Cellular Reaction Product in Atomic Per Cent Indium.

Temperature °C	Alloy Composition		Equilibrium Composition
	7.51	10.07	
	α - Phase Composition		
246		1.38	1.1
249	2.9[1]		1.1
329.3	2.06	2.51	1.28
403.9	4.2[1]	3.25[2]	2.56

Notes

1. These values are uncertain since the diffraction lines from the α- phase were quite weak.
2. This sample may have been held too long at temperature, allowing a relaxation of the nonequilibrium composition, since the CuK_α doublet was resolved as shown in figure 52 and discussed below.

The variation of composition within the sample may be estimated from the width of the diffraction lines, assuming all of the line broadening is due to a variation of composition and not to particle size or lattice strains. It is recalled that Böhm assumed the last cause, after first stating that the α- phase had the equilibrium composition. Figure53, a portion of the diffraction pattern of the 7.5% - 329°C sample, shows that the $Cu\text{-}K_\alpha$ doublet is resolved for the lower angle α'- phase but not for the α- phase. Assuming the minimum line breadth consistent with the blurring of the doublet, $\Delta\theta = \pm 0.2^\circ$, we may calculate the minimum composition variation to be

$$\pm \Delta X^\alpha = \frac{dX}{da}\, a \cot\theta\, \Delta\theta = 0.42 \text{ at \%}$$

where a is the lattice parameter, and $\frac{dX}{da}$ is found from table 9.

The problem of the composition variation in the α phase was briefly pursued further. This work is discussed in Appendix B.

The x-ray patterns from the α' - phase on the same films verified the lack of any significant loss of supersaturation by continuous precipitation. For example a 7.5%, 461.4°C, 72 hour sample had a composition 7.56 ± 0.08%. Homogenizing the same sample yielded a composition 7.42 ± .08%. After the first heat treatment general precipitate particles are clearly visible at 200X.

We may conclude from these x-ray experiments that the α' - phase retains its initial composition, during the course of discontinuous precipitation

and that the α - phase composition exceeds the expected equilibrium value and probably varies within a cell.

5.5 The Advancing Interface

Figure 54 shows several examples of the advancing interface. The difficulties in the quantitative evaluation of the shape are obvious, due partly to variations from one lamella to the next, and partly to the angle of section. If the average plane of the interface is tilted with respect to the foil about an axis in the growth direction, then the center of the interface appears flattened and the angles at the three phase juncture are blurred. If the tilt is about an axis in the foil and normal to the growth direction then the interface may appear fringed, figure 54 a,b,d,g and the angles at the juncture appear exaggerated.

Nonetheless several important observations on the shape may be made. The interfaces appear similar to the shapes calculated by Hillert (23) for pearlite growing by volume diffusion under the assumption of local equilibrium, as shown in figure 55. In particular, although some interfaces are convex toward the α' phase all across the lamellae, many are concave at the center. This corresponds to the case where the spacing is larger than that which yields a maximum growth rate. In either case, the curvature usually increases from the center to the edges of the lamellae. At these places the radius of curvature is as little as 1/10 the spacing. This value may be high due to the obliqueness mentioned in the last paragraph. For the same reason values of the angles θ^{α} (figure 14) range from a few degrees to 40°. One cannot determine the relative value of $\sigma^{\alpha\beta}$ from such measurements, but the fact that mechanical equilibrium is obtained at the juncture is shown in figure 54a, where the average interface direction is not normal to the lamellae. It is seen that the $\alpha - \alpha'$ interface curves

sharply at points like A_9 in order to meet the $\alpha - \beta$ interface at the proper angle.

A final word should be said on the question of whether these micrographs represent the shape of the interface at the temperature of growth or whether some alteration occurred in the final quench. This uncertainty is less important here than for the pearlite reaction where the fastest growth rates are several orders of magnitude greater than any here. For example, the fastest growth rate in our work is about 2×10^{-6} cm/sec so that in 1/10 second the interface can advance only 20 A. The interfaces in air cooled samples were examined and revealed no great differences from those shown here.

CHAPTER 6

DISCUSSION

6.1 Introduction

In Chapter 2, three steady state growth models for discontinuous precipitation were presented. Turnbull's dimensional equation 27 is simple to apply. No assumptions are made about mechanism or thermodynamics except for boundary diffusion control and the arbitrary prediction of lamellar spacing. In particular no explanation is given for the final composition of the α phase or the repeated discontinuous reaction in Pb-Sn alloys. Cahn's model assumes boundary diffusion, reaction control and a maximum rate of free energy decrease. No simple equation can be tested, but the dimensionless parameter β may be checked for consistency among the growth variables. The final model assumes boundary diffusion and local equilibrium in a metastable monotectoid system. The optimization problem is discussed but no conclusion is reached concerning the correct formulation of such a principle for this reaction. In the remainder of this chapter we discuss the relative merits of these models using our experimental findings.

6.2 Turnbull's Model

Equation 27 may be rewritten as

$$bD_B = \frac{X^{\alpha'}}{X^{\alpha'} - X^{\alpha}} vS^2$$

in which form it was used in Chapter 1 to evaluate the diffusion activation energies for various systems. It is recalled that the value for Cu-In using the spacing and growth rates of Böhm was about 21 Kcal/gm. mole, a reason-

able value for boundary diffusion. The same calculations are performed here, and the values of bD_B are plotted on a log scale as a function of $1000/T^{\circ}K$ along with the boundary self-diffusion data for silver in figure 56. The following observations may be made.

(a) The absolute value of bD_B is about 1/4 to 1/100 the value for silver grain boundary self diffusion (168). The data for silver was chosen since it has a melting point close to the average solidus temperature of Cu-In alloys. We consider the numerical agreement fairly good since Turnbull's equation is only a dimensional one and may therefore require a large corrective numerical constant, and since we are concerned with different diffusing species along phase rather than grain boundaries.

(b) The curves for each alloy almost overlap. This shows that initial composition has little effect on the apparent boundary diffusion coefficient between phases of different composition.

(c) The curve for 7.51% rises less steeply at higher temperatures. This behaviour was suspected to be associated with the anomolous increase in the lamellar spacing, and the accompanying drop in the growth rate. If we assume that the temperatures at which 1/S extrapolates to zero define a virtual phase boundary in figure 17b, then new values of X^{α} may be used in equation 27 from which bD_B may be recalculated and plotted in figure 56. It is seen that the linearity of the curve is restored. A possible significance of this result may be seen by reference to the free energy curve in figure 7. If the reciprocal of spacing is proportional to the free energy available from the reaction, then it is seen that the available free energy from a metastable monotectoid reaction, ΔF_1, is less than that available from the ordinary precipitation reaction, $\Delta F_1 + \Delta F_2$. Hence

1/S has a smaller value than expected at low supersaturations. This phenomenon is discussed further in section 6.5.

(d) The activation energy calculated from the curves in figure 56 is 36.5 Kcal/gm. mole. This value is considerably higher than that found by Böhm, and must be due to the different spacing values obtained in the two experiments. One expects boundary diffusion activation energies to be from 0.45 to 0.65 of the volume diffusion activation energy for the same system. Neither boundary nor volume diffusion data is available for α copper indium alloys. Volume diffusion data is available for α Cu-Sn alloys which may be close to those for Cu-In since the copper-solute atom size differences are comparable and the constitution diagrams are somewhat similar. From Smithell's, the diffusion coefficient increases rapidly with tin content, especially at lower temperatures (168). This is reflected in the drop in the activation energy for volume diffusion, from 58 Kcal/gm. mole at 1% Sn to 35 Kcal/gm. mole at 5 at % Sn. The volume diffusion activation energy for self-diffusion in copper is 47 Kcal/gm. mole. On this basis we might expect the value for boundary diffusion to range from 16 to 47 Kcal/gm. mole, with a value 20-25 Kcal/gm. mole being most probable. The value for silver self-diffusion in figure 56 is 21 Kcal/gm. mole. Thus we may suspect that the value obtained from the application of Turnbull's equation is too high to describe a boundary diffusion process.

A possible explanation of this behaviour which allows us to lower the value of activation energy obtained from figure 56 and thus retain the boundary diffusion model is now given. The curves in figure 56 are independent of initial composition, as mentioned. Let us assume a strong increase with composition in the ordinary grain boundary diffusion coefficient at low temperatures, as shown in figure 57, as is the actual case

for Cu-Sn volume diffusion. Let us further assume that the phase boundary diffusion coefficient depends mainly on the composition of the depleted α phase, and so does not vary greatly with initial composition as is actually observed at each precipitation temperature. Then the apparently rapid increase with temperature of bD_B as shown in figure 56 could be due to the increase in bD_B with X^{α} as the latter increases with temperature as indicated by curve A in figure 57. If this composition variation were subtracted then a smaller slope in curve A would be obtained.

The other possible explanations of this value for the activation energy lie in the possibility that Turnbull's equation is not a good approximation, and that the precipitation process is not boundary diffusion controlled. These possibilities are best discussed as part of the following two sections.

6.3 Cahn's Model, and Estimates of the Interface Mobility

(a) Internal Consistency and the Calculation of Mobility

The results of Cahn's model, which assumes boundary mobility and boundary diffusivity control, were presented in figure 11, using the dimensionless parameter

$$\beta = - \frac{kM\sigma^2 V^2}{bD_B \Delta F_o} . \qquad (42)$$

The internal consistency of this model may be checked by determining β in two independent ways. From our experimental data we may estimate both Q and R (as defined in section 2.3b) and find β using fig. 11. The more reliable values of α-phase composition given in Table 13 allow us to estimate $Q = 0.87 \pm .02$. Therefore $\beta = 4.4 \times 10^{-3}$ ($\pm 1 \times 10^{-3}$).

We also have the relation

$$R = \frac{2\sigma V}{S\Delta F_o} .$$

For the 7.5 at % In alloy, at 400°C we have the following values:

$\sigma^{\alpha\delta}$ = 400 erg/cm^2 (discussed below),

V = 7.5 cm^3/mole,

ΔF_o = -2.3 x 10^9 erg/gm mole, (from eq. 33)

S = 0.314μ.

Therefore R = 0.078 and from fig. 11 β = 5.2 x 10^{-3}

The most uncertain quantities in the evaluation of R are $\sigma^{\alpha\delta}$ and ΔF_o. Values for grain boundary surface tensions are listed by Inman and Tipler (162). In the cellular precipitate in Cu-In alloys, the lamellae are frequently observed to be curved or branched. In fact the analysis of several electron diffraction photographs yielded no simple or consistent habit relationship. Thus we conclude that a rigid habit is not attained and hence the value for $\sigma^{\alpha\delta}$ need not be much lower than a typical grain boundary free energy for a copper alloy. A value of 400 erg/cm^2 was therefore chosen. The estimate of ΔF_o will be discussed later. It will be seen that the present method should be fairly reliable for moderate supersaturations.

The two estimates of β agree fairly well for Cu-In alloys. By way of contrast, Cahn noted a poor agreement in the case of Pb-Sn alloys. The value of β found from R was approximately the same as that found here, but the value found from Q was about 500 times higher, due to the relatively large supersaturation remaining in the α-phase after the cellular reaction.

Because the data for Cu-In consistently fits the reaction control model, the next important test is a comparison of the values of phase boundary mobility, M, found through Cahn's analysis and by independent methods. There are two methods of calculating M from Cahn's growth model, and these are also independent. One can use both eq. 41

$$M = \frac{v}{(P-R)\ \Delta F_o} \quad ,$$

and eq. 42 (repeated earlier). For the application of eq. 41 for the 7.5 at % In alloy, values of v are taken from fig. 45, ΔF_o from eq. 33 and (P-R) from fig. 11 for $\beta = 5 \times 10^{-3}$. One needs values of bD_B and k in order to apply eq. 42. If these quantities can be measured directly then eq. 41 is truly independent of eq. 42. However, we are forced to use Turnbull's equation 27 for bD_B, which is derived from the kinetic data of the precipitation reaction, and we can only assume a value for k. This value is unity. Nonetheless, we have calculated M by both methods and have plotted the results in fig. 58 for the range of temperature 330°C to 450°C. It is seen that fair agreement exists between the two sets of values.

Three reactions, which involve boundary mobility control without any accompanying boundary diffusion, have been chosen to yield values of mobility for comparison with those calculated from the discontinuous precipitation reaction. These are grain growth in a concentrated alloy, the massive transformation in alloys, and the crystallization of amorphous thin alloy films which are deposited in a vacuum. The method of calculation of the mobility from these reactions is outlined in the next three sections.

(b) Mobility Values from Grain Growth in Concentrated Alloys

The problem of grain boundary migration in concentrated alloys has not received as much study as that in very pure metals or dilute alloys. Lücke and Stüwe have considered the theoretical problem (194). The boundary mobility is defined in an identical manner to that used here. The effect of a solute which is attracted to a grain boundary is discussed.

The attraction results in a solute atmosphere about the boundary. This atmosphere is most pronounced at lower temperatures and evaporates into the lattice at high temperatures. When the boundary is subject to a driving pressure the atmosphere exerts a retarding pressure. For a low boundary velocity, the full atmosphere can maintain a similar velocity. At higher velocities the extent of the atmosphere diminishes, and exerts a weaker retardation force. That is, the boundary can break away from the atmosphere. The reason for this is that at high velocities insufficient time is available to maintain the clustering of the solute about the moving boundary by volume diffusion. Thus, at low velocities and low temperatures, the kinetics of boundary migration should be governed by the rate of solute diffusion and should show a high volume diffusion activation energy, while at high velocities and high temperature the kinetics are determined by the mobility alone, and the activation energy should be that appropriate to grain boundary diffusion.

Grain growth experiments can provide a good example of pure mobility control. The driving pressure is given by

$$\Delta P = \frac{2\sigma}{r} \quad , \tag{83}$$

where r is the radius of curvature of a boundary, which will be close to the average radius of a grain. Therefore

$$v = \frac{dr}{dt} = M2\sigma V_o \frac{1}{r} \tag{84}$$

Integrating

$$r^2 - r_o^2 = M't \quad , \tag{85}$$

where

$$M' = 4\sigma VM \quad . \tag{86}$$

Thus the measured values of M' enable us to find a value of mobility for comparison with that found by Cahn's analysis. This will be true so long

as the values obtained refer to the same velocity and temperature conditions, as discussed in the last paragraph. Immediately it can be seen that discontinuous precipitation involves much larger driving forces than does grain growth. The average radius of curvature in the first case is comparable with the spacing, but the pressure of this curvature (exerted to retard the interface advance) is only about 1/10 of the total driving force. Therefore the radius of curvature which would exert a driving force, equivalent to $(P-R)\ \Delta F_o$, is about

$$\frac{1}{12} \times 0.3\mu = \frac{1}{40}\ \mu,$$

whereas the typical grain size in grain growth experiments is about 10μ. Therefore cellular precipitation should be less affected by the retardation of an atmosphere than is grain growth, and if the latter reaction appears unaffected then the former certainly is. On the other hand it will be seen shortly that the temperature of discontinuous precipitation is usually around the lower limit of grain growth experiment temperatures so that the effect of an atmosphere would be increased for our reaction. Therefore, a possible explanation for the high value of diffusion activation energy found using Turnbull's equation may be the existence of an atmosphere at the advancing interface.

Feltham and Copley have measured the grain growth parameters in α-brass in the temperature range 475°C to 700°C and for zinc contents of 10% to 35% (171). (No work has been done with Cu-In alloys.) Eq. 85 was found to hold, which shows that long range or cumulative volume diffusion effects are not important. The following expression was found for M':

$$M' = K \exp(-H/RT)$$

or

$$M' = K_o \exp\left(-\frac{9\ H_\ell\ X_{zn}}{RT_s}\right) \exp\left(-\frac{H_o - 25.4\ X_{zn}}{RT}\right) \qquad (87)$$

where

K_o = 3 x 10^{-3} cm^2/sec,

H_o = 20.2 Kcal/gm-mole,

X_{zn} = mole fraction of zinc,

H_ℓ = 2.84 Kcal/gm-mole = latent heat of melting for copper,

T_s = 1200°K = solidus for a 30% Zn alloy.

The authors interpret this result as showing that atomistically the grain growth process is essentially equivalent to grain boundary diffusion, because of the low initial value of H_o, and because of the decrease of H with composition. We may stress that no effect of a boundary atmosphere is evident from these measurements. Finally, we note that Cahn's suggestion that the boundary mobility is determined by the lowest values of individual atomic mobility in the boundary while the boundary diffusivity is determined by the highest atomic mobility, is refuted by the results of these experiments.

To use this result for our work we compare phase diagrams and electron-per-atom ratios for Cu-Zn and Cu-In alloys, and assume that we may use the above results by letting 1 at % In be equivalent to 3 at % Zn. Hence we calculate H = 14.8 Kcal/gm-mole and K = 3 x 10^{-4}. From these quantities and eq. 86 and 87, we evaluate M, which is plotted in fig. 58. The values obtained are about 1000 times larger than estimated using Cahn's model.

(c) The Mobility Value from the Massive Transformation

The massive transformation was mentioned in section 1.3b. The mechanism of the growth of the new phase appears to range from the passage of an incoherent boundary to a martensite-like transformation. We are interested in the former only. No growth rates have been measured in the

Cu-Ga system because some massive product, the ζ_s phase, appears even on quenching from the temperature range where the parent phase is stable. Thus the growth rates are very high, and we estimate from micrographs in reference 156 that a minimum value is

$$v = 10^{-2} \text{ cm/sec.}$$

In order to calculate the mobility, $M = \frac{-v}{\Delta F}$, we also need ΔF. This cannot be large for the reaction is observed in Cu-Ga alloys at 600°C only 16°C below the temperature where the β phase is stable. Since the ζ_s-phase can only be stable with respect to β for some finite undercooling, we estimate a maximum value of $-\Delta F$ to be

$$-\Delta F \stackrel{\circ}{=} 20 \text{ cal/gm-mole}$$

$$\stackrel{\circ}{=} 10^{9} \text{ erg/gm-mole .}$$

Therefore a conservative estimate of the mobility at about 600°C is

$$M = 10^{-11} \ \frac{\text{cm-gm mole}}{\text{sec-erg}} \ .$$

This single estimate is plotted in fig. 58, and it is seen that it compares well with the value obtained for grain growth at the same temperature. We may conclude that the growth of one phase at the expense of another of the same composition is probably controlled by the same basic grain boundary diffusion mechanism as the grain growth process.

(d) The Mobility Value from the Crystallization of Amorphous Thin Alloy Films

Mader et al have prepared thin films of Cu-Ag, Cu-Co and Au-Co alloys by simultaneous evaporation of each metal of a given pair (191, 192). The substrate, amorphous, or crystalline, was maintained at ~80°K, which resulted in the deposition of a homogeneous and amorphous alloy film. On heating, two distinct changes occur. First there is crystallization to a homogeneous alloy. For equiatomic Cu-Ag alloys this process begins at

about 250°K and is fastest at 350°K, when heating at the rate of 40°K/hour. At these temperatures, Cu-Ag alloys should exist as two phases of fairly pure copper and silver. The segregation process actually begins at about 440°K and is complete at 500°K for the same heating rate.

It is the first process that is of interest here, for the atomic mobility associated with the crystallization of an amorphous alloy without long range diffusion should be comparable to that which governs the advance of an incoherent interface.

The calculation of a value for the mobility M from the available data for this reaction involves several plausible assumptions that have not been subject to experimental verification. The only kinetic data available is the electrical resistance of the alloy film as a function of temperature for a fixed rate of heating. No isothermal experiments have been performed. In addition, the parameters of the crystal growth process are unknown. We do not know the rate of formation or final dispersion of crystal nuclei.

The first assumption is that the final grain size is of the order of the film thickness, 10^{-5} cm, so that there is one spherical crystal nucleus in a volume, V_o, of 10^{-15} cm^2. Secondly, we assume that apart from its positive temperature coefficient the relative change in resistance is proportional to the relative volume of crystalline material in the amorphous matrix. We use the initial slower change of resistance for calculation, since at early times there is little likelihood of impingement between growing grains. We calculate the isothermal time rate of change of resistance as

$$\frac{d\rho}{dt} = \frac{d\rho}{dT}\frac{dT}{dt} \quad .$$

From reference 191 we estimate the rate of relative volume change at 250°K to be

$$\frac{1}{V_o}\frac{dV}{dt} = \frac{1}{\rho}\frac{d\rho}{dt} = 10^{-5}\ \text{sec}^{-1}\ .$$

Now

$$\frac{dV}{dt} = 8\pi r^2 \frac{dr}{dt} = 8\pi r^2 v\ ,$$

and at the early time we choose $r = 10^{-6}$ cm.

Therefore,

$$v = \frac{V_o}{8\pi r^2}\left(\frac{1}{\rho}\frac{d\rho}{dt}\right)$$

$$\cong \frac{10^{-15}\ 10^{-5}}{8\ \pi\ 10^{-12}}\ .$$

Finally, $v \cong 4 \times 10^{-10}$ cm/sec.

The driving force ΔF is calculated as

$$-\Delta F \cong \frac{H_\ell}{T_s}\ \Delta T\ ,$$

where H_ℓ = average latent heat of melting for silver and copper = 2750 cal/gm-mole, and T_s = temperature at which liquid alloy is in equilibrium with the homogeneous equiatomic alloy. Since copper and silver form a simple eutectic, at the eutectic temperature (~800°C), liquid is in equilibrium with the two solid phases, which are more stable than a homogeneous alloy. Therefore $T_s < 800$°C, and we choose $T_s = 750$°C = 1020°K.

Therefore,

$$\Delta T = T_s - T = 770\text{°K}.$$

and

$$\Delta F = 2080\ \text{cal/gm-mole}.$$

Finally,

$$M = \frac{4 \times 10^{-10}}{2080 \times 4.2 \times 10^{7}} = 4.5 \times 10^{-21}\ \frac{\text{cm}}{\text{sec}} - \frac{\text{gm-mole}}{\text{erg}}\ .$$

For comparison we plot this value in Fig. 58. Again excellent agreement is obtained between the reaction constant of this reaction and the value obtained by extrapolating the results of the grain growth experiments.

We may conclude from these three examples of purely mobility controlled processes that mobilities evaluated from discontinuous precipitation experiments using Cahn's theory are too low by about three orders of magnitude. Therefore, using the new values of M in a model which includes both mobility and diffusion terms, will result in virtual compliance with the local equilibrium assumption. As a final note of caution we emphasize that the above examples apply to alloys other than copper-indium. Grain growth and thin film crystallization experiments can and should be performed on copper-indium alloys.

6.4 Metastable Monotectoid, Local Equilibrium Model for Growth

The most useful relation resulting from this model is eq. 74,

$$vS^3 = \frac{48bD_B\sigma^{\alpha\beta}V(K-1)}{q(\frac{1}{2}-a)^2} \quad .$$

We now apply eq. 74 to the cellular precipitation process in full awareness that the curves in figure 14 may be but a poor approximation to the free energy relations for cellular precipitation in Cu-In alloys. vS^3 should be approximately proportional to bD_B, and so is plotted on a log scale as a function of reciprocal absolute temperature in figure 59. The graph is linear even in the high temperature region for the 7.51% alloy, unlike the curve for Turnbull's equation using the equilibrium solubility data. In addition vS^3 appears to be independent of initial composition, as was the case for bD_B in figure 56. From the slope of the curve we calculate a tentative value for the activation energy for diffusion,

$$\Delta H \cong 37 \pm 3 \text{ Kcal/gm-mole} .$$

We next attempt to improve the thermodynamic approximation by considering the variation with temperature of the quantities q and $(\frac{1}{2} - a)^2$. For the free energy curves depicted in figure 14, these quantities are constants, but for an actual alloy "q" should decrease and "a" increase with temperature, as mentioned in section 2.4d.

Thus

$$\frac{d \ln \nu S^3}{d(\frac{1}{T})} = \frac{d \ln bD_B}{d(\frac{1}{T})} - \frac{d \ln q}{d(\frac{1}{T})} - 2 \frac{d \ln (\frac{1}{2} - a)}{d(\frac{1}{T})}$$

or

$$\Delta H = \Delta H_D - \Delta H_q - 2\Delta H_a$$

and we must find ΔH_q and ΔH_a. From eq. 56 a

$$q = \frac{1}{2} \frac{\partial^2 f^\alpha}{\partial X^{\alpha 2}} .$$

Therefore,

$$q \cong \frac{1}{2} RT(e^{\frac{zU}{RT}} - 2zU)$$

from section 2.4d and reference 178.

Hence,

$$\Delta H_q \overset{\circ}{\cong} -zU = -2RT_o ,$$

where T_o is the maximum temperature of immiscibility in Cottrell's example (178). From the Cu-In phase diagram we estimate

$$T_o \overset{\circ}{\cong} 1000^\circ K, \text{ so that}$$

$$\Delta H_q \overset{\circ}{\cong} -4 \text{ Kcal/gm-mole}.$$

ΔH_a cannot be found in an analytically simple way. We shall interpret $(\frac{1}{2} - a)$ as $(X^{\alpha' o} - X_e^\alpha)$ (as recalled from fig. 14) and calculate the difference quotient rather than the derivative,

$$2\Delta H_a = -2R\ell n \left[\frac{X^{\alpha' o} - X_e^{\alpha}(T_1)}{X^{\alpha o} - X_e^{\alpha}(T_2)}\right] / \left(\frac{1}{T_1} - \frac{1}{T_2}\right) .$$

Taking $X^{\alpha' o} = 0075$, $T_1 = 723^{\circ}K$, $T_2 = 523^{\circ}K$, then $2\Delta H_a = -6.8$ Kcal/gm-mole. Therefore

$$\Delta H_D = \Delta H + \Delta H_q + 2\Delta H_a ,$$

$$= 26 \pm 3 \text{ Kcal/gm-mole.}$$

This is a more reasonable value for a boundary diffusion controlled process. Although the corrections ΔH_q, ΔH_a may not be numerically very accurate, they do have the proper sign. In addition these corrections do not seem so large as to make the initial approximation an unreasonable starting point. Finally, it is recalled from section 6.2 that another adjustment in ΔH_D can be made. This adjustment arises from the variation of bD_B with the final α-phase composition which in turn increases with temperature, as shown in figure 57.

Thus we see that the apparently high diffusion activation energy as determined from Turnbull's analysis can be improved using the present thermodynamic model, and that a log plot of vS^3 is linear over a wider temperature range than is bD_B calculated from Turnbull's model.

The discussion above is consistent with, but is not absolute proof of the metastable monotectoid, local equilibrium model. Further support comes from the electron micrographs of the advancing interface shown in fig. 54. These show that the curvature increases from the lamella center to the α-β interface, and that close to mechanical equilibrium obtains at the α' - α - β juncture.

In section 6.2 the suggestion was made that the extrapolation of 1/S to a value zero at a temperature less than the solvus also indicates the existence of the metastable monotectoid reaction. This possibility is

discussed further in the following section.

6.5 The Lamellar Spacing and the Available Free Energy of Precipitation

The reciprocal spacing curves plotted in figure 5 indicate that the 1/S values extrapolate to zero at temperatures below the solvus in alloy systems other than Cu-In. The values of

$$\Delta T = T(\tfrac{1}{S} \to 0) - T \text{ (solvus)}$$

are listed in table 14. (The data for Pb-Sn were obtained by first plotting 1/S versus $X^{\alpha'o}$ at constant temperature, and then using the phase boundary determined by Cahn and Treaftis (10)). It is seen that all alloys except Fe-Ni-Ti behave in a similar manner.

Table XIV - $T(\frac{1}{S} \to 0)$ - T(solvus) for Various Alloys

Alloy	Composition	ΔT ($^{\circ}C$)
Cu Cd	1.8 wt % Cd	+ 5 ± 10 (2 points only)
Cu Cd	2.9 wt % Cd	- 33 ± 5
Cu Cd	3.8 wt % Cd	- 25 ± 5
Pb - Sn	11.2 at % Sn	- 4 ± 3
Pb - Sn	14.7 at % Sn	- 9 ± 3
Pb - Sn	17.0 at % Sn	- 11 ± 3
Fe-30 Ni-6 Ti		0 ± 2
Cu-In	5.13	-22 ± 12
	7.51	-38 ± 8
	10.07	-49 ± 12

There are two reasons to suspect that the reciprocal spacing is proportional to the available free energy from the discontinuous pre-

cipitation reaction. First such a proportionality is found experimentally for the eutectoid reactions in Fe-C, Cu-Be, and Cu-In. In the case of these alloys a plot of 1/S versus T is linear and an extrapolation does yield the eutectoid temperature, T_e. (Appropriate data may be found in references 42, 151, and 153.) Since

$$\Delta F_o \doteq \frac{H}{T_e}(T - T_e) ,$$

where H is the latent heat of the eutectoid reaction, the linear dependence of 1/S on temperature proves the required proportionality. Second, the results of the theory in sections 2.4d and 25 show to a good approximation that all optimization principles thus far proposed will yield a proportionality between 1/S and ΔF_o, due to the factor $(1 - \frac{2\sigma^{\alpha\beta}v}{(A'-A)S})$ in eq. 72. The proportionality constant was taken as K. Therefore we seek the significance of the 1/S versus T curves in terms of the available free energy according to various thermodynamic models, especially at low supersaturations.

The simplest model is that depicted in figure 10, i.e., not a monotectoid. The free energy change of reaction is given by eq. 33:

$$\Delta F_o = RT(X^{\alpha'} \ln \frac{X^{\alpha}}{X^{\alpha'}} + (1 - X^{\alpha'}) \ln \frac{1 - X^{\alpha}}{1 - X^{\alpha'}})$$

For small undercoolings below T', $(X = X^{\alpha'}$ at $T = T')$ we may use the Taylor series,

$$\Delta F_o(T) = \frac{\partial \Delta F_o}{\partial T}\Delta T + \frac{\partial^2 \Delta F_o}{\partial T^2}\frac{\Delta T^2}{2} + \frac{\partial^3 \Delta F_o}{\partial T^3}\frac{\Delta T^3}{6} + \ldots , \qquad (88)$$

where the derivatives are evaluated at $T = T'$.

Thus at $T = T'$ $\quad \frac{\partial \Delta F_o}{\partial T} = 0$

$$\frac{\partial^2 \Delta F_o}{\partial T^2} = -\frac{RT}{X^{\alpha'}(1 - X^{\alpha'})}\left(\frac{dX^{\alpha}}{dT}\right)^2 ,$$

and

$$\frac{\partial^3 \Delta F_o}{\partial T^3} = -\frac{3R}{X^{\alpha'}(1-X^{\alpha'})}\left(\frac{dX^{\alpha}}{dT}\right)^2 - \frac{3\,RT}{X^{\alpha'}(1-X^{\alpha'})}\frac{dX^{\alpha}}{dT}\frac{d^2X^{\alpha}}{dT^2}$$

$$+ 2RT\left[\frac{(1-X^{\alpha'})^2 - X^{\alpha'2}}{X^{\alpha'2}(1-X^{\alpha'})^2}\right]\left(\frac{dX^{\alpha}}{dT}\right)^3$$

The derivatives $\frac{dX^{\alpha'}}{dT}$, etc. are determined from the shape of the α phase boundary. For the region 400°C to 500°C the Cu-In α-phase boundary is given by

$$X^{\alpha'} - X^{\alpha} = p(T' - T) - m\,(T' - T)^2$$

where

$$X^{\alpha'} = 0.075\ ,$$

$$T' = 488^{\circ}C\ ,$$

$$p = 7.97 \times 10^{-4}$$

$$m = 2.42 \times 10^{-6}\ .$$

Therefore, at $T = T'$,

$$\frac{dX^{\alpha}}{dT} = p$$

and

$$\frac{d^2X^{\alpha}}{dT^2} = 2\,m\ .$$

Finally,

$$\Delta F_o(T) = -6.9 \times 10^{-3}(T'-T)^2 - 4.0 \times 10^{-6}(T'-T)^3\ \frac{cal}{mole} \qquad (89)$$

It can be shown that the second term is small compared to the first even at 400°C so that a parabolic dependence of ΔF_o on undercooling remains. Thus the apparent linear extrapolation of 1/S to zero at temperatures below T' may merely reflect this parabolic variation of ΔF_o. To test this statement we plot in figure 60 1/S versus ΔF_o as calculated by eq. 89 for the 7.51 % In alloy. At low supersaturations (small ΔF_o) the spacing is still

larger than expected from the proportionality between 1/S and ΔF_o at higher supersaturations.

We next consider the result of a departure from Henry's law for the solute. In this case eq. 33 does not apply so that we must write for the free energy change on precipitation

$$\Delta F = RT[X^{\alpha'} \ln \frac{X^{\alpha}(1+\varepsilon X^{\alpha})}{X^{\alpha'}(1+\varepsilon X^{\alpha'})} + (1 - X^{\alpha'}) \ln \frac{(1-X^{\alpha})(1-\frac{1}{2}\varepsilon X^{\alpha 2})}{(1-X^{\alpha'})(1-\frac{1}{2}\varepsilon X^{\alpha' 2})}] \quad (90)$$

since

$$\mu_B^{\alpha} \cong \mu_B^{\alpha o} + RT \ln \eta X_B^{\alpha} (1 + \varepsilon X_B^{\alpha}) \quad (91)$$

$$\mu_A^{\alpha} \cong \mu_A^{\alpha o} + RT \ln X_A^{\alpha} (1 - \frac{1}{2} \varepsilon X_B^{\alpha 2}) \quad (92)$$

and

$$X_A + X_B = 1 .$$

These equations show the departure from Henry's and Raoult's laws. Eq. 88 is rather cumbersome to apply, so we shall evaluate the first approximation to ΔF at $X^{\alpha} = X^{\alpha'} + \Delta X$. We use X' for $X^{\alpha'}$ and X for X^{α}. From eq. 90, 91 and 92

$$\Delta F = RT[X' \ln \frac{(X'+\Delta X)(1+\varepsilon(X'+\Delta X))}{X'(1-\varepsilon X')}$$

$$+ (1-X') \ln \frac{(1-X-\Delta X)(1-\frac{1}{2}\varepsilon(X'+\Delta X)^2)}{(1-X')(1-\frac{1}{2}\varepsilon X'^2)}] \quad (93)$$

$$= RT [X' \ln(1+\frac{\Delta X}{X'}) + X' \ln(1 + \frac{\varepsilon \Delta X}{1+\varepsilon X'})$$

$$+ (1-X') \ln(1-\frac{\Delta X}{1-X'}) + (1-X') \ln(1-\frac{\varepsilon X' \Delta X - \frac{1}{2}\varepsilon \Delta X^2}{1-\frac{1}{2}\varepsilon X'^2})]$$

$$\cong RT[\frac{\Delta X \varepsilon X'}{1+\varepsilon X'} - (1-X') \frac{\varepsilon \Delta X (X' - \frac{1}{2}\Delta X)}{1-\frac{1}{2}\varepsilon X'^2}] .$$

Finally,

$$\Delta F \doteq -RT\,\varepsilon\Delta X\left[\frac{X'^2\left(1-\varepsilon-\frac{X'}{2}+\varepsilon X'\right)+\frac{\Delta X}{2}\left(1-X'+\varepsilon X'-\varepsilon X'^2\right)}{1+\varepsilon X'-\frac{\varepsilon X'^2}{2}-\frac{\varepsilon X'^3}{2}}\right] \qquad (94)$$

Thus a term in ΔX (or ΔT) does exist for a thermodynamic model which is more realistic than the previous one. To a first approximation, the ΔF term found in eq. 94 may be added to those of eq. 89 so that the points on Figure 60 should be shifted to higher $|\Delta F|$ values. This shift is relatively more pronounced at lower supersaturations so that the departure of 1/S from proportionality with respect to ΔF_o as calculated in this section is also more pronounced. This departure is in the direction that favours a metastable monotectoid reaction rather than a simple precipitation reaction. That is, one cannot assume that both the above normal thermodynamic model holds, and that the energy stored in the α-δ interfaces is a constant fraction of the available free energy for all supersaturations. We have chosen to retain the latter assumption because of the two reasons given previously. Finally, although these results do support a metastable monotectoid theory, we must bear in mind that the spacing measurements do become more difficult at low supersaturations since the frequency of nodule formation is lower, and that few other workers have concentrated efforts in this area to provide reliable corroborating data.

Table 14 and figure 5 show that the results for Fe-30 Ni-6Ti differ from those for other alloys. Claiming to use the Henry's law approximation, eq. 33, for calculating ΔF_o, Speich obtains the result (15)

$$\Delta F_o = 0.1\,(T - T') \text{ cal/mole} .$$

This expression disagrees in form with eq. 89, in which no term linear in $(T - T')$ is present. Because of this disagreement, it is difficult to comment further on the spacing data for this alloy.

The metastable monotectoid postulate as a general principle appears to run into serious difficulty for the Au-Ni system.* As mentioned in section 3.2d, both the growth rates and the free energy of formation of supersaturated Au-Ni alloys have been measured (79, 95). At 775°C the free energy of formation curve appears to have a single concave downward section from 50 to 90 at % Ni, indicating a simple miscibility gap and no metastable monotectoid. In addition the growth rates of a 69 at % Ni alloy are measured up to 797°C. This information cannot be taken as a positive proof against the monotectoid model because Sellars and Maak claim an accuracy of $\pm$ 10 cal/gm mole in the free energy data, and the maximum free energy difference between the unstable homogeneous alloy and the stable two phase alloy is also about 10 cal/gm mole at 775°C. Therefore it is still possible that an intermediate concave upwards section exists in the free energy-composition curve, as required for the metastable monotectoid reaction.

Although it has not been possible to accurately evaluate the free energy released on precipitation there is still some value in estimating the fraction of this free energy that is stored as interfacial energy, denoted by 1/K in eq. 73. From figure 60 at higher ΔF_o we obtain

$$\frac{1}{2\sigma VK} = 1.6 \times 10^{-5} \text{ cm}^{-1} \text{ erg}^{-1} \text{-gm mole.}$$

Therefore

$$\frac{1}{K} = 0.076,$$

if we use $V = 7.5$ cm^3/gm mole, $\sigma = 400$ erg/cm^2. In terms of the minimum possible spacing S_c, figure 15, we have $S/S_c = 10.4$.

---

* Prof. M. Hillert, private communication to Prof. J. S. Kirkaldy.

There are two factors which suggest that this ratio may actually be lower than 10.4. First, the solute content of the α-phase does not have its equilibrium value. This was proved experimentally and may be understood on the basis of either Cahn's model ($Q < 1$), or the metastable monotectoid model, since the α-phase composition determined by local equilibrium at each point along the advancing interface will be greater than the composition in equilibrium with δ at the same temperature. Hence the free energy available for conversion to $\alpha - \delta$ surface is reduced. Secondly, the total free energy available from a metastable monotectoid reaction may be substantially less than that calculated from eq. 33 as shown in Fig. 7.

The observed spacing may also be said to be at most five and seven times the spacing predicted from the assumptions of maximum rate of entropy production and maximum growth rate, respectively. These high values have been interpreted as evidence that either the local equilibrium model presented in section 2.4 does not apply or that the correct optimization procedure has not been discovered. Another interpretation concerns the volume diffusion in the α' phase that must accompany a local equilibrium model. In section 2.4a (using eq. 17) we showed that, D_v/v, the typical volume diffusion distance under the conditions of growth, is from 5A to 20A. If this distance is not sufficient to establish the required composition in the α'-phase then a decrease of v allows the diffusion distance to increase. In its turn the spacing can then increase taking advantage of the greater time available for boundary diffusion. As yet we have no evidence to enable us to choose between these three explanations.

6.6 Suggestions for Future Study

Discontinuous precipitation is a complex reaction, whose analysis depends on the knowledge of several quantities other than such growth parameters as v, S, X^{α}. If these quantities can be measured independently, then progress will be made in the evaluation of the various models. The following suggestions are directed toward this task.

(a) The local equilibrium and interface diffusion model can be tested independently of the metastable monotectoid assumption with a eutectoid reaction involving substitutional solid solutions. A system should be chosen which does not undergo simultaneous reaction by other mechanisms, as do β Cu-Al, Cu-Ga, and Cu-In alloys.

(b) Although it is impossible to obtain independent data for interface diffusion between the phases of interest in a cellular precipitation reaction, boundary diffusion data in the homogeneous alloys of the major phase should still be useful, such as in α Cu-In.

(c) For similar reasons, independent experiments should be performed to evaluate the mobility of grain boundaries in both α and δ Cu-In alloys. Both grain growth measurements and experiments to measure the rate of crystallization of amorphous alloys should be useful, since these two experiments are performed at temperatures which bracket the temperatures of discontinuous precipitation. If possible the crystallization process should be observed directly at constant temperature so that a soundly based growth model can be formulated.

(d) It is recalled that the first discontinuous precipitate in Fe-30Ni - 6Ti alloys was characterized by a rigid α - β habit, resulting in a relatively wide variation of spacing within a cell, and no branching of the lamellae. If this coherency results in difficulty in attaining

the proper spacing when the temperature of reaction is varied then a way has been found to constrain the system to a spacing other than that given by the unknown optimization principle. By beginning the reaction at a set of temperatures (to obtain a set of spacings) and then varying the temperature, curves of the type represented by figure 15 may be generated and the diffusion model tested in a direct way. Unfortunately the observed spacings are so much greater than S_c that figure 15 predicts the variation of v with S will be small.

(e) The difficulty in nucleating cells in Cu-In alloys at low supersaturations may be overcome by the following method, which makes use of the fact that the lamellae do branch easily in this system. The precipitation is begun at a relatively low temperature to encourage profuse coverage of the grain boundaries with cells. Then the temperature is slowly raised to the temperature of interest so that the lamellae may continuously branch to maintain the required spacing. In this way better data may be obtained in the low supersaturation region.

(f) Experiments should be devised that enable one to measure the growth rate corresponding to a known spacing and set of crystallographic parameters (e.g. α - δ lamellar orientation). In this study the value of the kinetic parameters measured depended on the statistical methods which extracted the smallest spacing and largest growth rate.

6.7 Summary and Conclusions

a. Precipitation Morphology from α Cu-In Alloys

Supersaturated α phase copper indium alloys were found to decompose by both a continuous and discontinuous mode. In addition a fine precipitate, called δ', was observed to form in 10 at % In alloys.

The general precipitate does not interfere with the cellular reaction in alloys with a lower indium content; and for the highest In alloys no interference is observed during moderate precipitation times. The growth rate and lamellar spacing of the discontinuous precipitate has been measured, as well as the average α -phase composition for some heat treatments. It was found that for a given initial composition the reciprocal of spacing extrapolated to the value zero at a temperature below the solvus. Transmission electron micrographs have been obtained of the advancing interface region.

b. Evaluation of Various Theories

An evaluation of the kinetic data showed that Turnbull's interface diffusion model can account for the growth rate. The activation energy calculated for the apparent boundary diffusivity is 36.5 Kcal/gm mole as opposed to 21 Kcal/gm mole found from Böhm's data. Our apparently high value may be due to the variation of the α-phase composition with the temperature of precipitation.

The large values of spacing support Cahn's model of boundary diffusion and reaction control. However the value of boundary mobility required for quantitative agreement is about 1000 times smaller than that calculated from purely mobility controlled reactions in other copper alloys.

Kirkaldy's model, which assumes boundary diffusion and local equilibrium at the advancing interface in a metastable monotectoid reaction, was pursued to yield a kinetic equation relating v and S.

The problem of determining the stable steady state from all the possibilities that satisfy the diffusion model equations was considered but no conclusion was reached. The observed interlamellar spacings are

about six times greater than those calculated to yield the largest growth rate or the largest rate of entropy production on the basis of this model. On the other hand the phenomenon of the accelerated increase in spacing at low supersaturations indicates that less free energy is available in this transformation than is expected from a simple precipitation reaction. This observation is consistent with the metastable monotectoid reaction assumption. Furthermore the general profile of the advancing interface is consistent with a local equilibrium assumption which, for the discontinuous $\alpha' \rightarrow \alpha + \beta$ reaction, is only possible with a metastable monotectoid configuration.

The v and S data fit the kinetic equation derived for the symmetric eutectoid reaction in which local equilibrium and boundary diffusion are assumed. Although the translation to the unsymmetric monotectoid is difficult, the activation energy for diffusion, 26 ± 3 Kcal/gm mole, is more plausible than that found from Turnbull's equation, and can be made closer to the expected lower value using the same argument concerning the temperature variation of the α-phase composition as used for this equation. We may consider Turnbull's equation an expedient and useful approximation to the one derived in this work.

Thus there is some indirect evidence for both the reaction control and local equilibrium model. At this stage we favour the metastable monotectoid model although there is no unequivocal proof for it. It is our opinion that the problem of the choice of mechanism for discontinuous precipitation cannot be solved until the problem of the stability criterion for lamellar growth reactions is solved.

APPENDIX A

DISSOLUTION OF THE DISCONTINUOUS PRECIPITATE IN COPPER - INDIUM ALLOYS

In Chapter 1, we reviewed the morphology and kinetics of the discontinuous dissolution in Cu-Cd and Pb-Sn alloys (11, 145). In this section we briefly describe the dissolution behaviour of Cu-In alloys. 7.5 at % In alloys were first allowed to precipitate at 330°C for ten hours. The following treatments were then given:

Temperature	Time
450°C	26 hr.
461°C	12 hr.
470°C	24 hr.

The relevant microstructures are shown in figures 61, 62 and 29. Figure 61 shows that the lamellar structure easily spheroidizes, perhaps due to the lack of a strict α-δ orientation relationship. Some of the δ is probably dissolved in this process so that dissolution in Cu-In cannot be completely discontinuous. The formerly advancing interface is outlined by relatively large δ particles. The adjacent region of the matrix seems to have a lower density of δ particles than areas remote from the interface, so that the cells may have retreated during the growth of the larger particles. The density of general precipitate is much higher under the conditions of this two temperature precipitation process than after a single heating at 450°C for the same time, perhaps due to the more copious nucleation at the lower temperature. Thus as the discontinuous precipitate

dissolves on reheating to 450°C, continuous precipitation proceeds at a faster rate.

At 460°C, the continuous precipitate is less dense, the spheroidization still important, and the larger δ particles now appear to take a position behind the interface.

After a treatment at 470°C for twenty-four hours, the cells have disappeared completely, leaving a few δ particles. That dissolution has proceeded partly by the retreat of the nodule interface is shown by the appearance of small twins which have the same orientation as some of the large grain growth twins in some of the regions formerly occupied by cells. In this case the α phase has the orientation of the original grains (or their twins), and not the orientation of neighbouring grains as does the α phase in a cell.

We may conclude that dissolution below the solvus temperature for the initial compositions is characterized by spheroidization, and continuous dissolution as well as the discontinuous mode. The kinetics of the last process should then depend on the changing geometry and composition within the nodule, and so may be difficult to interpret. No study was made of the dissolution behaviour above the solvus temperature.

APPENDIX B

THE USE OF MOIRÉ PATTERNS IN THE STUDY OF FINE SCALE COMPOSITION VARIATIONS

Moiré patterns have been observed in electron microscopy when two lattices are superposed (198, 199). A simple explanation of this phenomenon comes from the analogy to microscopic light optics. When two almost identical grids are superposed a Moiré pattern is observed. Sets of atomic planes almost parallel to the electron beam are analogous to the set of lines in a grid. Two simple types of pattern exist, that for which the grids are parallel to each other, but have different spacing, and that for which the grids have the same spacing, but are rotated with respect to one another.

Moiré fringes arise from double diffraction in electron microscopy. A bright field image may be formed if the direct beam is combined with a beam so diffracted by each lattice in turn that it enters the objective aperture. The fringe spacing is given by the expression from light optics to a first approximation. For the parallel case the spacing in

$$u = \frac{d_1 d_2}{d_1 - d_2} \qquad \text{(A 1)}$$

where d_1, d_2 are the spacings of the relevant atomic planes. From the dynamical theory of electron diffraction Hashimoto et al have shown that the fringe spacing also depends on the thickness of the foils and the deviation from the Bragg angle (147). (For parallel lattices, the crystals cannot both be at the Bragg condition.) A 10% spacing variation

can result from these causes.

If the pair of parallel lattices is formed by the epitaxial growth of one crystal on an existing thin foil, then a second source of error in eq. A1 is present. The two lattices can be continuous if they exist in a state of plane strain at the interface or if an array of dislocations is present at the interface to accommodate the misfit. Van der Merwe has shown theoretically that all of the elastic strain is not relieved by a dislocation array (148).

Nonetheless eq. A1 shows that the fringe spacing u can be a sensitive function of one of the lattice spacings, d_1, say. Since the lattice parameter varies strongly with composition in Cu-In alloys then we have the possibility of determining composition variation on a fine scale. The variation of u with composition is given by

$$\frac{\delta u}{\delta X} = - \frac{u}{d_1 - d_2} (h^2 + K^2 + \ell^2)^{-1/2} \frac{\delta a_1}{\delta X}$$

where $d_1 = a_1 (h_1^2 + K_1^2 + \ell_1^2)^{-1/2}$, is the variable spacing. The results of some calculations are summarized below, for the average composition X = 2 at % In, and the (200) planes.

Second Foil	d_2	u	$\delta u / \delta X$
Cu	1.804	320A	160 A°/%
Ni	1.758	60A	5 A°/%

Embury and Duff have shown that copper may be deposited epitaxially on thinned copper indium alloys using a cyanide copper plating solution and a low current density, 0.5 ma/cm^2 (146). High current densities result in the normal polycrystalline deposit. Moiré fringes appeared with thinner deposits and a dislocation network with thicker deposits

(longer times at the same current density). The authors' main interest is the initiation of the discontinuous precipitate (private communication).

The ventilation in the specimen preparation area in our laboratories did not seem adequate for the use of cyanide solutions, and so other solutions were tried. Sulphate copper plating solutions resulted in an etched and jagged foil, probably due to the action of the acid during the time between electrodeposition and rinsing. A nickel plating solution (less acidic) was tried and found successful. This solution was prepared from a recipe received from H. Deem:

$Ni\ C\ell_2$ - 7 oz/gallon

$Ni\ SO_4\ (H_2O)_5$ - to make total metal content 10 oz/gal

Boric acid - 5 oz/gal

Dreft - a few drops from a solution of 1 tsp/gal

100 gm/gal of activated charcoal are added, the solution heated to 80°C and left to cool 12 hours. After filtration the solution was ready for use. The Ph should be between 5.4 and 5.6.

Samples were thinned in the usual manner, rinsed and immediately transferred to the electroplating solution in which a copper coupon of 1 cm^2 area was being plated at a preset current level of 1.5 ma. After one minute of plating the specimen was rinsed and cut for electron microscopy. Figures 63 a and b show the appearance of the still untransformed area of a 7.5 % In alloy aged ten hours at 330°C. The fringes of Figure 63a are seen to be fairly regular over wide areas, but less so than are those arising from epitaxial deposition from the vapour at higher temperatures (198). The spacing is about 100A, about twice the largest expected from eq. A1. This shows the effect of the coherency strain which decreases

the difference between the lattice parameters of two materials. One would also expect a change in $\frac{\delta a}{\delta X}$ to arise from this strain. Figure 63b shows what may be a dislocation network at the interface between the two layers. A different area of the same specimen is photographed. It is not known to what extent the appearance of dislocations depends on either a variation in deposition rate with surface orientation, or on the variation of the diffraction conditions with orientation.

The study was not extended to include thinned and plated nodules, and so the variation of fringe spacing across the lamellae was not investigated. Previous work indicates that cells do not thin uniformly, i.e. the δ phase is polished at a slower rate than the α phase and the thickness of α phase appears to vary across the lamellae. Consequently one expects the fringe spacing to vary both for this reason and because of any composition variation. Nevertheless, this method appears to be a promising technique for investigating fine scale composition variations in cellular precipitates.

BIBLIOGRAPHY

1. Jones, F.W., Leech, P. , Sykes, C. , Roy. Soc. Lond., Proc., 181, 154 (1942).
2. Forsyth, P. J. E., Metcalfe, G. J., King, R., Chalmers, B., Nature 158, 875 (1946).
3. Margolin, H., Hibbard, W. R. Jr., Trans. AIME, 191, 174 (1951).
4. Gruhl, W., Ammann, D., Acta Met., 3, 347 (1955).
5. DeSorbo, W., Turnbull, D., Acta Met., 4, 495 (1956).
6. Gruhl, W., Kramer, H., Metall., 12, 707, (1958).
7. Korchynsky, M. K., Fountain, R. W., Trans. AIME, 215, 1033, (1959).
8. Fountain, R. W., Forgeng, W. O., Trans. AIME, 215, 998, (1959).
9. Hagel, W. C., Beatie, Jr. H. J., Special Report 64 of the Iron and Steel Institute, (1959).
10. Cahn, J. W., Treaftis, H. N., Trans. AIME, 218, 376 (1960).
11. Sulonen, M. S., Acta Met., 8, 669, (1960).
12. Haynes, F. G., Smart, R. F., J. Inst. Met., 90, 189, (1962) also J. Inst. Met., 91, 153 (1962).
13. Böhm, H. Z.Metallkde, 54, 142 (1963).
14. Piearcey, B. J., Jackson, R., Argent, B. B., J. Inst. Met., 91, 257, (1963).
15. Speich, G. R., Trans AIME, 227, 754 (1963).
16. Hirschhorn, J. S., Gregg, R. A., Acta Met., 12, 120 (1964).
17. Sulonen, M. S., Acta Met., 12, 748, (1964).
19. Howard, R. T., Cohen, M., Trans AIME, 172, 413, (1947)
20. Shewmon, P. G., Diffusion in Solids, McGraw-Hill, (1963), p. 172.

21. Kirkaldy, J. S., Decomposition of Austenite by Diffusional Processes, Interscience, (1962), p. 39.

22. Cahn, J. W., Acta. Met., 7, 18, (1959).

23. Hillert, M., Jernkont Ann., 141, 757, (1957).

25. Turnbull, D., Acta Met., 3, 55, (1955).

26. Zener, C., Trans AIME, 167, 550, (1946).

27. Böhm, H., Z. Metallkde, 50, 87, (1959).

28. Turnbull, D., Treaftis, H. N., Trans AIME, 212, 33, (1958).

29. Turnbull, D., Treaftis, H. N., Acta Met., 3, 43, (1955).

30. Nystrom, J., Ark. Fys., 1, 359,(1949).

31. Smith, C. S., Trans. ASM, 45, 533, (1953).

32. Geisler, A. H., Metal Interfaces, ASM, p. 282 (1951).

33. Hardy, H. K., J. Inst. Met., 75, 707, (1948-9).

34. Tiedema, T. J., Burgers, W. G., Appl. Sci. Res., 4A, 243, (1954).

36. Geisler, A. H., Phase Transformations in Solids, Wiley p. 432, (1951).

37. Newkirk, J. B., Precipitation from Solid Solution, ASM, (1959), p. 22, 78.

38. Böhm, H., Z. Metallkde, 52, 518, (1961).

39. Böhm, H., Z. Metallkde, 52, 564, (1961).

40. Cahn, J. W., Acta Met., 4, 449, (1956).

41. Cahn, J. W., Acta Met., 4, 217, (1956).

42. Cahn, J. W., Hagel, W. C., Decomposition of Austenite by Diffusional Processes, Interscience, (1962), p. 132.

43. Hirschhorn, J. S., Gregg, R. A., J. Less Common Metals, 6, 333, (1964).

44. Bohm, H., Z. Metallkde, 52, 512, (1961).

59. Smith, C. S., Trans. ASM, 45, 555, (1953).

63. Koster, W., Donnöhl, W., Z. Metallkde, 28, 248, (1936).

64. Gerlach, W., Z. Metallkde, 29, 102, (1937).

65. Koster, W., Schneider, A., Z. Metallkde, 29, 103, (1937).

69. Borisov, V. T., Sov. Phys., Dokl. 8, 499, (1963).

70. Borisov, V. T., Sov. Phys., Dokl. 7, 50, (1962).

72. Sulonen, M. S., Acta Polytech. Scand; Ch 28, 1, (1964).

73. Kelly, A., Nicholson, R. B., Prog. in Mat. Sci., 10, 154, (1963).

75. Geisler, A. H., Newkirk, J. B., Trans AIME, 180, 101, (1949).

76. Borelius, G., Trans AIME, 191, 477, (1951).

77. Tufton, P.J., Ph. D. Thesis, U. of Cambridge, 1963.

79. Underwood, E.E., Ph. D. Thesis, M.I.T., 1954.

80. Pearson, W. B., Handbook of Lattice Spacings and Structures of Metals and Alloys, Pergammon, (1958), p. 580.

91. Weinberg, F., Prog. in Met. Phys. 8, 105 (1959).

94. Smith, C. S., Met. Reviews, 9, 1, 1964.

95. Sellar, C. M., Maak, F., Final Rept. to Air Force Office Of Sci. Res., Contr. No. AF 18(600) - 1572, (1962).

96. Phillips, V. A., Trans. AIME, 230, 967, (1964).

98. Johnson, A. A., Barton, P. W., Hughes, E. J., J. Metals, 16, 767, (1964).

102. Thomas, G., Transmission Electron Microscopy of Metals, Wiley, (1962), p. 153.

103. Tomlinson, H. M., Phil. Mag. 3, 867, (1958).

104. Swann, P. R., Nutting, J., J. Inst. Met. 88, 478, (1960).

106. Owen, E. A., O'Donnell Roberts, E. A., J. Inst. Met., 81, 479, (1952-3).

109. Tiedema, T.J., Bowman, J., Burgers, W.G., Acta Met. 5, 310, (1957).

117. Jackson, K. A., Chadwick, G. A., Klugert, A., Trans. AIME, 230, 1547, (1964).

122. Index, X-ray Powder Data File, 1960, 2-1178.

123. Moore, D. A., White, M., West, D.R.F., Nature, 185, 454, (1960).

124. Corderoy, D.J.H., Honeycombe, R.W.K., J. Inst. Met., 92, 65, (1963-4).

125. Embury, J. D., Nicholson, R. B., Acta Met., 13, 403, (1965).

128. Tiller, W. A., J. App. Phys. 34, 3615, (1963).

131. Menter, J. W., Adv. in Phys., 7, 299,(1958).

132. Hardy, H. K., Heal, T. J., Prog. in Met. Phys., 5, 143,(1954).

133. Nicholson, R. B., Electron Microscopy and Strength of Crystals, Interscience, (1963), Ch. 18, p. 861.

135. Thomas, G., Electron Microscopy and Strength of Crystals, (1963), Ch. 17, p. 836.

136. Smith, C. S., Trans. AIME, 175, 15, (1948).

137. Guy, A. G., Barrett, C. S., Mehl, R. F., Trans. AIME, 175, 216 (1948).

138. Mack, D. J., Trans. AIME, 175, 240, (1948).

139. Liu, C. T., Gurland, J., Trans. ASM, 58, 66, 1965.

140. Reynolds, J., Wisman, W. A., Hume-Rothery, W., J. Inst. Met., 80, 637, (1951-2).

143. Sulonen, M., Z. Metallkde, 55, 549, (1964).

144. Sulonen, M., Ann. Acad. Sci. Fenn. A, VI, 1, (1957).

145. Sulonen, M., 4th International Symposium on Reactivity of Solids, Amsterdam, (1960) p. 257.

146. Embury, J. D., Duff, W. R., U. S. Steel Corp. Res. Report, PR 289.

147. Hashimoto, H., Nannami, M., Maihi, T., Phil. Trans. Roy. Soc., 253A, 490, (1961).

148. Van der Merwe, J. H., J. App. Phys., 34, 123,(1963).

149. Massalski, T. B., Met. Reviews, 3, 45, (1958).

151. Spencer, C. W., Mack, D. J., J. Inst. Met., 82, 81, (1953-4).

152. Spencer, C. W., Mack, D. J., Decomposition of Austenite by Diffusional Processes, Interscience, (1962), p. 549.

153. Brelt, J. S., Kehl, G. L., Jaraiz, E., Trans AIME, 218, 753, (1960).

154. Spencer, C. W., Mack, D. J., J. Inst. Met., 84, 461, (1955-6).

155. Garwood, R. D., Hopkins, A. D., J. Inst. Met., 81, 407, (1952-3).

156. Massalski, T. B., Acta Met., 6, 243, 1958.

157. Murphy, W. K., Oriani, R. A., Acta Met., 6, 556,(1958).

161. Westbrook, J. H., Met. Reviews, 9, 415, (1964).

162. Inman,M.C., Tipler, H.R., Met. Reviews, 8, 105, (1963).

163. Jones, R. O., Owen, E. A., J. Inst. Met., 82, 445, (1954).

164. Shewmon, P. G., Trans. AIME, 233, 736, (1965).

165. Fillnow, R., Mack, D. J., Trans. AIME, 188, 1229, (1950).

168. Smithells, C. J., Metals Reference Book, Vol. II, Butterworths, (1962), p. 583.

169. Hirone, T., Kunitomi, N., Sakamoto, M., Yamaki, H., J. Phys. Soc., Japan, 131, 838, (1958).

171. Feltham, P., Copley, G. J., Acta Met., 6, 539, (1958).

172. Brandt, W. H., J. App. Phys., 16, 139, (1945).

173. Brandt, W. H., Trans. AIME, 167, 405, (1946).

174. Tiller, W. A., Liquid Metals and Solidification, ASM, (1958) p. 276.

175. Chadwick, G. A., Prog. in Mat. Sci., 12, 97, (1963).

177. Machlin, E. S., Trans. AIME, 197, 437,(1953).

178. Cottrell, A. H., Theoretical Structural Metallurgy, Arnold, (1955), p. 154.

179. Mullins, W. W., Sekerka, R. F., J. App. Phys. 35, 444, (1964).

180. Kirkaldy, J. S., Can. J. Phys. 42, 1447, (1964).

181. Bell, J. A., Ph.D. Thesis, U. of Toronto, (1965).

182. Chalmers, B., Principles of Solidification, Wiley, (1964), p. 202.

184. Johnson, A. A., Hughes, E. J., Barton, P. W., J. Metals, 17, 1014, (1965).

185. Smithells, C. J., Metals Reference Book, V. I, Butterworths, (1962), p. 236.

186. Metals Handbook, ASM, (1948), p. 901.

188. Ogilvie, R. E., private communication.

189. Hansen, M., Anderko, K., McGraw-Hill, (1958), p. 590.

190. Ginn, B. J., Brown, E. D., Brit. Welding J., 12, 901, (1965).

191. Mader, S., Widmer, H., d'Heurle, F. M., Nowick, A. S., App. Phys. Lett., 3, 201, (1963).

192. Mader, S., Norwick, A. S., App. Phys. Lett., 17, 57, (1965).

193. Ashby, M. F., Brown, L. M., Phil. Mag., 8, 1083, (1963).

194. Lücke, K., Stüwe, H. P., Recovery and Recrystallization, Interscience, (1963), p. 171.

195. Gerlach, W., Z. Metallkde, 28, 248, (1936).

197. Glansdorff, P., Prigogine, I., Physica, 30, 351, (1964).

198. Heidenreich, R. D., Fundamentals of Transmission Electron Microscopy, Interscience, (1964), p. 294.

199. Thomas, G., Transmission Electron Microscopy of Metals, (Wiley), (1962), p. 46, 155, 218.

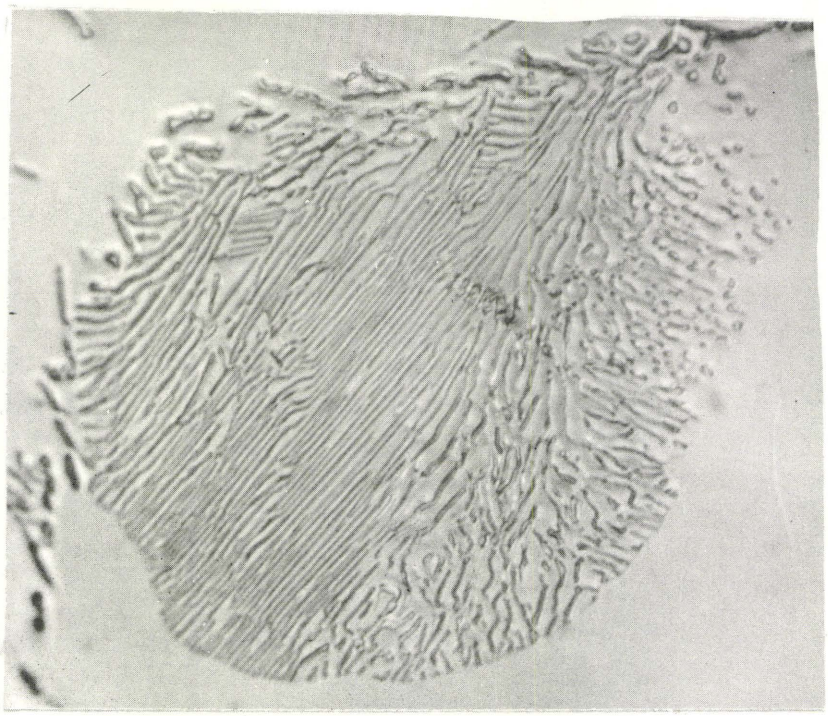

Fig. 1 Typical Cellular Precipitate, Cu-7.5 at % In, aged 10 hr. at 420°C. 1530X

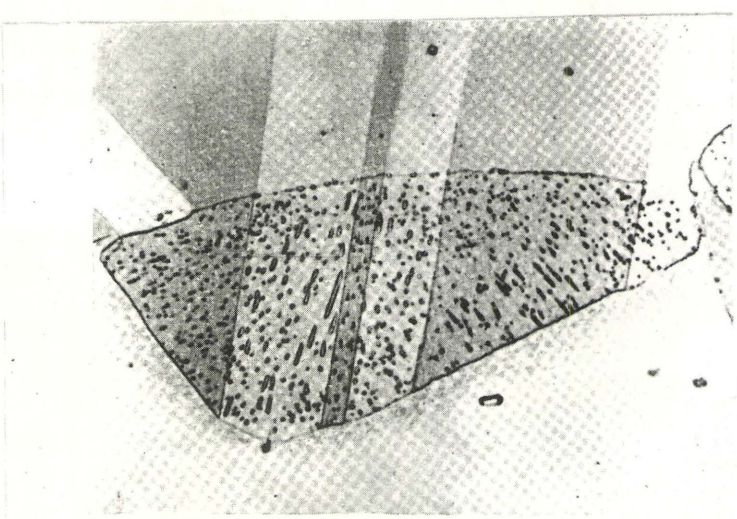

1000 ×

Three of the twins in the mother grain continue into the colony, but not the fourth. Same specimen as above.

Fig. 2 Cu - 1.82 wt % Cd, aged 4796 hr. at 300°C, Ref. 144.

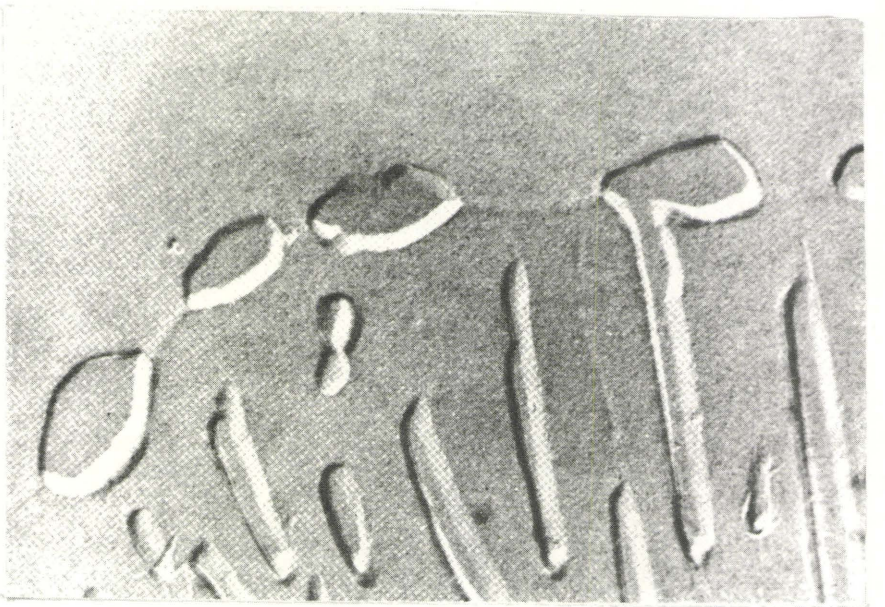

Fig. 3 Interfacial Precipitation in Nb - 8,7 wt % Cr. 6 hr. at 1205°C. 10,000X. Ref. 43.

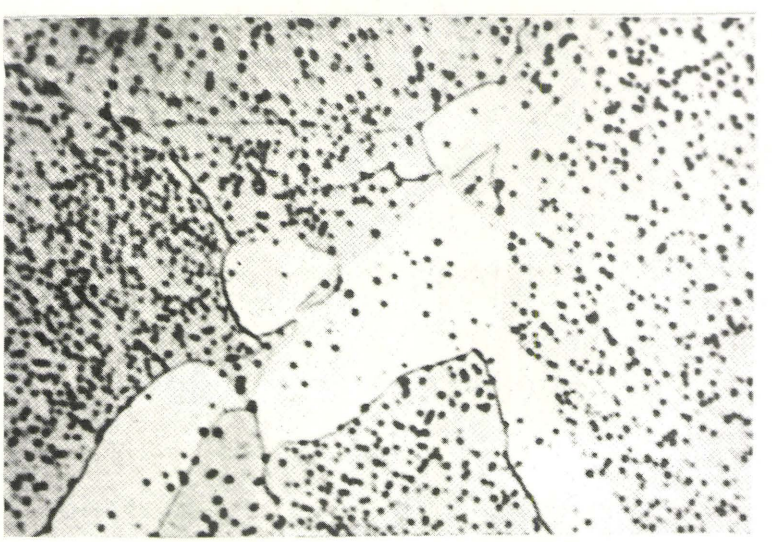

A slightly advanced stage of the discontinuous dissolution process in the $\alpha + \beta$ range. The 2.75 wt. % Cd alloy solution annealed 2 min at 500 C after complete discontinuous precipitation at 350 C ×2500

Fig. 4 Cu - Cd alloy, Ref. 11.

FIGURE 5

Legend

Curve	Alloy	Reference
1 - 1	Pb - 11.2 At % Sn	28
1 - 2	" 12.4 " " "	"
1 - 3	" 14.7 " " "	"
1 - 4	" 17.0 " " "	"
2 - 1	Cu - 2.90 wt % Cd	144
2 - 2	" 3.81 " " "	
3 - 1	Fe - 30 wt % Ni - 6 Ti	15
4 - 1	Cu - 10 wt % In	27
4 - 2	" 12.5 " "	
4 - 3	" 15 " "	
5 - 1	Cu - 5.13 wt % In	Present work.
5 - 2	" 7.51 " "	
5 - 3	" 10.07 " "	

(These last results may be disregarded for the discussion in Chapter 1.)

FIG. 5

RECIPROCAL SPACING VERSUS REDUCED TEMPERATURE

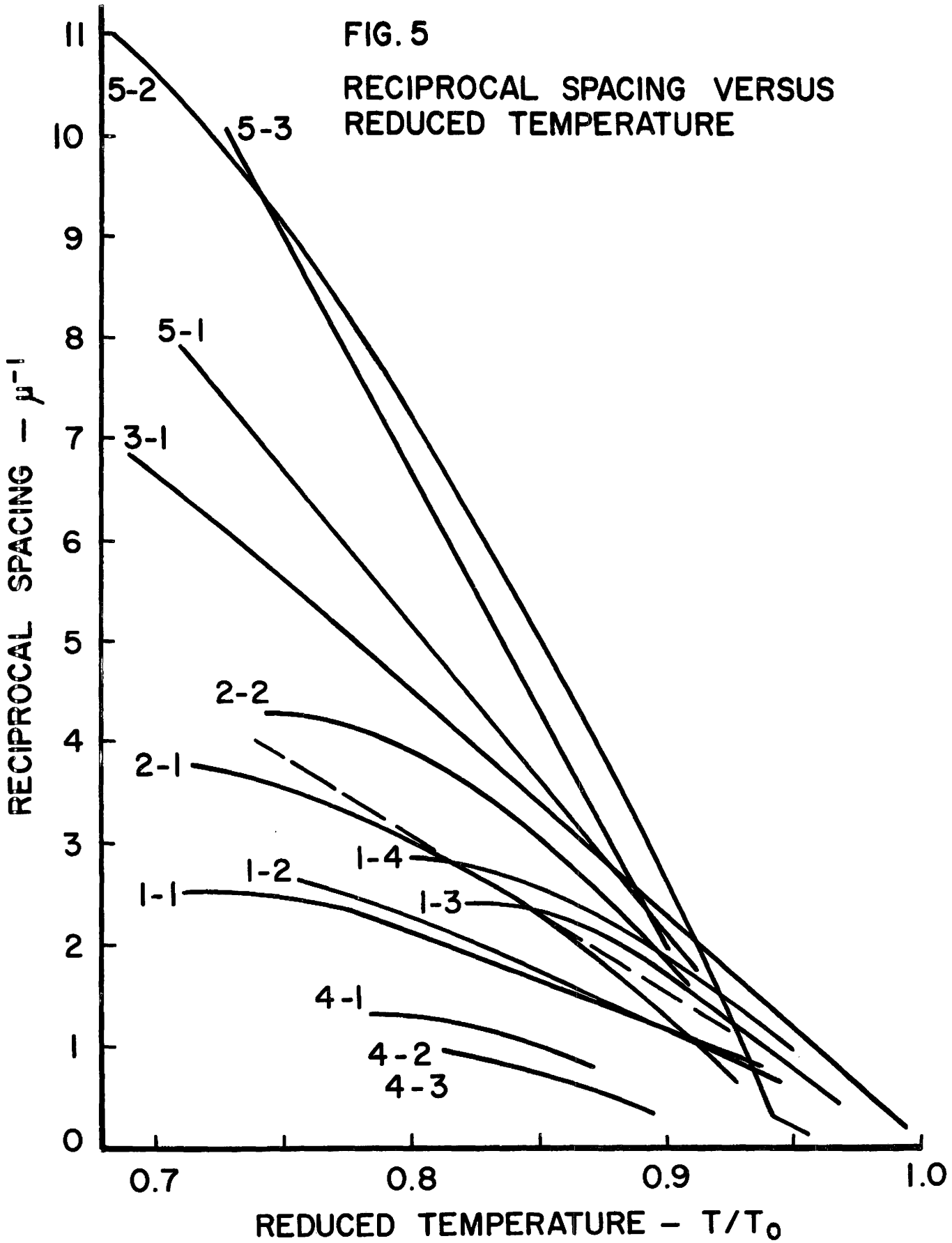

FIG. 6 COMPOSITION – TEMPERATURE RELATIONS FOR DISCONTINUOUS DISSOLUTION

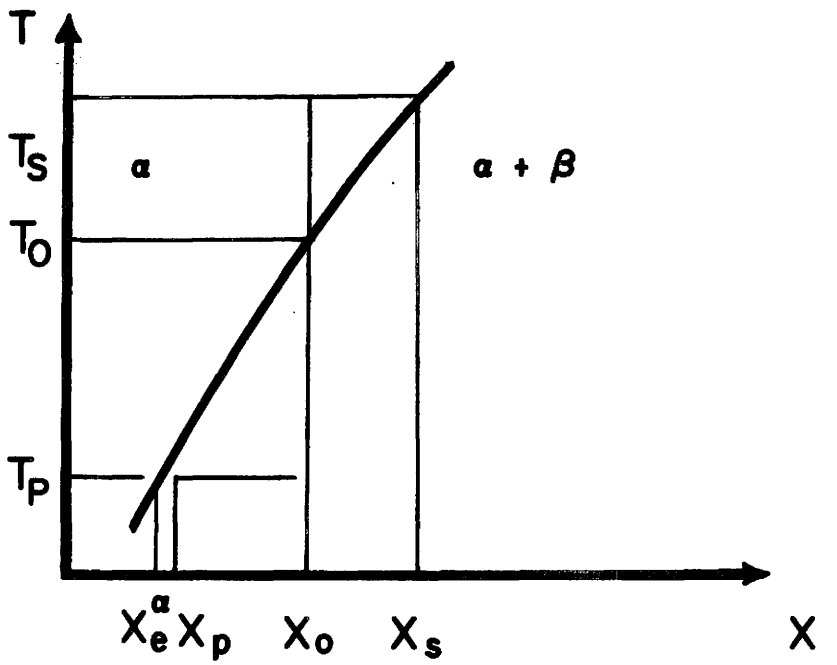

a. PHASE DIAGRAM

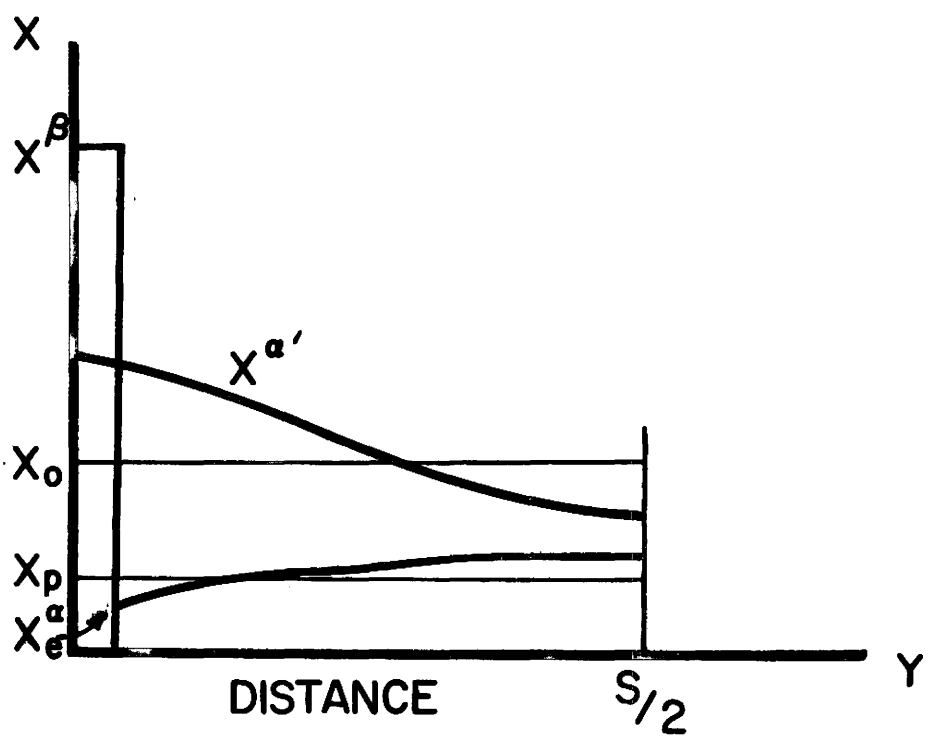

b. COMPOSITION – DISTANCE

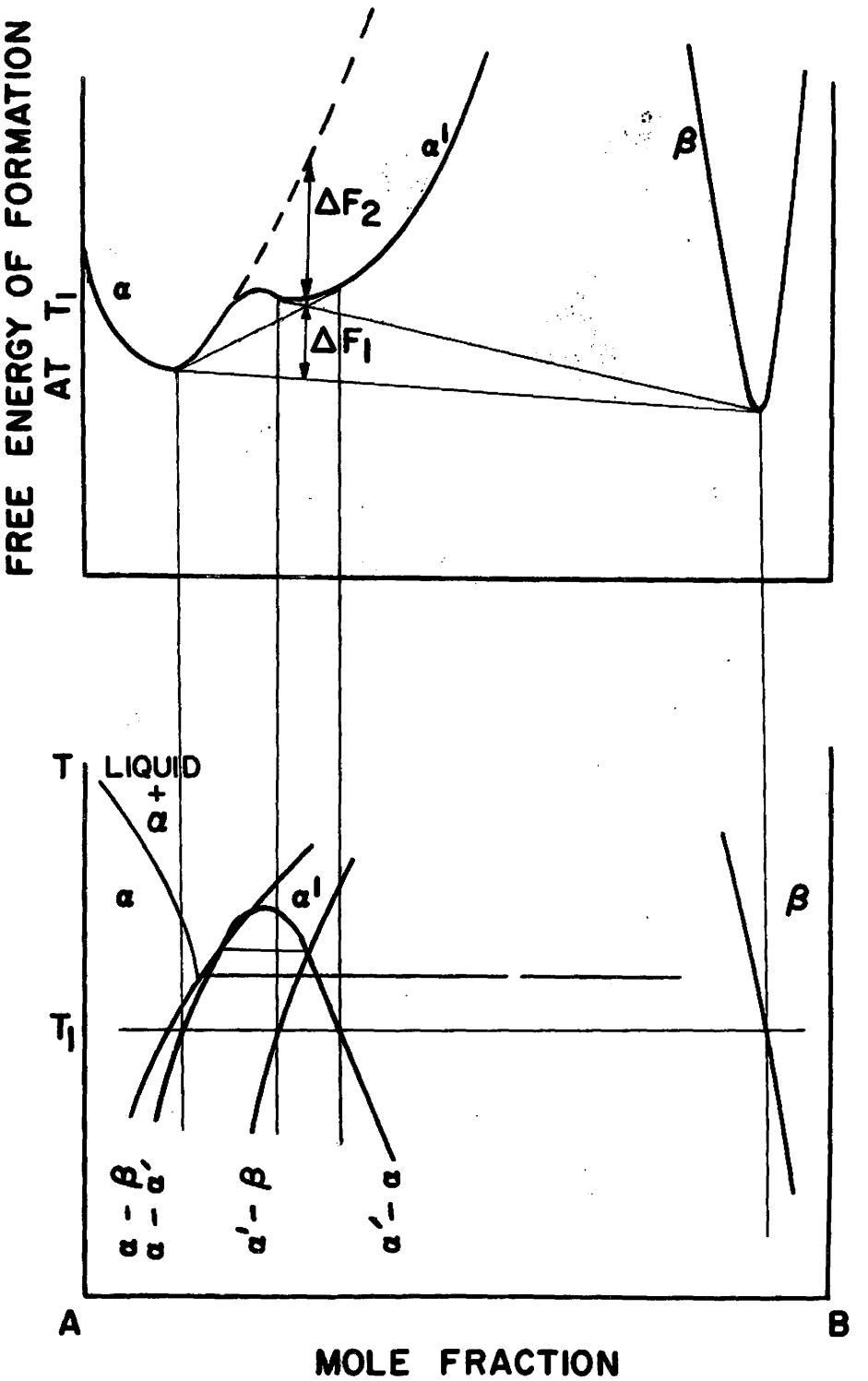

FIG. 7 FREE ENERGY CURVES AND PHASE DIAGRAM FOR METASTABLE MONOTECTOID REACTION

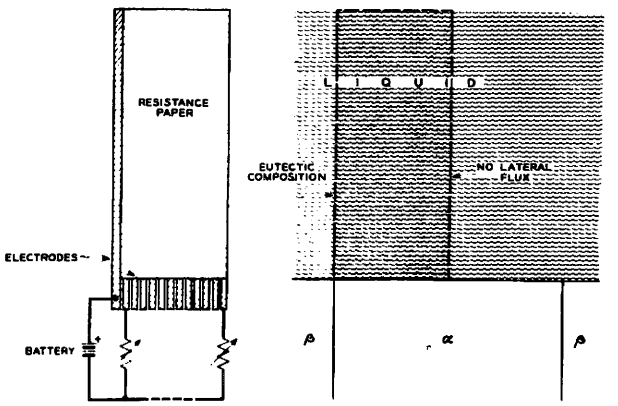

(*a*) Resistance paper with electrodes. The electrode on the left edge imposes a constant potential; the free right-hand side and top edge permit no current to flow across these lines. The resistors are adjusted to give the same current from each of the electrodes along the bottom. (*b*) The dotted area shows the portion of the lamellar growth front represented by the resistance paper, and the corresponding boundary conditions.

Fig. 9 The Electric Analogue for Eutectic Growth. Ref. 117.

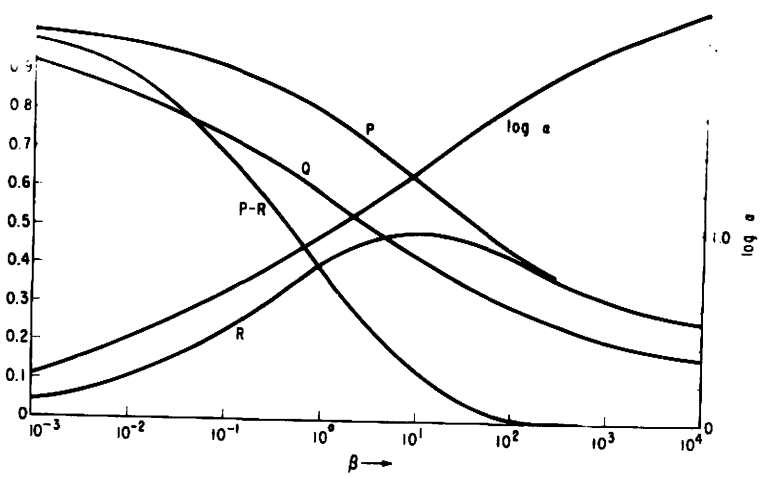

Precipitation from dilute solution as a function of the parameter $\beta = \xi M V^2 \sigma^2 / D_B \delta \Delta F_0$

P the fraction of ΔF_0 realized.
Q the fraction of material precipitated.
R the fraction of ΔF_0 expended on surface energy.
$P - R$ the fraction of ΔF_0 exerting a pressure on the cell boundary

Fig. 11 Ref. 22

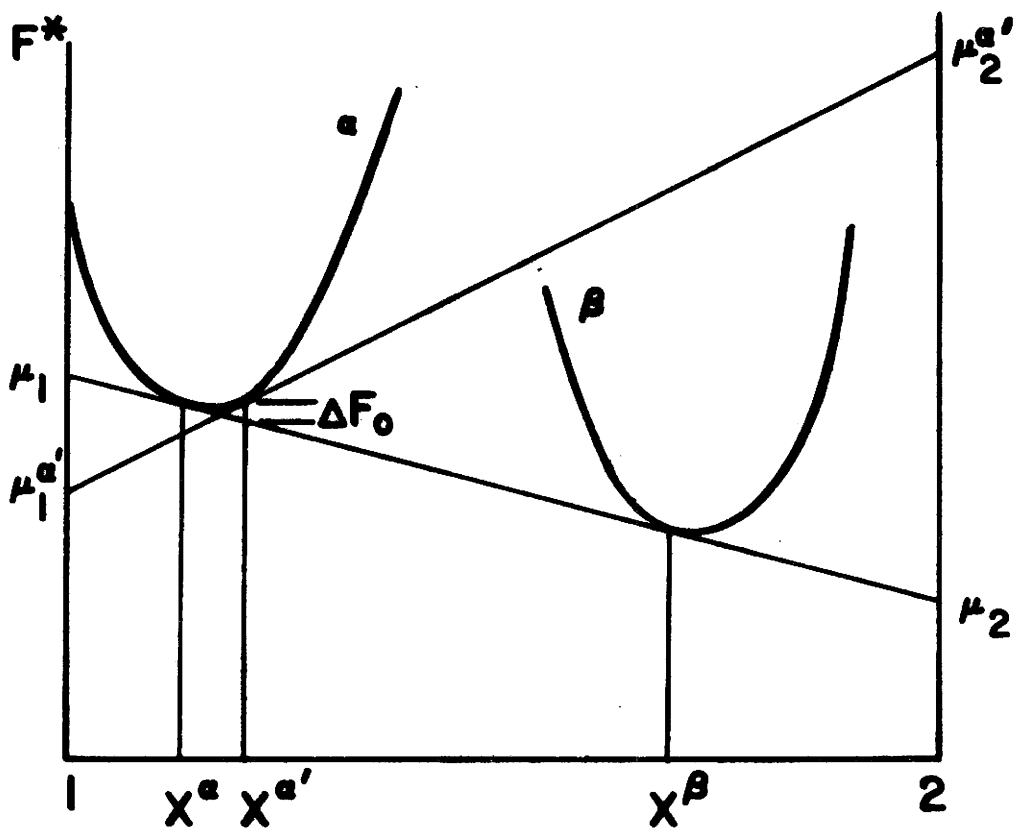

FIG. 10 A POSSIBLE FREE ENERGY OF FORMATION VERSUS COMPOSITION DIAGRAM FOR DISCONTINUOUS PRECIPITATION.

FIG. 12 THE MATRIX – NODULE OR AUSTENITE PEARLITE INTERFACE

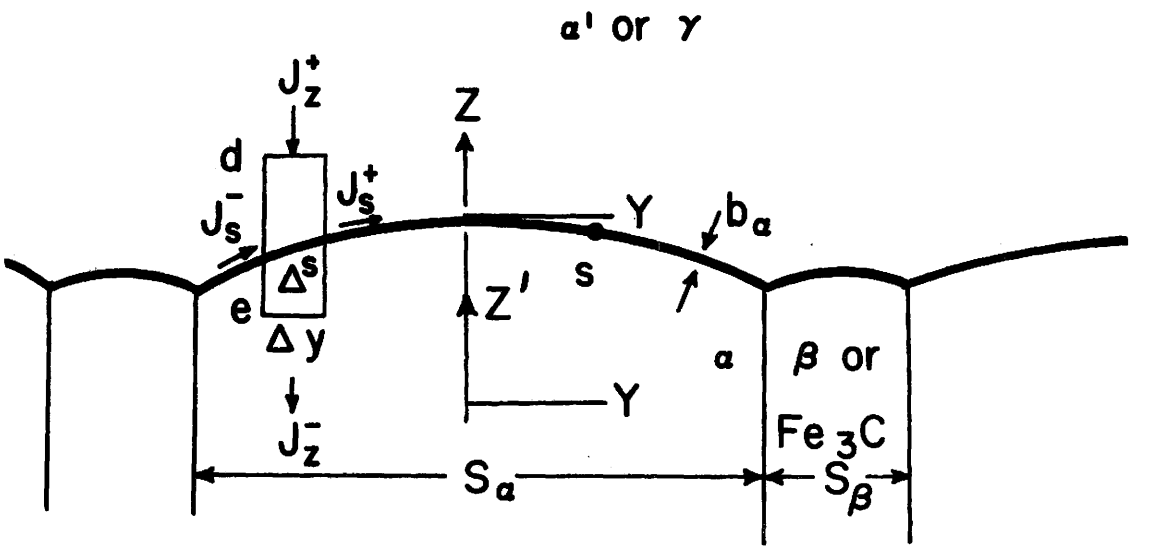

FIG. 13 ANGLES AT THE $\alpha' - \alpha - \beta$ JUNCTURE

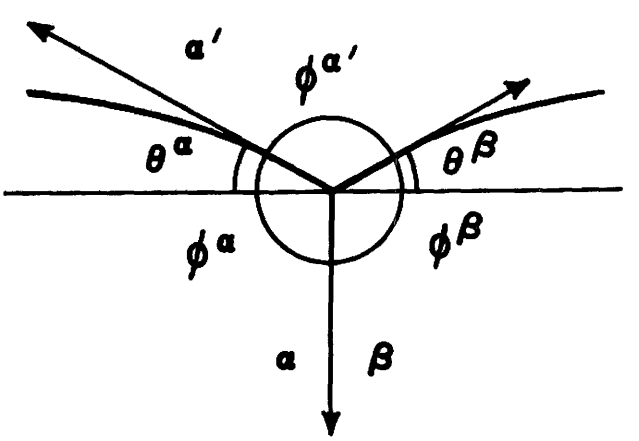

FIG. 14 .FREE ENERGY VERSUS COMPOSITION FOR A SYMMETRIC EUTECTOID.

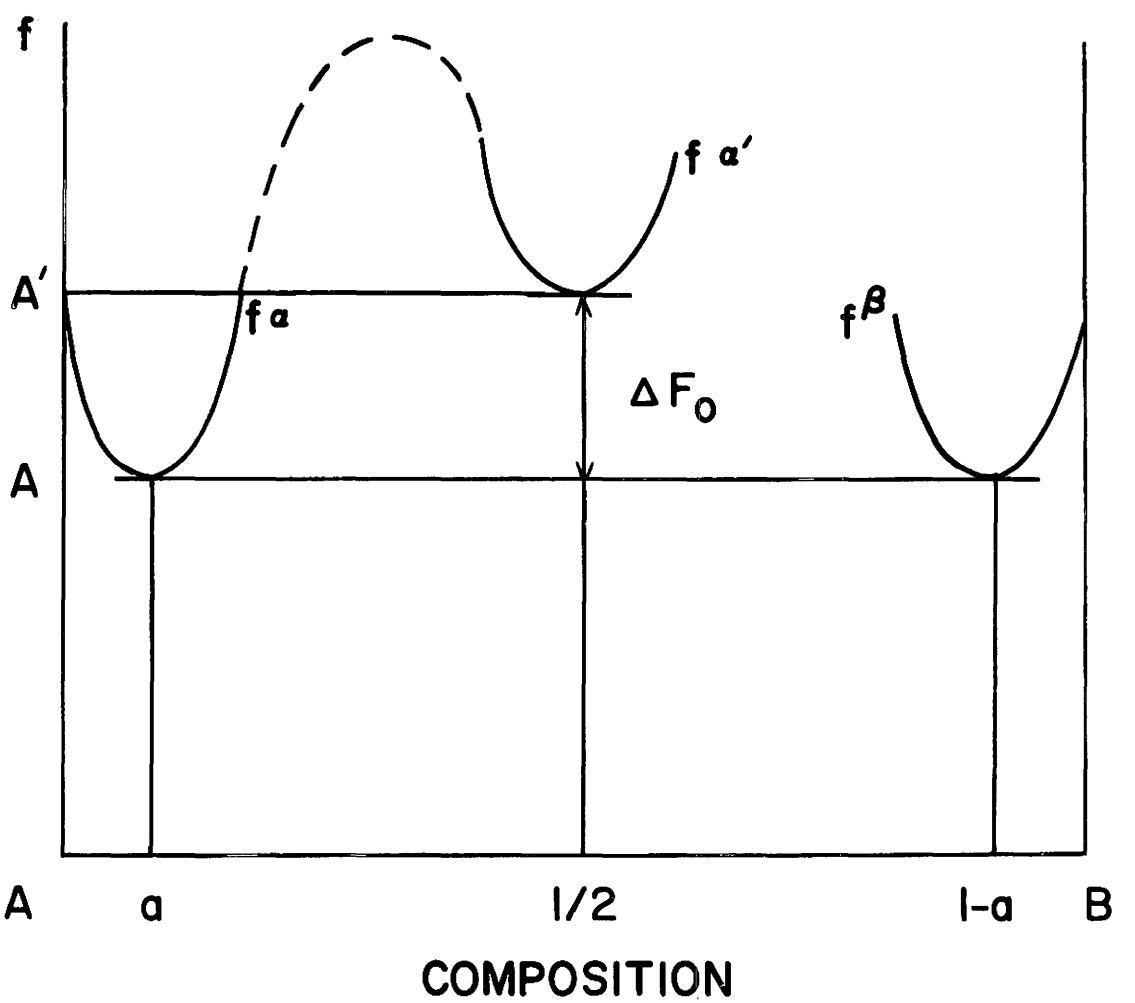

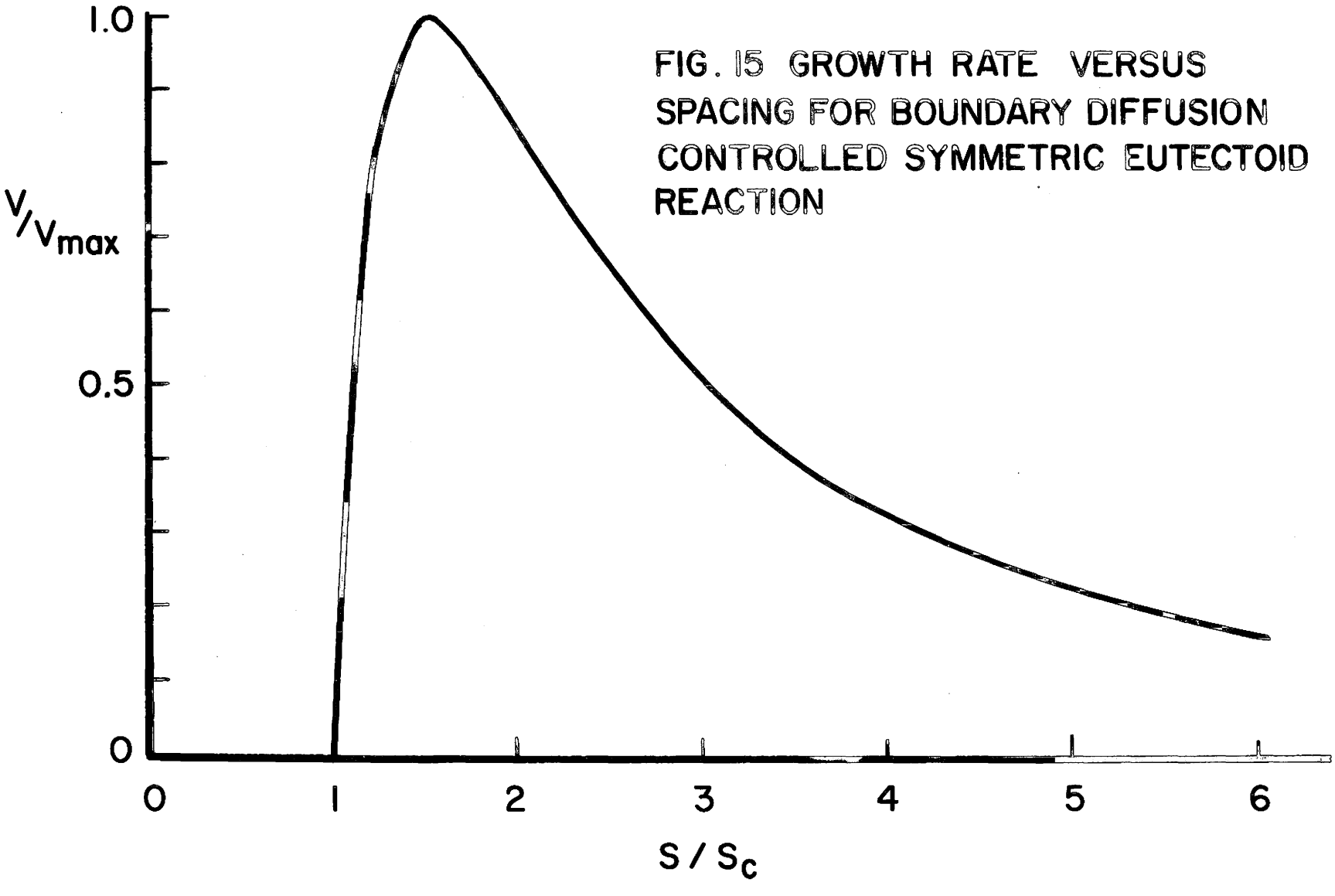

FIG. 15 GROWTH RATE VERSUS SPACING FOR BOUNDARY DIFFUSION CONTROLLED SYMMETRIC EUTECTOID REACTION

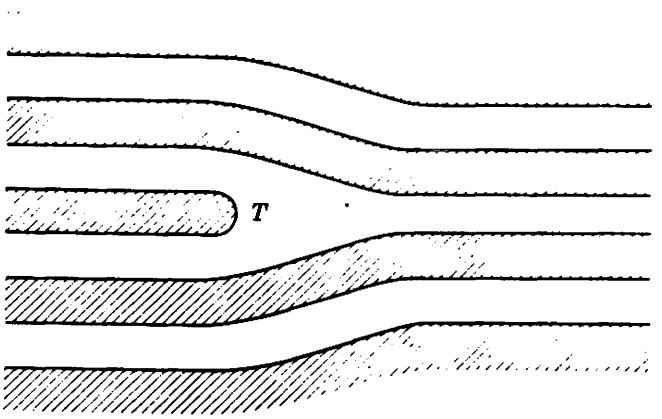

Termination of lamellar (schematic).

Fig. 16 Ref. 187.

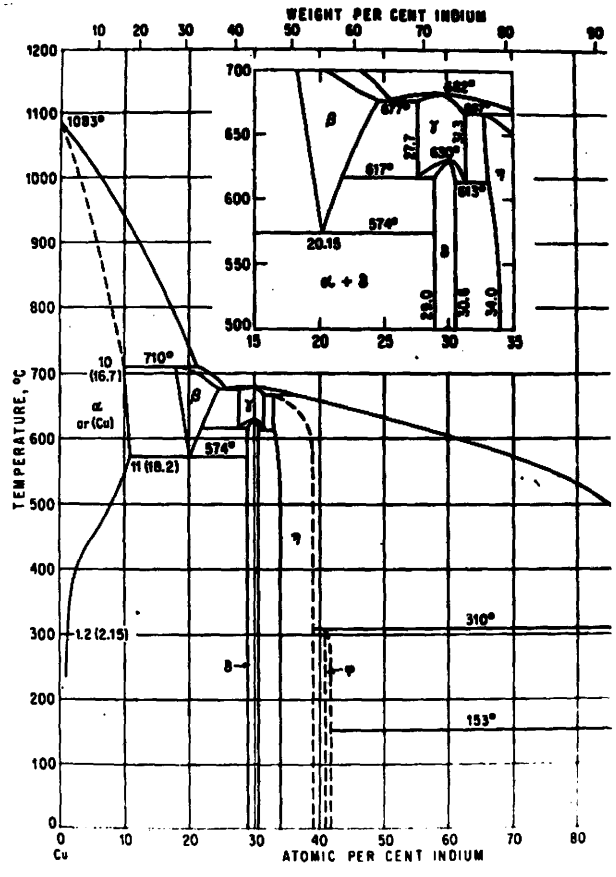

FIG 17a. Cu — In PHASE DIAGRAM FROM REF. 189

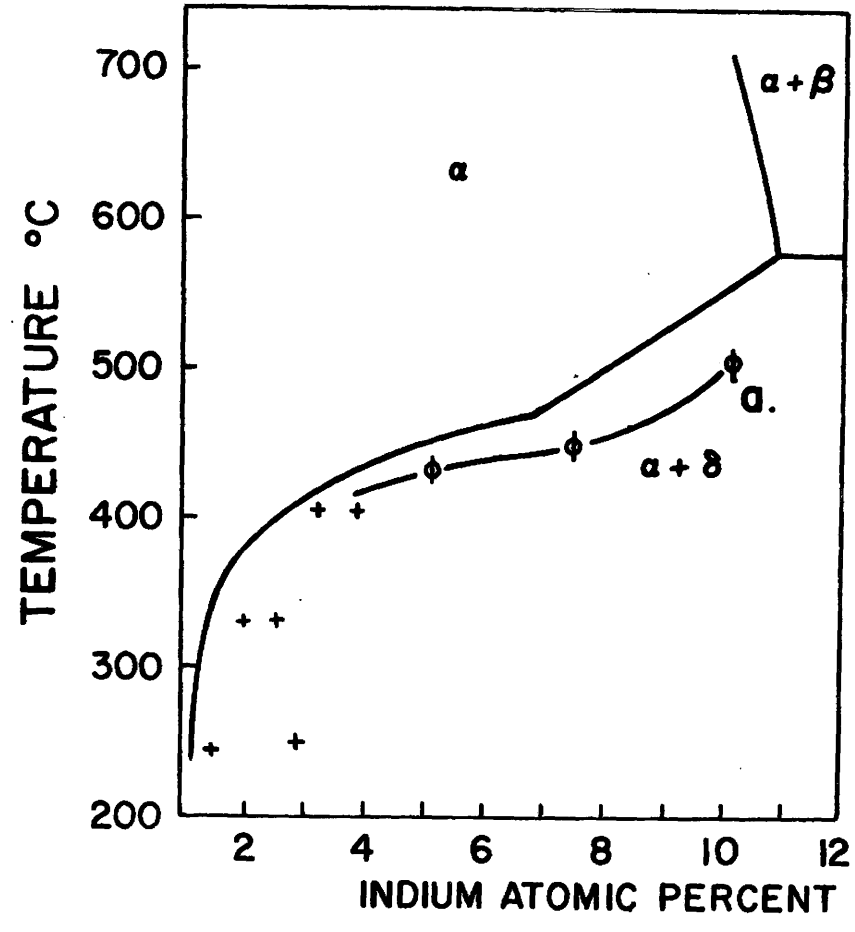

FIG 17b. FROM REF. 163
+ α PHASE COMPOSITION FROM TABLE 13.
φ TEMPERATURE FOR WHICH 1/S → 0 FROM TABLE 12

FIG. 18 ALLOY PREPARATION APPARATUS

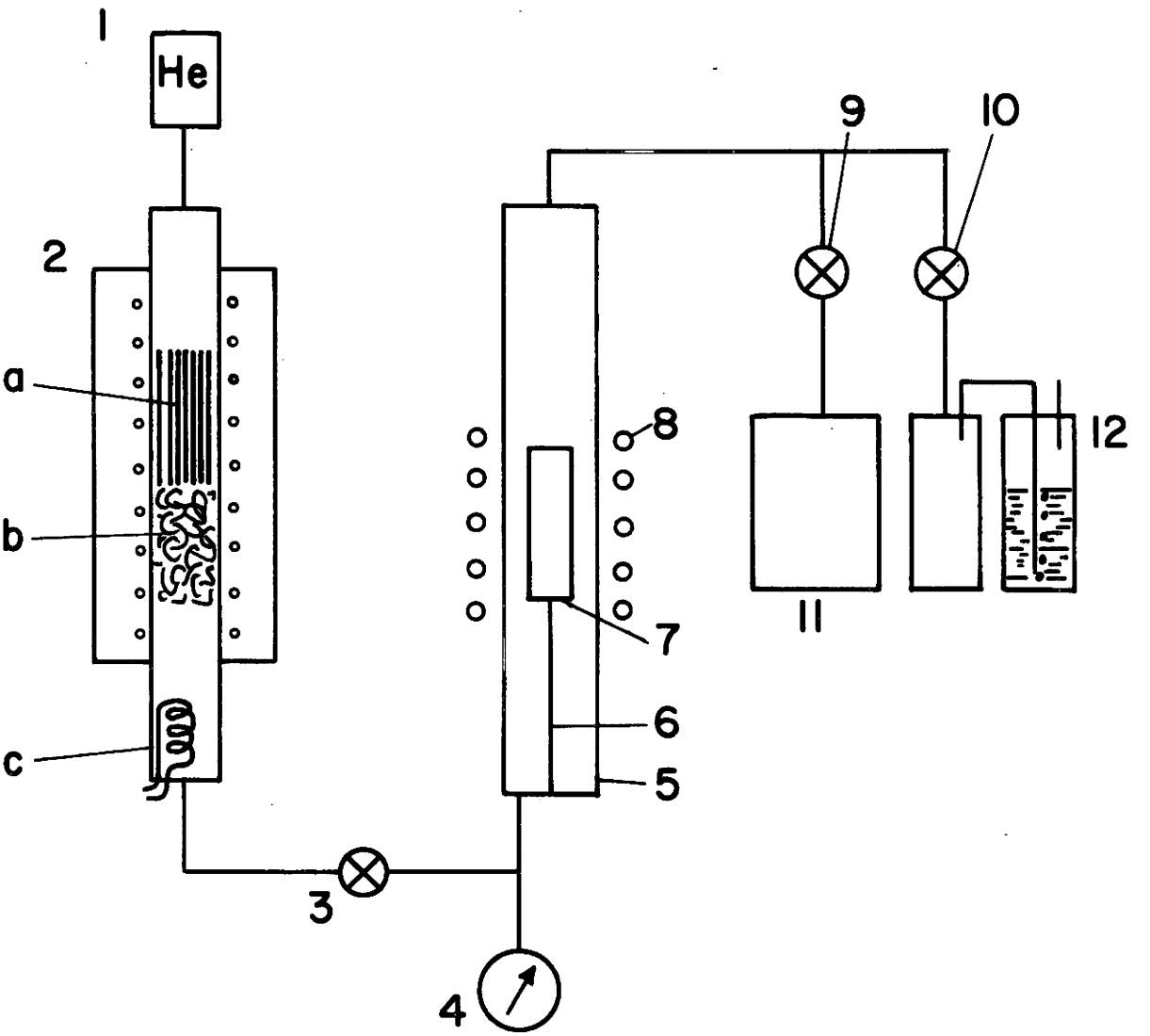

1. Helium Source
2. Helium Cleaning Furnace
2a. Copper Tubing
2b. Copper Turnings
2c. Gas Cooling Coil
3. Valve
4. Vacuum Gauge
5. Pyrex Tube
6. Refractory Rod
7. Graphite Crucible
8. Induction Coil
9. Valve
10. Valve
11. Vacuum Pumps
12. Bubbler

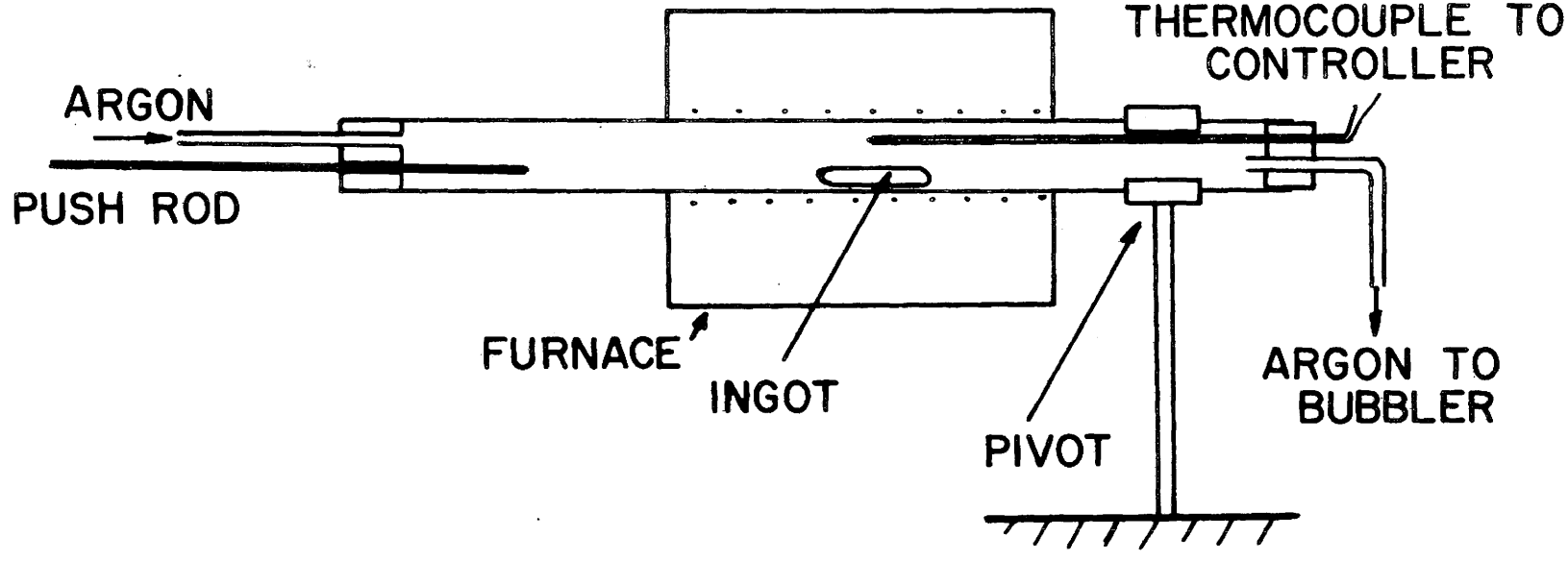

FIG. 19 FURNACE FOR HOT ROLLING

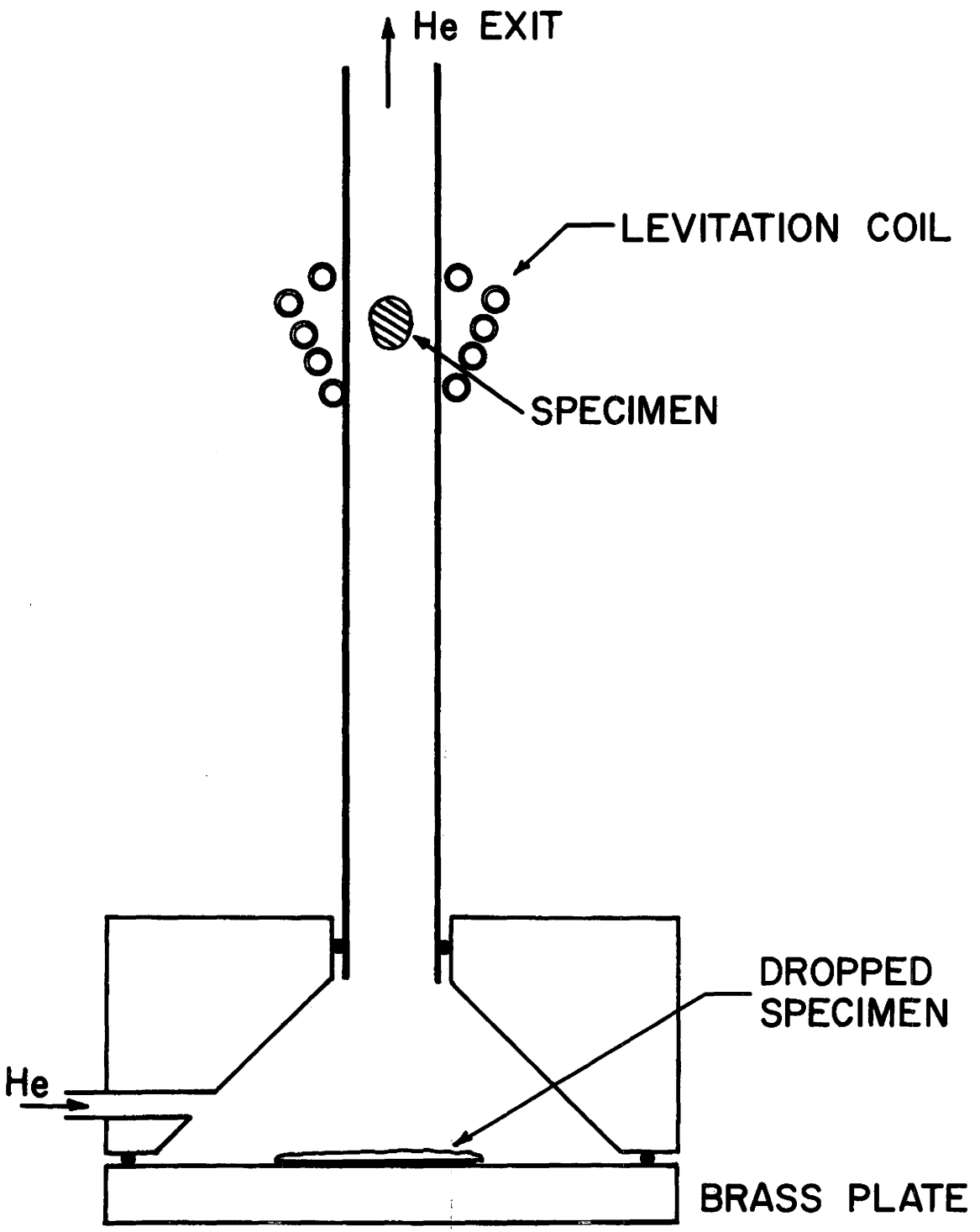

FIG. 20 LEVITATION MELTING APPARATUS

FIG. 21

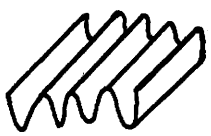

a. MOLYBDENUM SEPARATOR

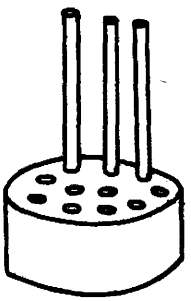

b. GRAPHITE SEPARATOR

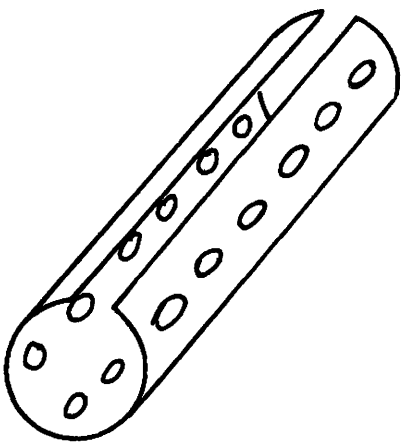

c. MOLYBDENUM PROTECTOR

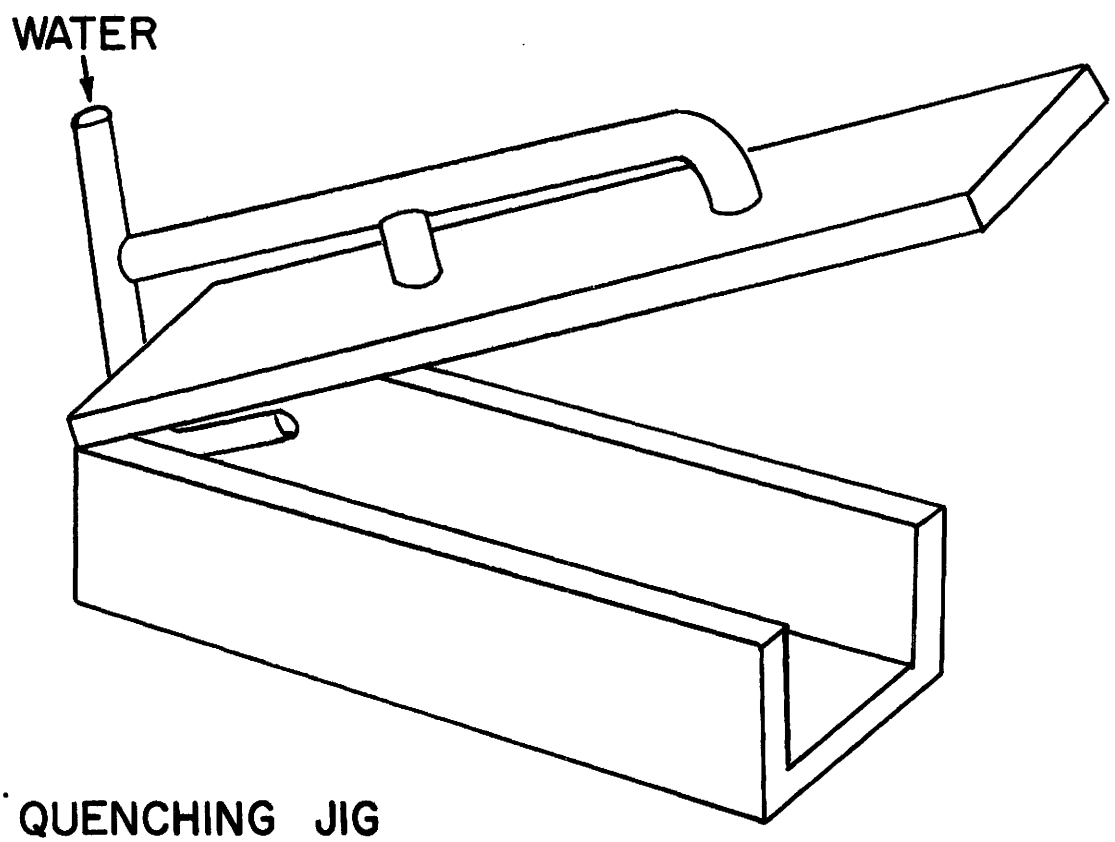

d. QUENCHING JIG

FIG. 22 a ELECTROPOLISHING CELL

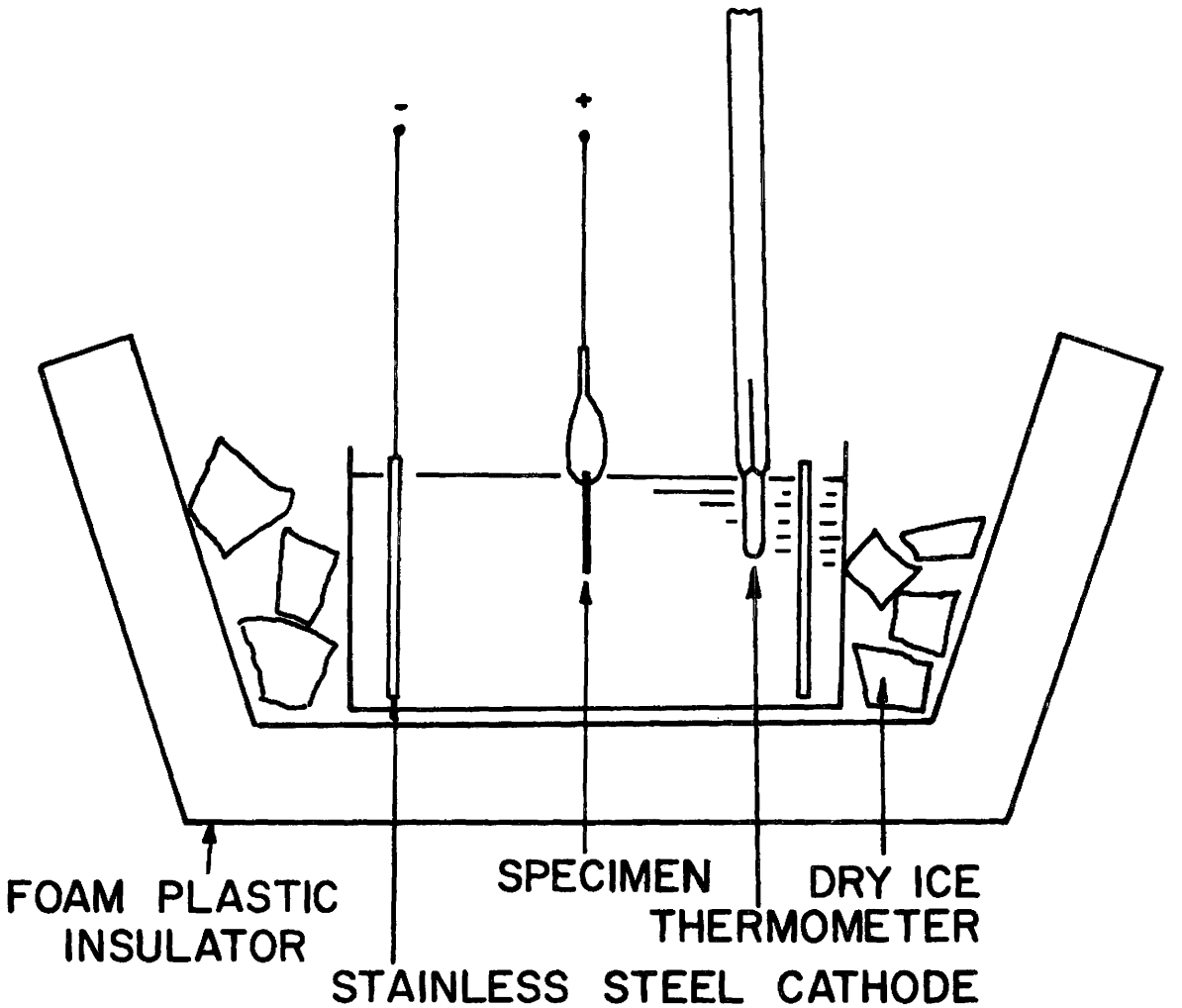

b SPECIMEN LACQUERED

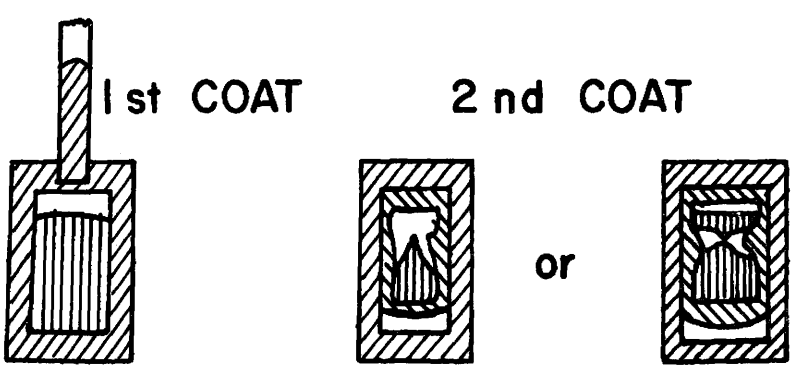

Fig. 23 Oblique lamellae in 5.1% In, 395°C, 84 hrs. 12,000X.

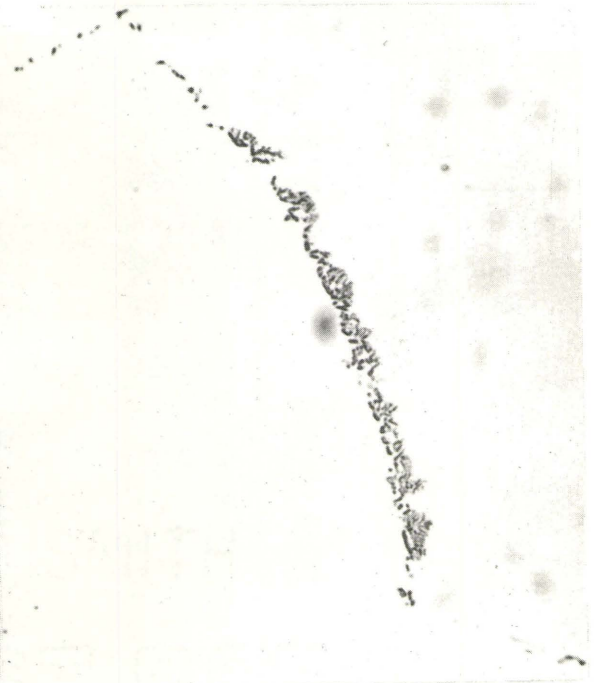

Fig. 24 Cell Beginning in 7.5% In, 404°C, 86 min, 650X.

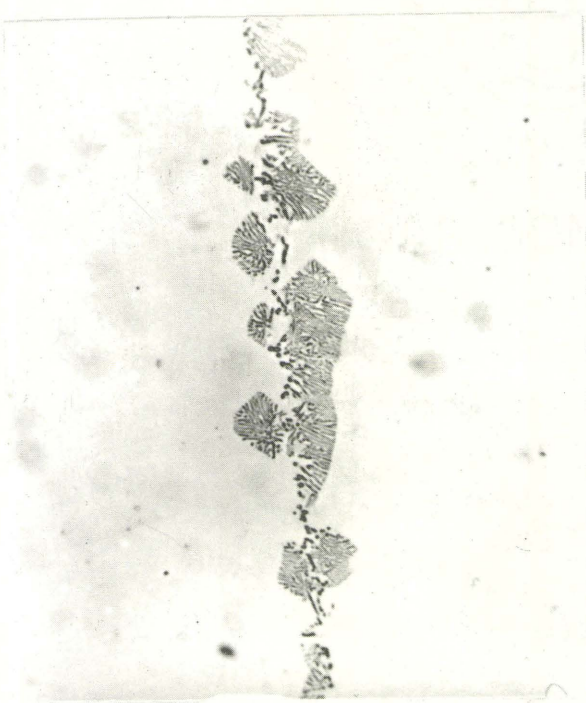

Fig. 25 Cell growth in 75% In, 404°C, 290 min, 650X.

Fig. 26 Cell Beginning in 7.5% In, 404°C, 290 min, 15,000X.

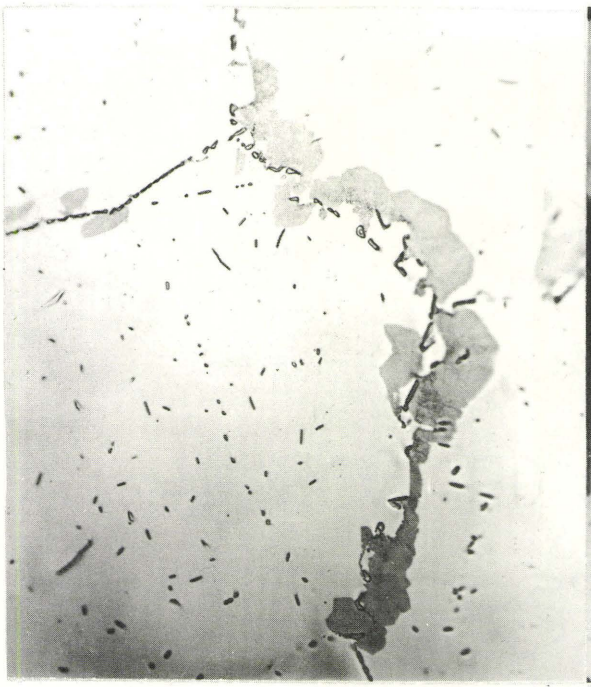

Fig. 27 7.5% In. 447°C,- 24 hr.; then 330°C,- 10 hr. 400X.

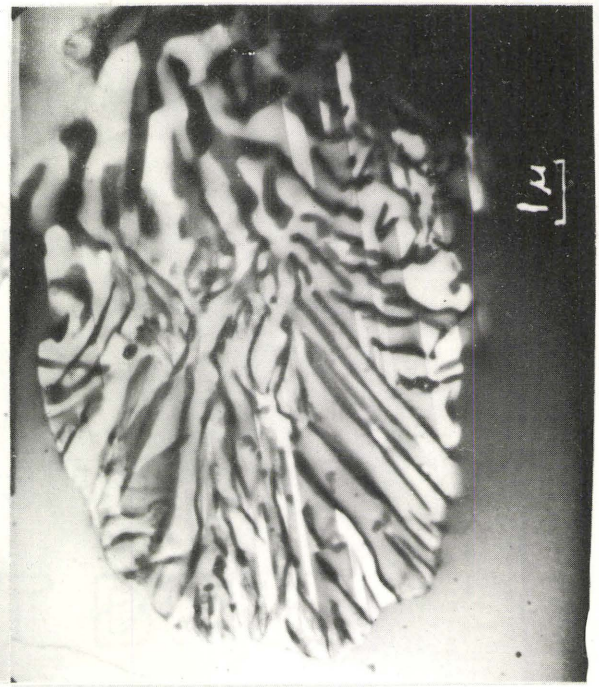

Fig. 28 5.13%, 345°C, 18 hr. 10,000X

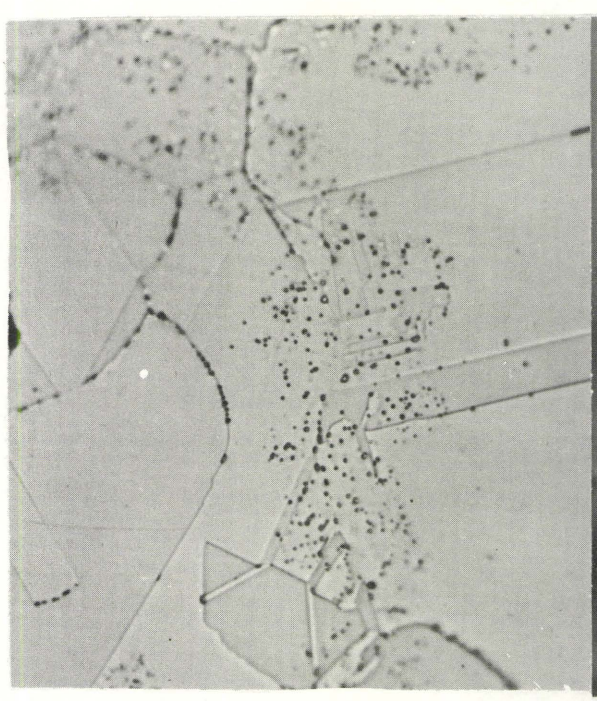

Fig. 29 7.5% In 330°C, 11 hr; then 470°C, 24 hr, 630X.

Fig. 30 7.5%, 432°C, 15 hr. 7,000X.

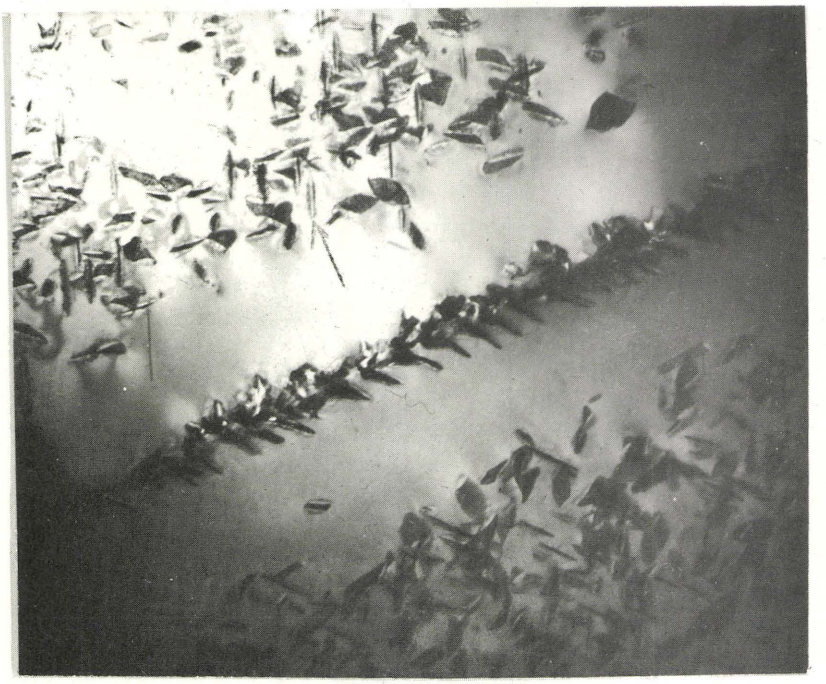

Fig. 31 10.1% In, 246°C, 207 hr., 15,200X

Fig. 33 10.1% In, 246°C, 207 hr., 29,000X

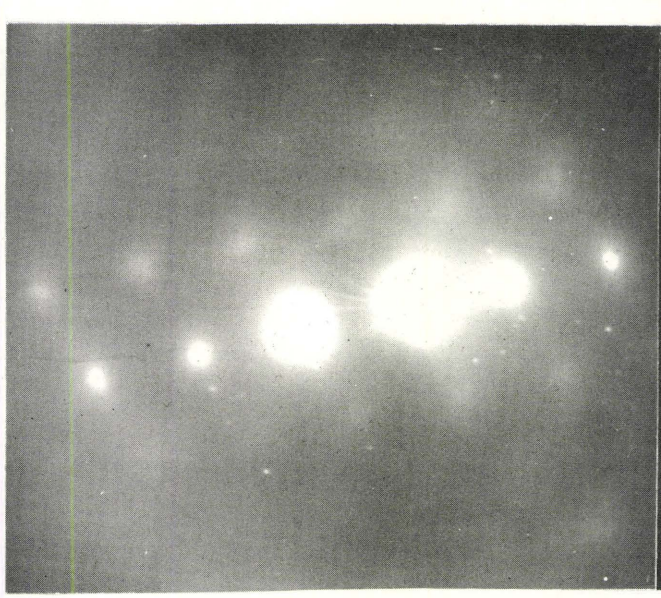

Fig. 34a Diffraction of area of Fig. 33

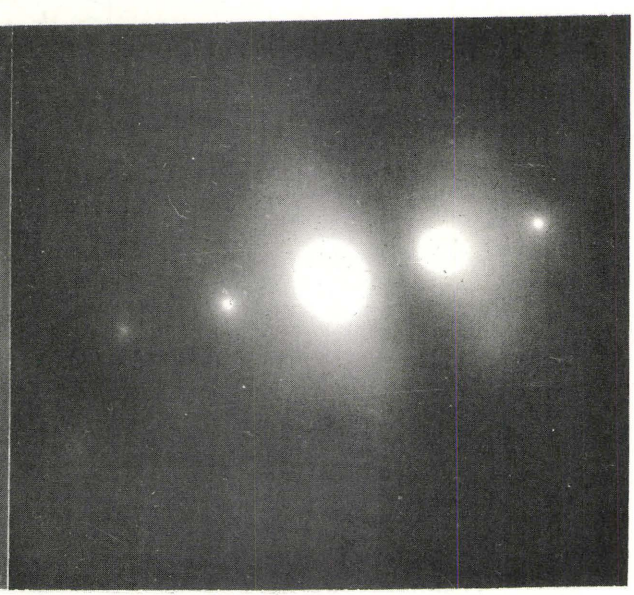

Fig. 34b Diffraction of area of Fig. 33 for orientation where δ' is not visible

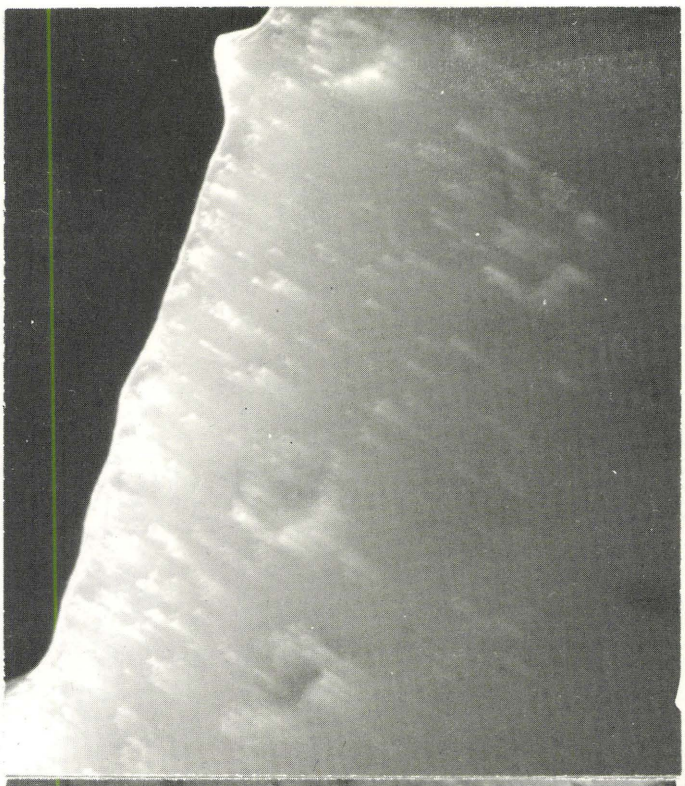

Fig. 35

10.1% In, 246°C, 207 hr. Dark field, using strong (111) beam. 47,000X.

Fig. 36 10.1 % In, 246°C, 207 hr. 93,000X

Fig. 37 10.1% In, 330°C, 310 min. 93,000X

Fig. 38 10.1 % In, 404°C, 230 min. 1500X.

Fig. 39 10.1 % In, 404°C, 60 min. 80,000X

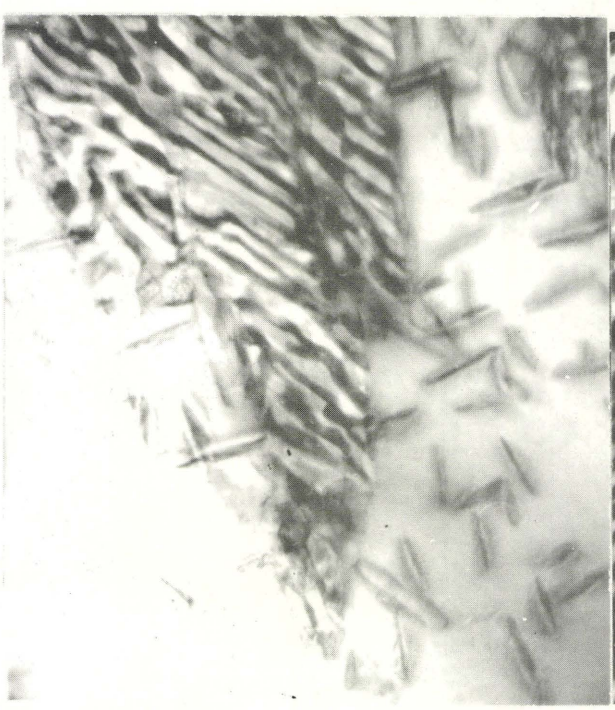

Fig. 40 10.1 % In, 246°C, 207 hr. 40,000X

Fig. 41 10.1 % In, 4001°C, 230 min. 14,000X

Fig. 42 Variation of Grain Boundary Occupation with Temperature

a. 7.5 % In. 328°C, 11.3 hr, 400X.

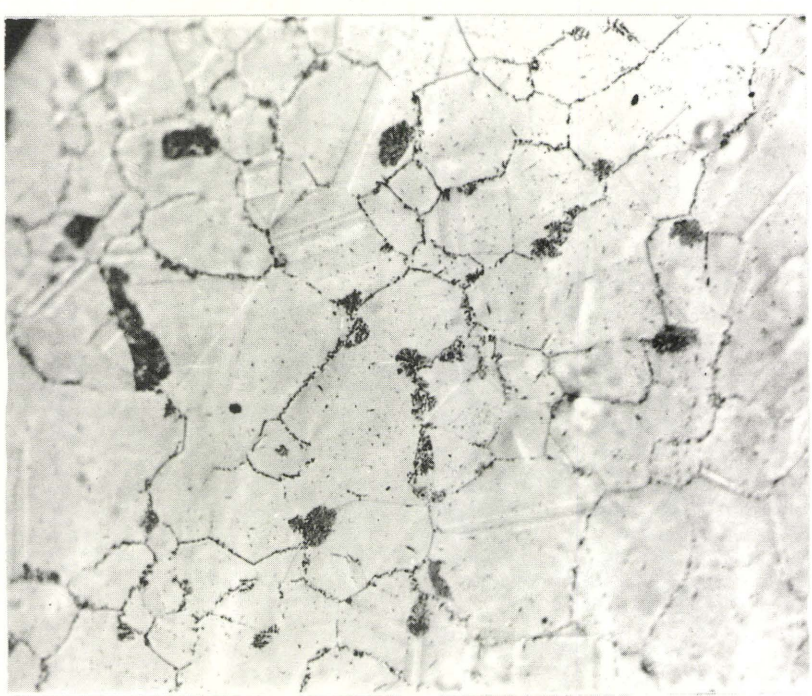

b. 7.5 % In. 432°C, 16 hr, 150X.

FIG. 43
HISTOGRAM OF CELL GROWTH DISTANCE

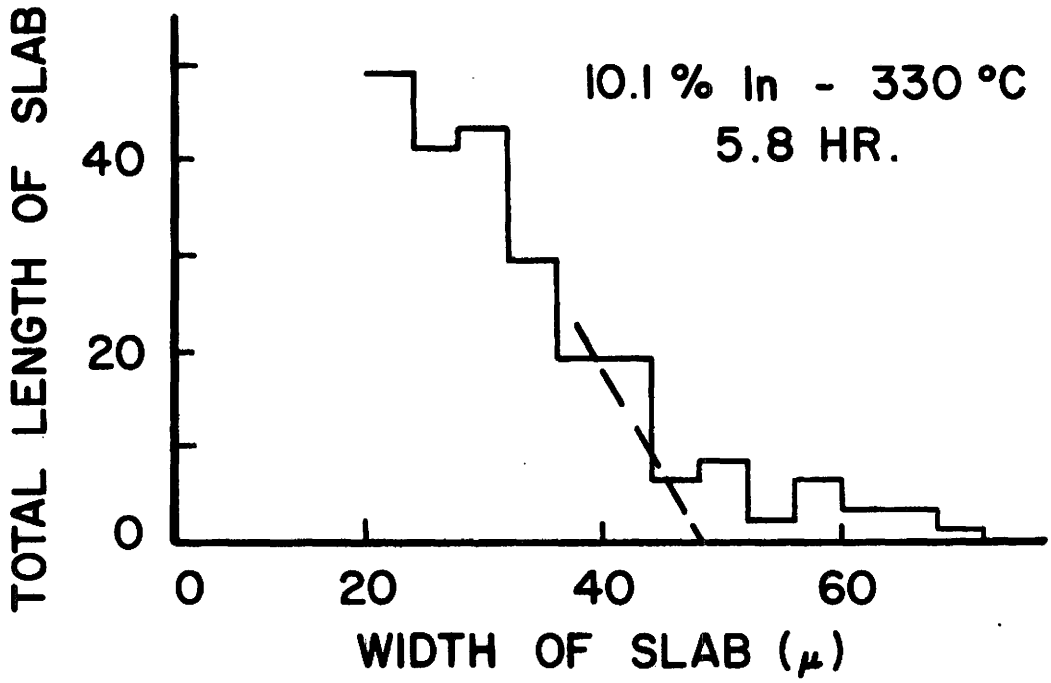

FIG. 44
GROWTH DISTANCE VERSUS TIME

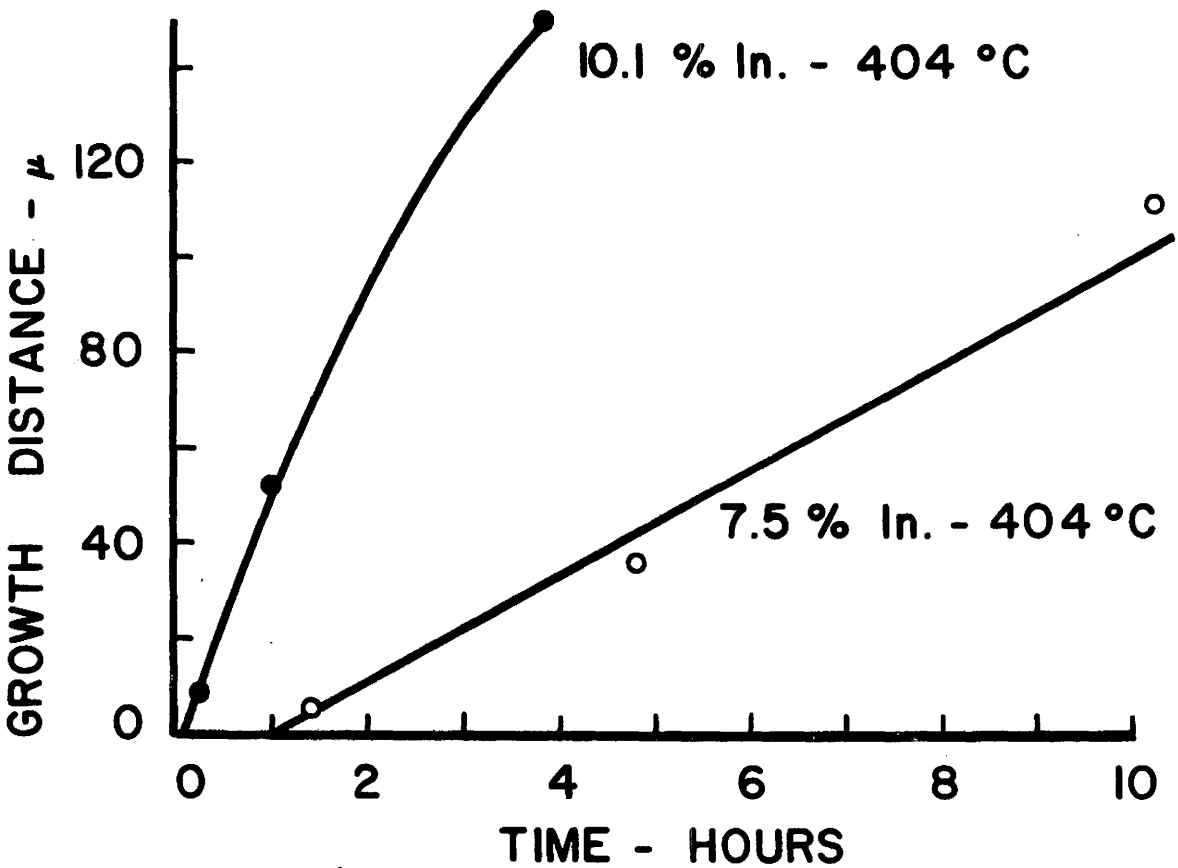

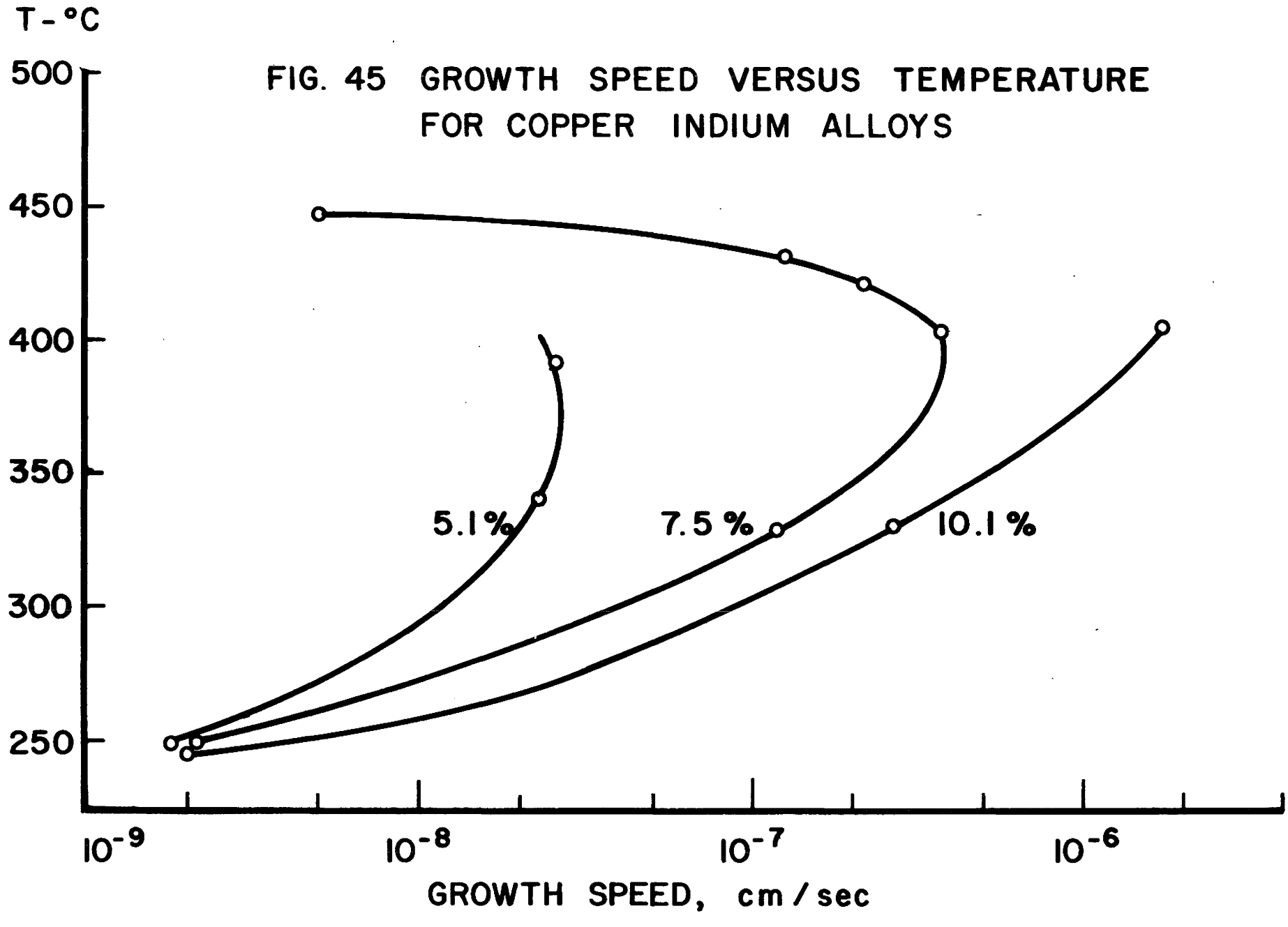

FIG. 45 GROWTH SPEED VERSUS TEMPERATURE FOR COPPER INDIUM ALLOYS

FIG. 46 GROWTH SPEED VERSUS COMPOSITION

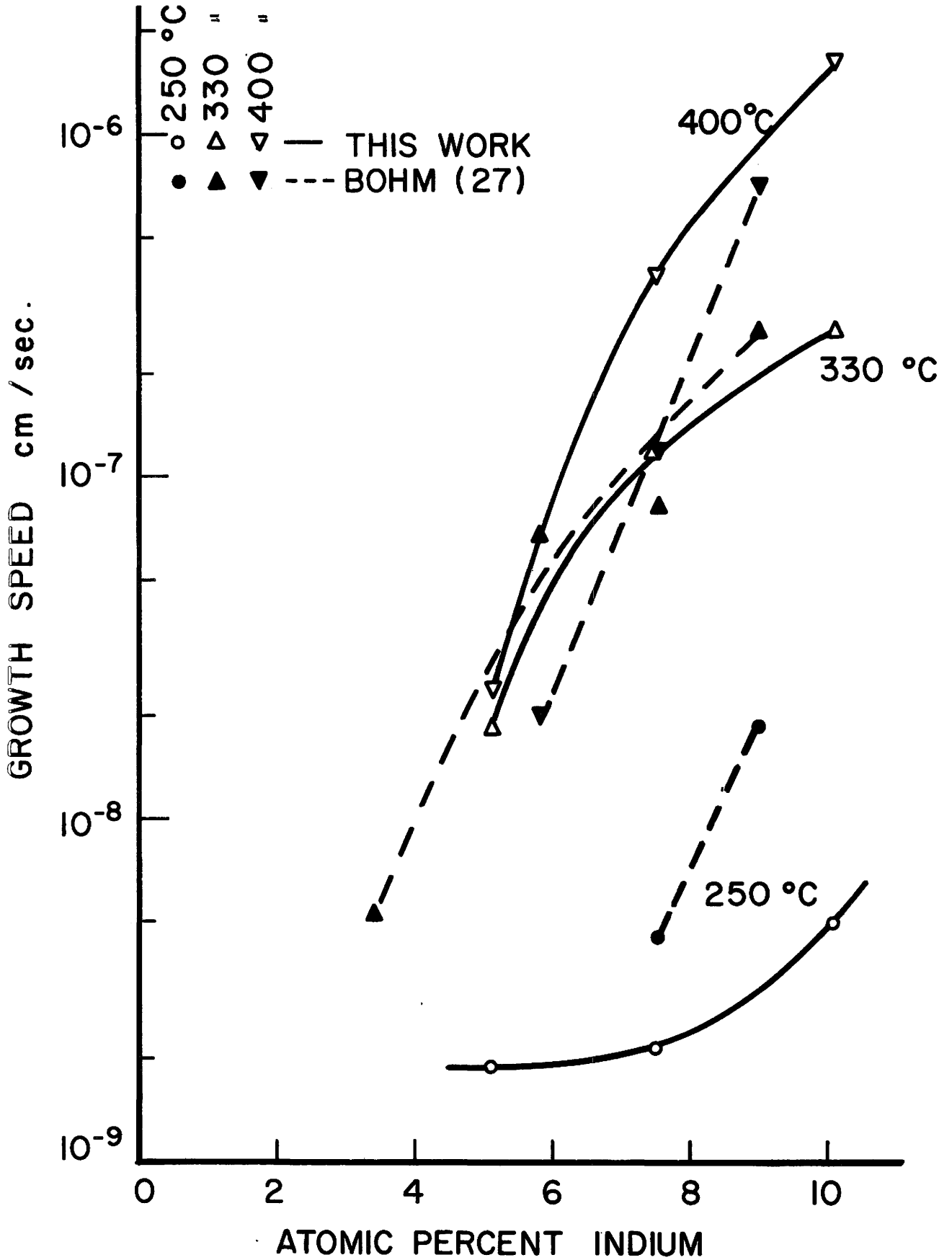

FIG. 47 RECIPROCAL OF LAMELLAR SPACING VERSUS TEMPERATURE FOR COPPER INDIUM ALLOYS

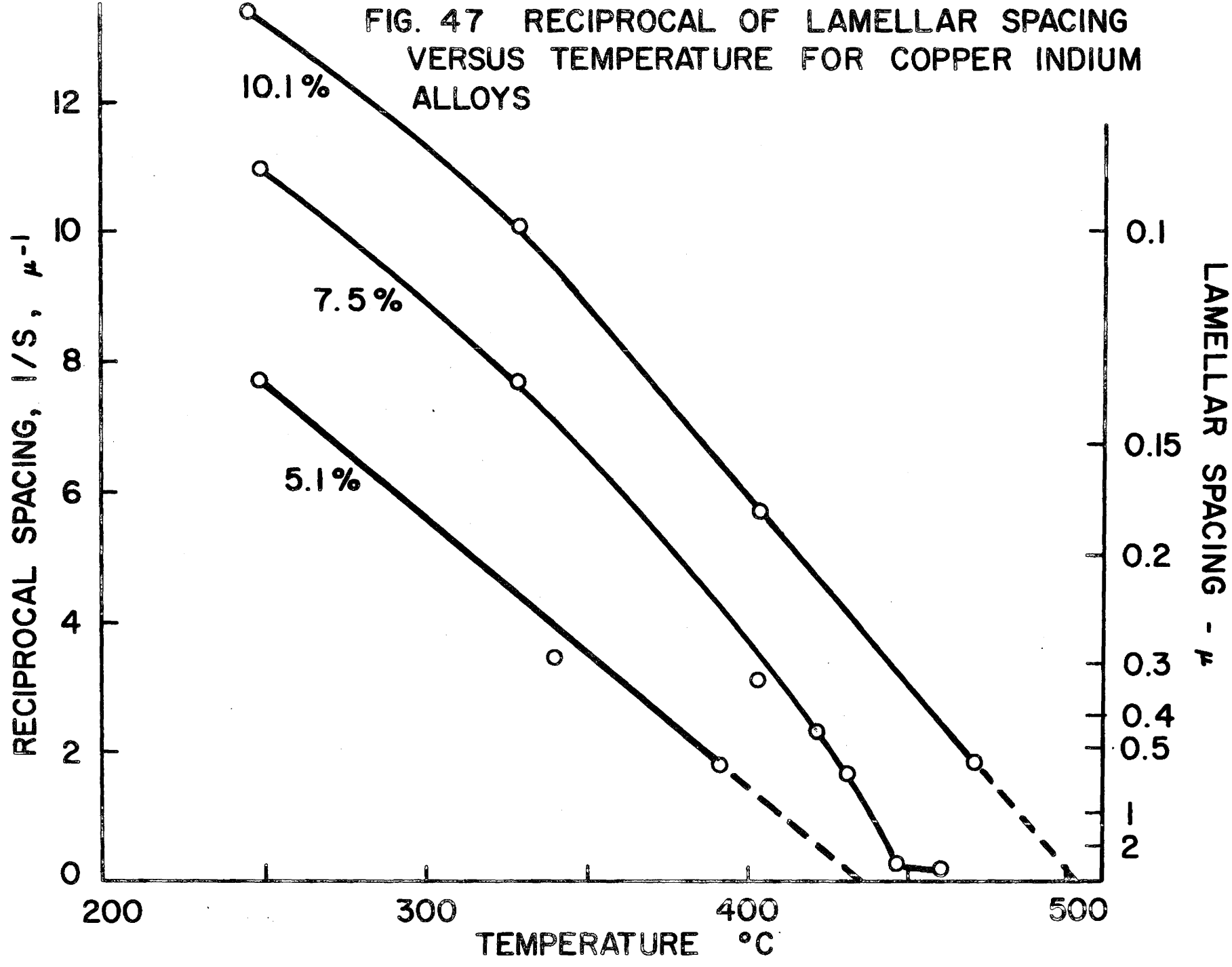

Fig. 48 7.5 % In, 461°C, 72 hr, 760X.

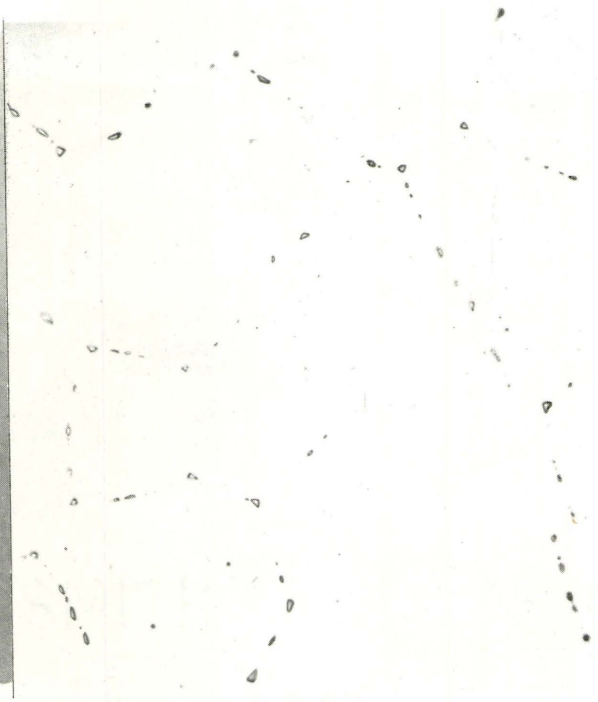

Fig. 49 7.5 % In, 472.5°C, 120 hr, 260X.

Fig. 50 7.5%, 249°C. 391 hr. 70,000X.

Fig. 51 7.5%, 249°C, 391 hr. 50,000X.

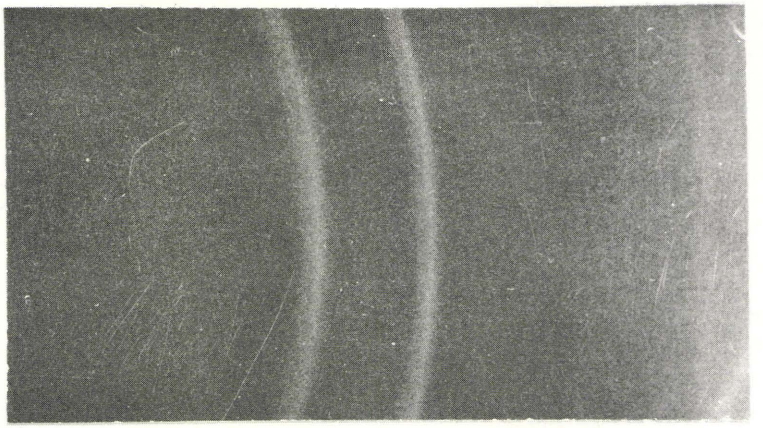

Fig. 52 Debye Scherrer X-ray Photograph of 10.1 % In, 404°C, 4 hr. $K_{\alpha 1}$, $K_{\alpha 2}$ doublet is resolved for α phase.

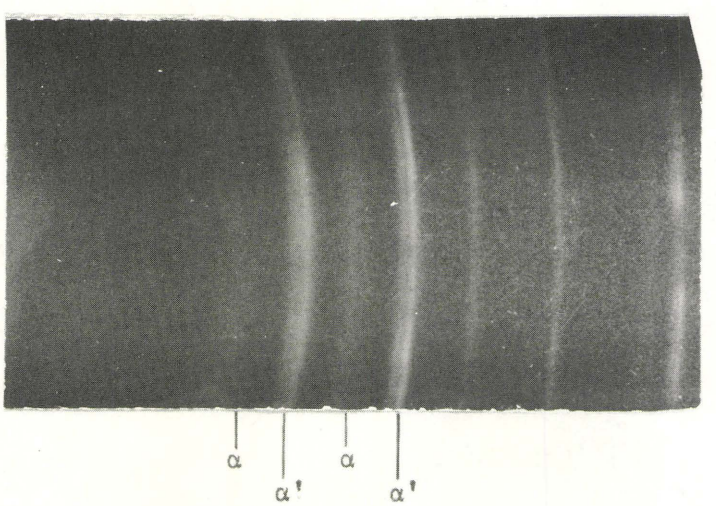

Fig. 53 Debye - Scherrer X-ray Photograph of 7.5 % In, 329°C, 11 hr.

$K_{\alpha 1, \alpha 2}$ doublet is resolved for α' phase.

$K_{\alpha 1, \alpha 2}$ doublet is not resolved for α phase.

Fig. 54 Examples of the Cell - Matrix Interface

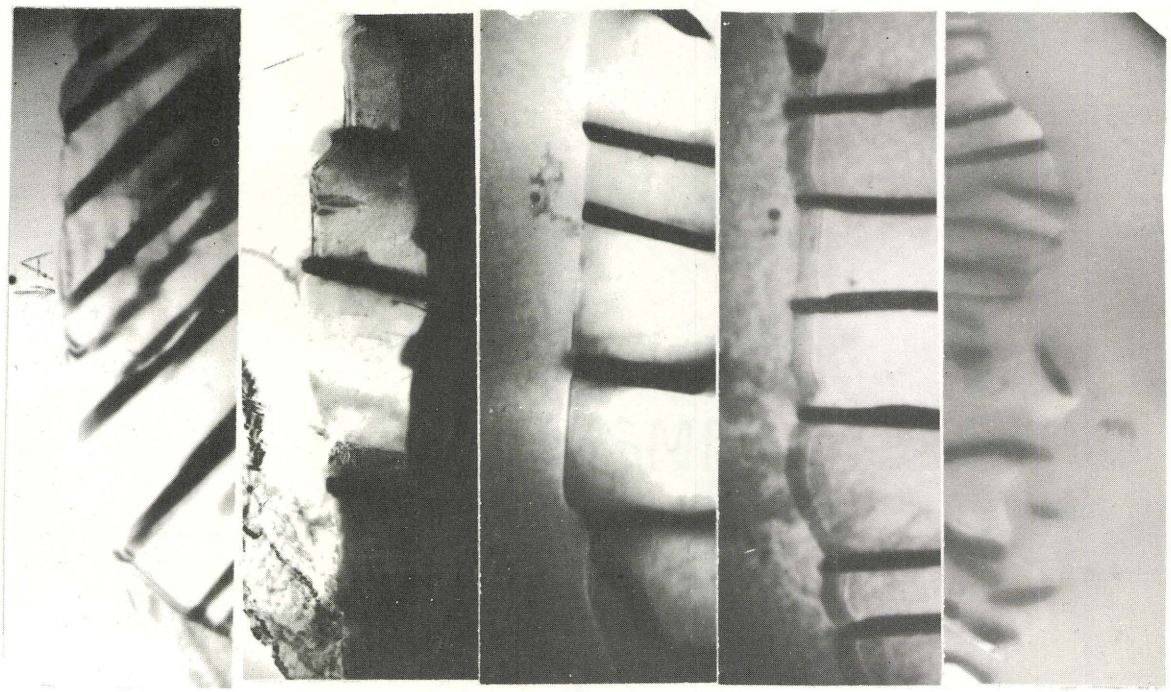

a b c d e

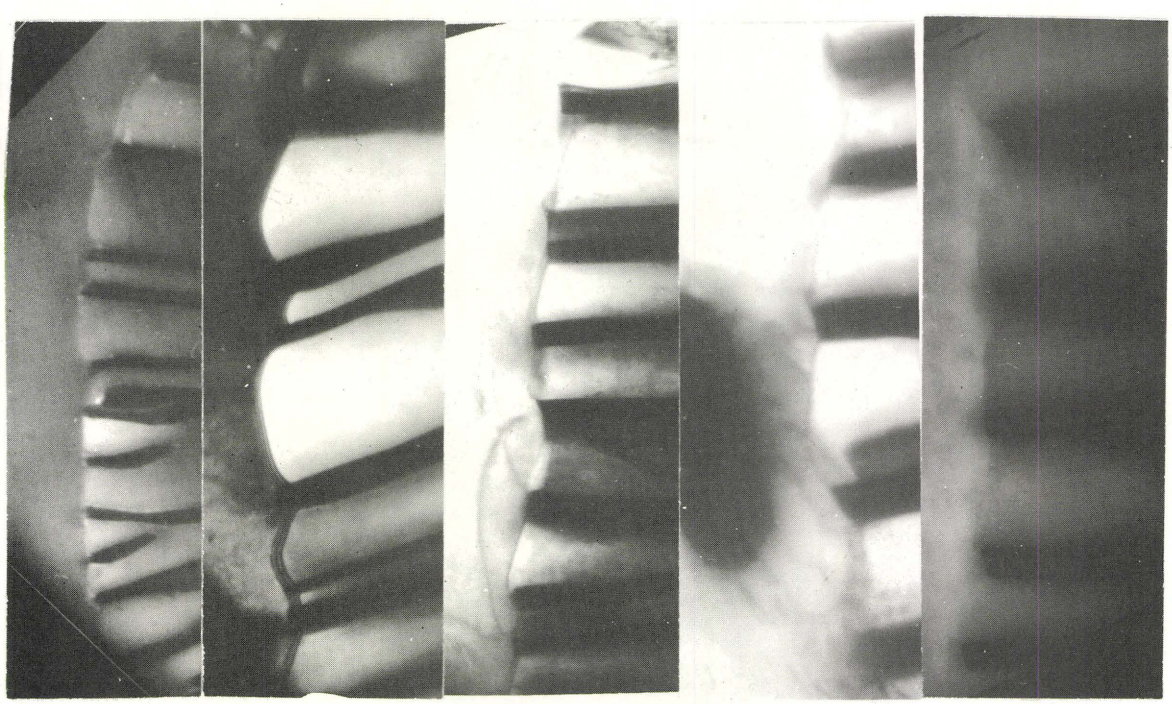

f g h i j

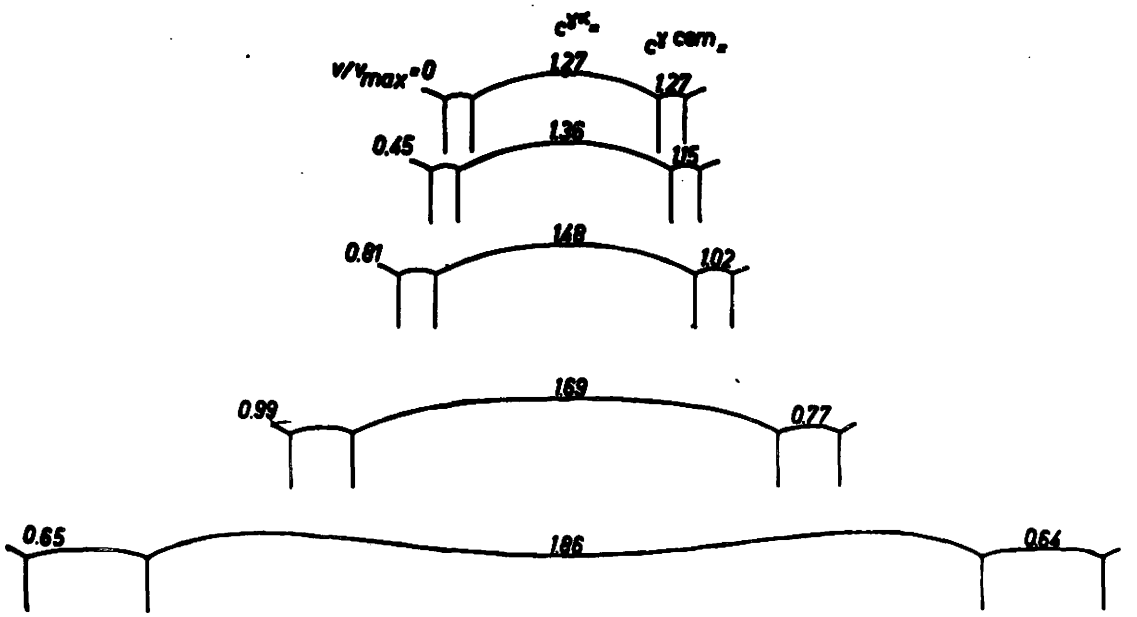

Calculated shape and growth rate of pearlite with different interlamellar spacings.

Fig. 55 From ref. 23.

FIG. 56 BOUNDARY DIFFUSION COEFFICIENT CALCULATED FROM TURNBULLS EQ.27

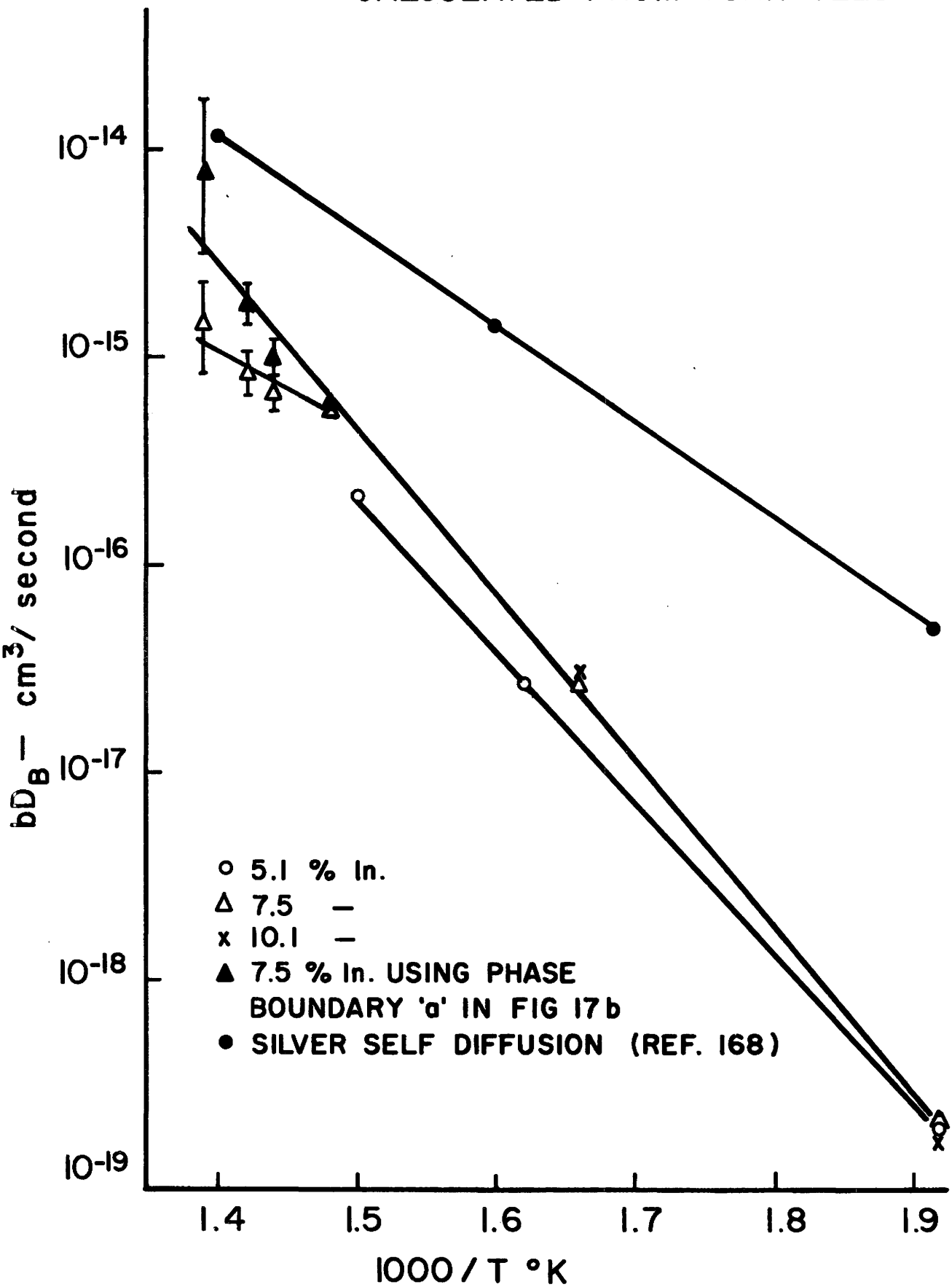

FIG. 57 PROPOSED VARIATION OF BOUNDARY DIFFUSION COEFFICIENT WITH TEMPERATURE AND COMPOSITION.

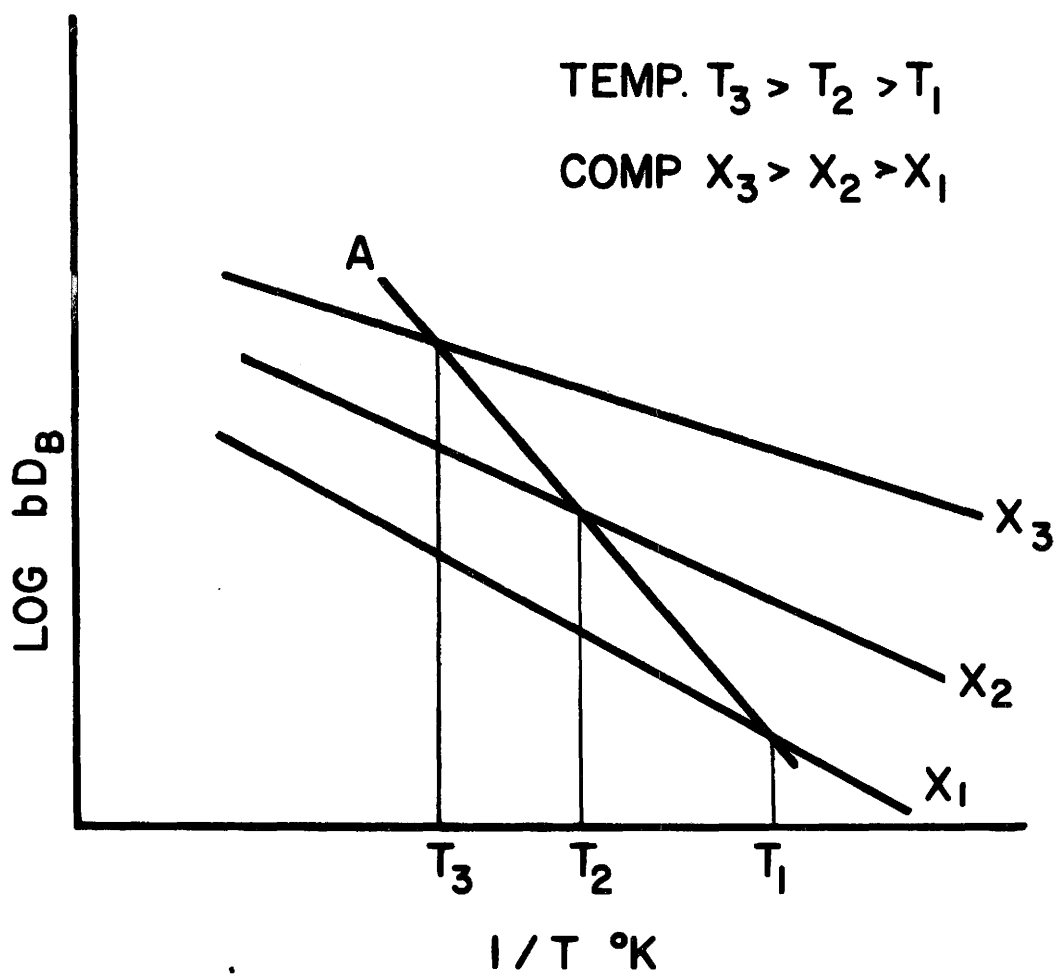

FIG. 58 THE INTERFACE MOBILITY FOR VARIOUS REACTIONS

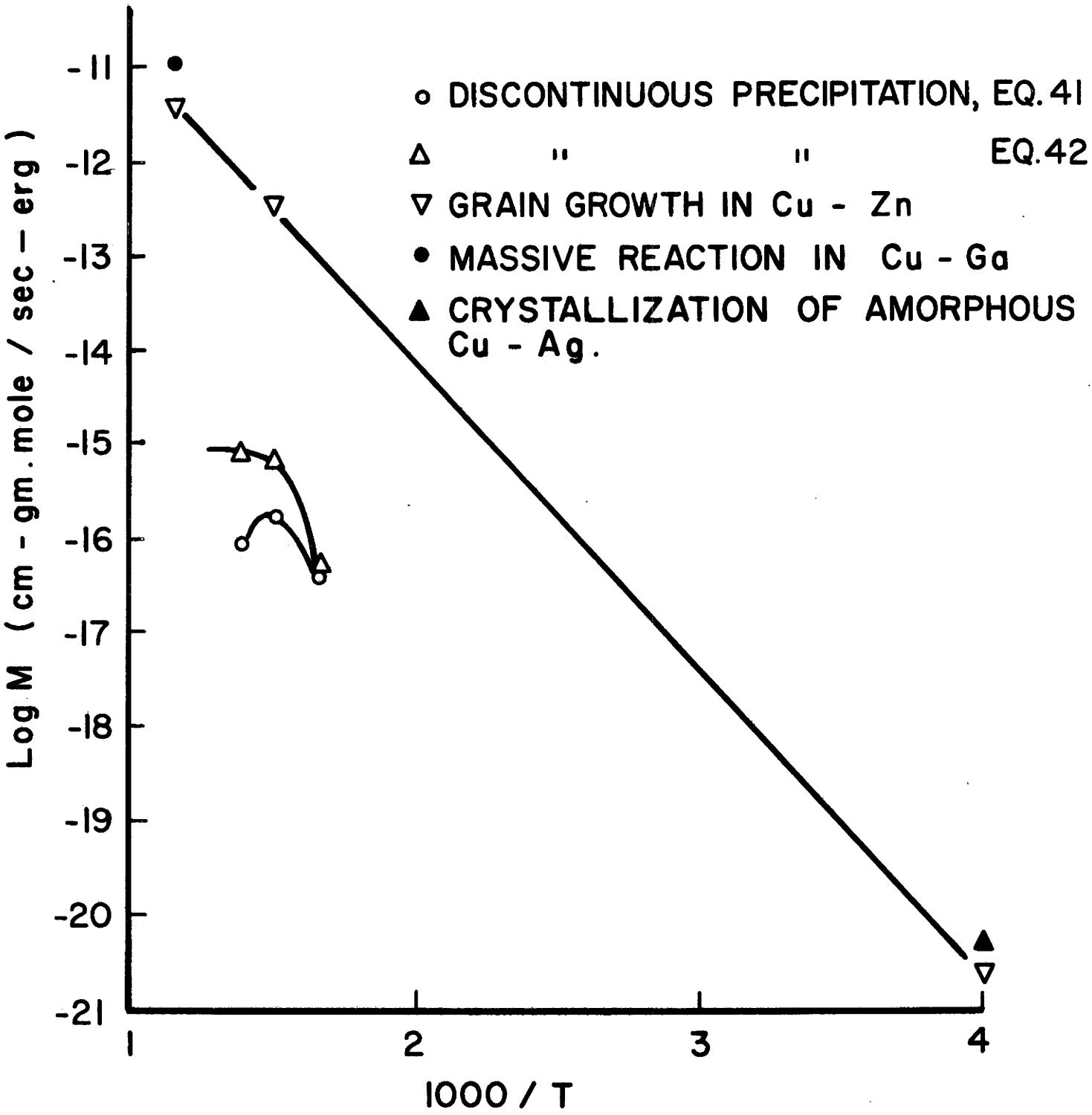

FIG. 59 vS^3 VERSUS RECIPROCAL TEMPERATURE

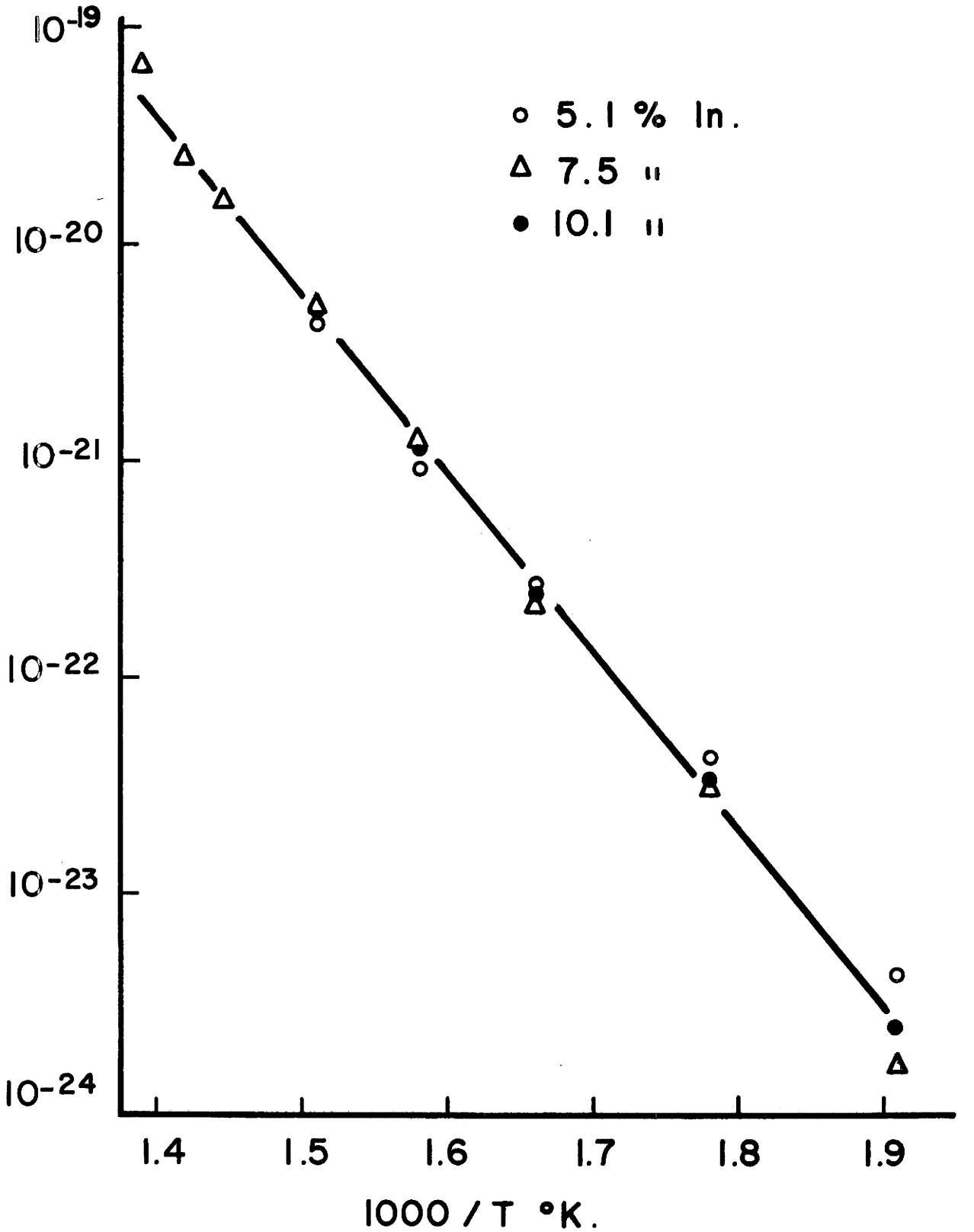

FIG. 60

RECIPROCAL SPACING VERSUS $-\Delta F_0$ AS CALCULATED FROM EQUATION 88.

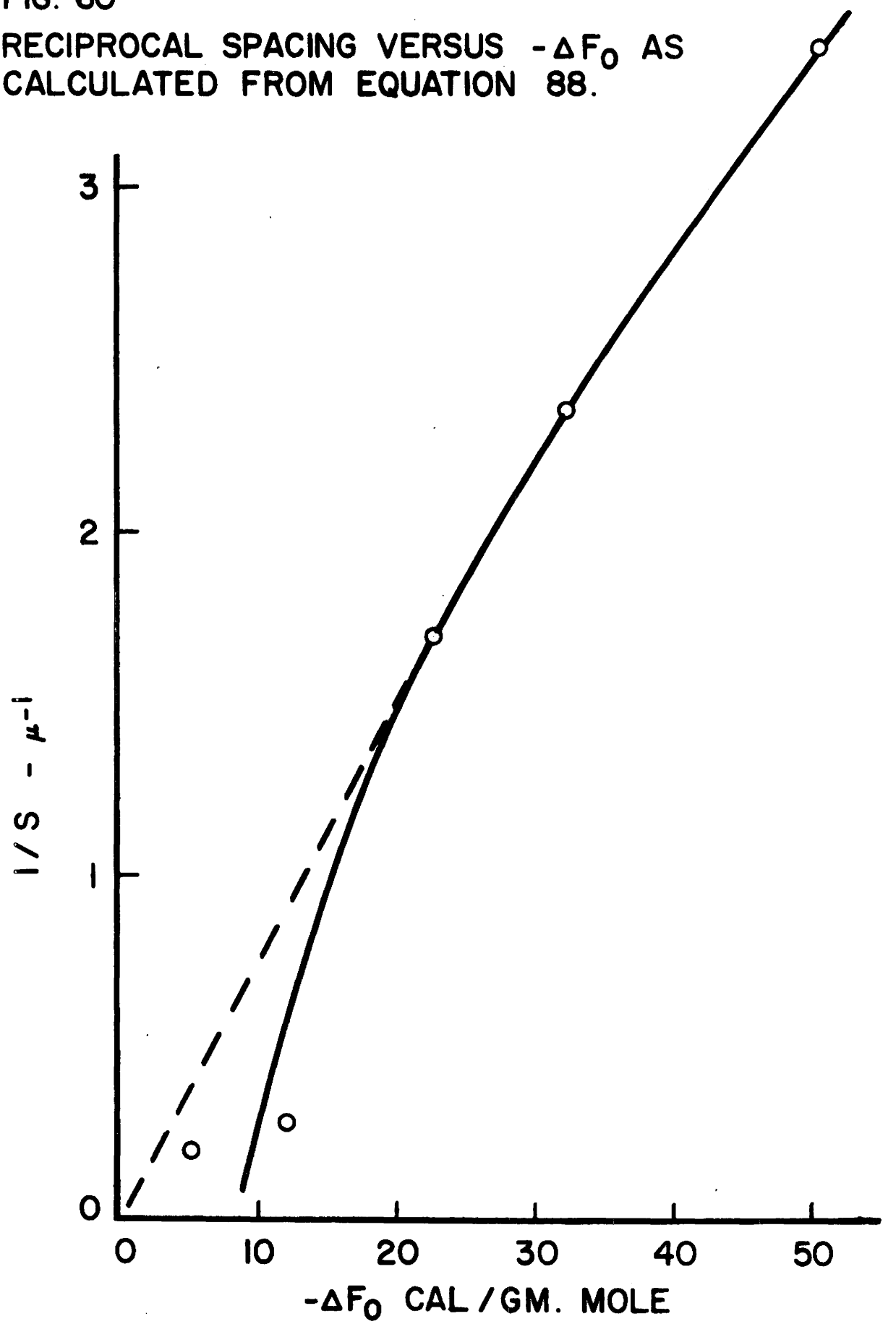

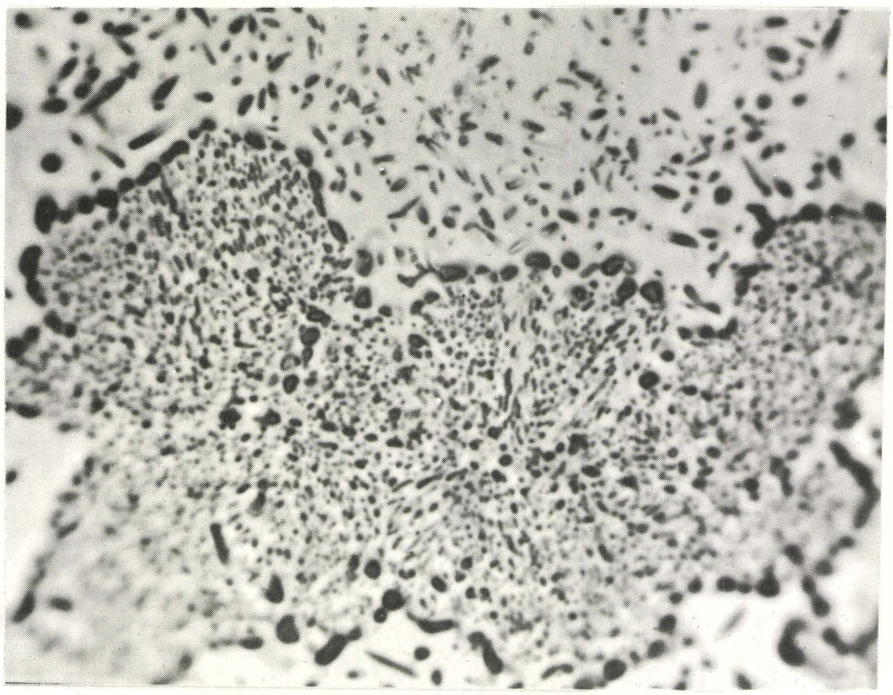

Fig. 61 7.5%In, held 10 hr. at 330°C, then 26 hr. at 450°C
1780x

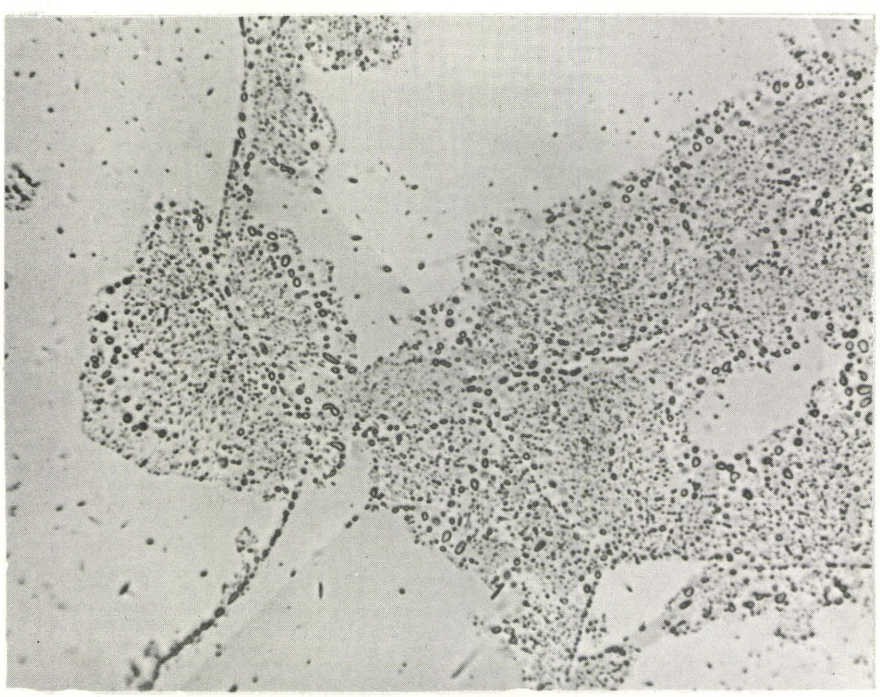

Fig. 62 7.5%In, held 10 hr. at 330°C, then 12 hr. at 461°C
760x

a

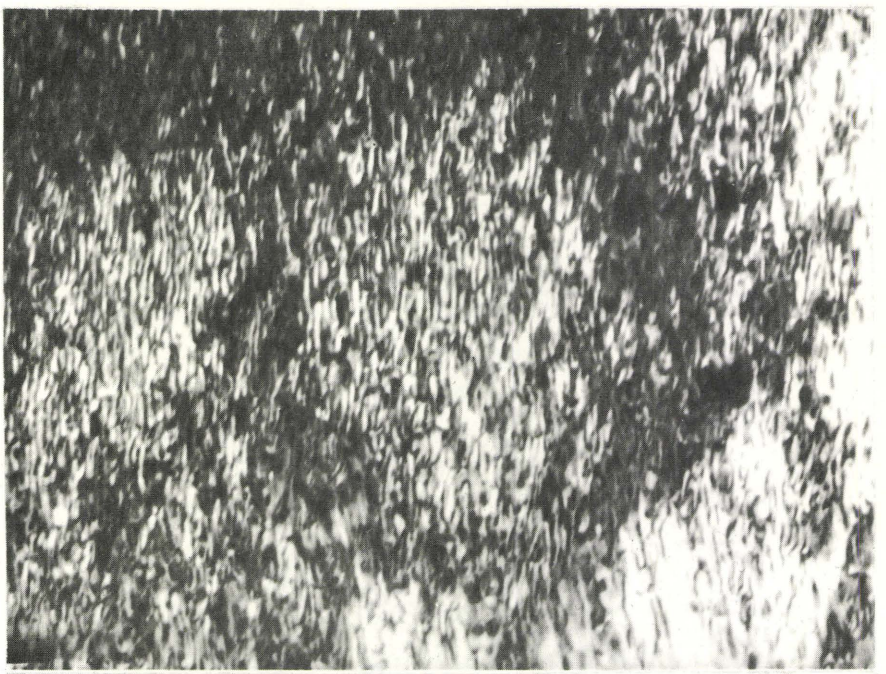

b

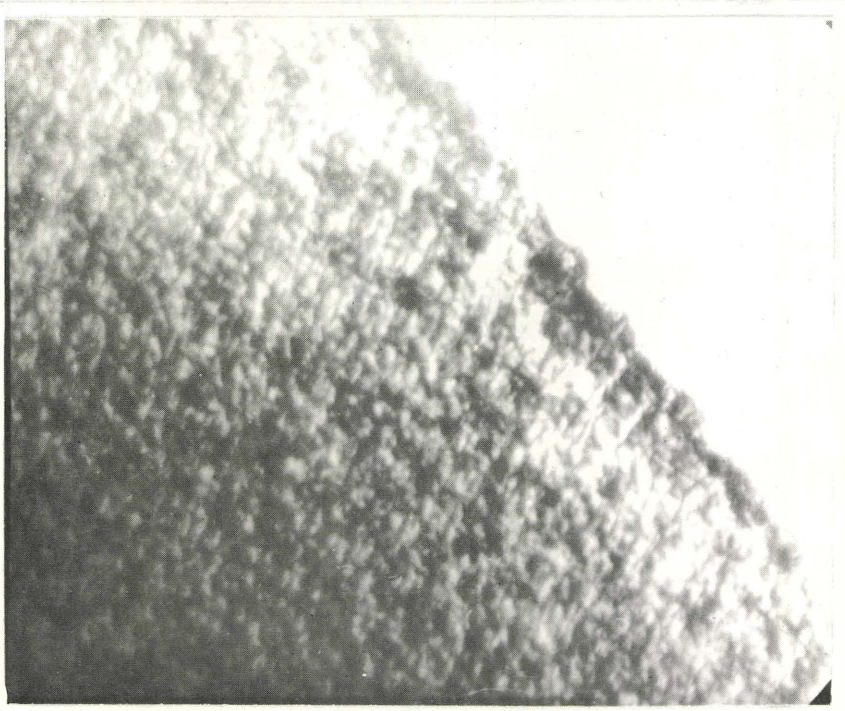

Fig. 63 Cu-7.5%In, thinned and electroplated with Ni for 1 min. at 1.5 ma/cm

a. Moire pattern. 10,000x

b. Dislocation Network. 73,000x